Journal of
Materials Chemistry A

ROYAL SOCIETY
OF CHEMISTRY

REVIEW

View Article Online
View Journal | View Issue

Check for updates

Cite this: J. Mater. Chem. A, 2025, 13, 2441

Progress in crystalline silicon heterojunction solar cells

Bingquan Liang,[abc] Xinliang Chen, *[abc] Xiaofeng Wang,[abc] Heze Yuan,[abc] Aixin Sun,[abc] Zheng Wang,[abc] Liyuan Hu,[abc] Guofu Hou,[abc] Ying Zhao[abc] and Xiaodan Zhang[abc]

Received 2nd September 2024
Accepted 10th December 2024

DOI: 10.1039/d4ta06224h

rsc.li/materials-a

At present, the global photovoltaic (PV) market is dominated by crystalline silicon (c-Si) solar cell technology, and silicon heterojunction solar (SHJ) cells have been developed rapidly after the concept was proposed, which is one of the most promising technologies for the next generation of passivating contact solar cells, using a c-Si substrate and two hydrogenated amorphous silicon (a-Si:H) thin films. SHJ solar cells not only have the advantages of high conversion efficiency and high open-circuit voltage, but also have a low temperature coefficient and free from potential induced degradation. For SHJ solar cells, the passivation contact effect of the c-Si interface is the core of the entire cell manufacturing process. To approach the single-junction Shockley–Queisser limit, it is necessary to passivate monocrystalline silicon well to reduce the efficiency loss caused by recombination. Recently, the successful development of silicon heterojunction technology has significantly increased the power conversion efficiency (PCE) of crystalline silicon solar cells to 27.30%. This review firstly summarizes the development history and current situation of high efficiency c-Si heterojunction solar cells, and the main physical mechanisms affecting the performance of SHJ are analyzed. Subsequently, an overview is provided on the selection and application of passivation contact layer materials, with particular emphasis on distinguishing between various types of passivation materials and their respective roles in facilitating selective carrier transportation. Then, other components of SHJ solar cells are reviewed, including the selection and application of transparent conductive electrode materials that can reduce or replace indium element use. The application of copper plating technology and laser transfer printing (LTP) technology in the industrial development of SHJ solar cell technology is discussed. Finally, the development status of SHJ-based tandem solar cells is discussed, and also the prospects, challenges, as well as potential solutions for industrial development of SHJ solar cells are outlooked.

1. Introduction

Solar energy is a renewable energy source and the most representative green energy source, because of its non-toxic, harmless, non-polluting, inexhaustible characteristics.[1] Silicon is an indirect bandgap semiconductor with a band gap of 1.12 eV, corresponding to a cut-off wavelength of light absorption wavelength of about 1160 nm, and its bandgap closely matches the solar spectrum and photogenerated electrons/holes can exhibit a long lifetime.[2] At present, crystalline silicon (c-Si) cells occupy 95% of the global market share and are currently the most important photovoltaic technology.[3,4] With a newly installed capacity of over 100 MW per day on average, photovoltaic (PV) solar cells have become the fastest growing class of solar energy–harvesting technologies.[5] The large-scale deployment of PV has been mainly based on diffused junction silicon solar cells. The increased quality of c-Si wafers at acceptable cost, dielectric surface passivation schemes, and the possibility of making direct metal–silicon contacts on relatively lightly doped surfaces have been important factors.[6,7] The device physics underlying such solar cells is well understood, and the theory coupled with device and material characterization has been an important contributing factor to the increasing sophistication of solar energy technologies. SHJ solar cells have attracted a lot of attention in the past few years due to its high performance, reasonable production cost.[8] In SHJ solar cells, an intrinsic hydrogenated amorphous silicon (a-Si:H) layer provides passivation of the Si wafer, a doped hydrogenated amorphous silicon (a-Si:H) layer provides good vertical conductivity and a suitable work function for carrier selection, and a well-designed transparent conductive oxide (TCO) reduces sensitivity to the work function of the metallic

---

[a] Institute of Photoelectronic Thin Film Devices and Technology, Nankai University, Tianjin 300350, China. E-mail: cxlruzhou@163.com

[b] Tianjin Key Laboratory of Efficient Utilization of Solar Energy, Nankai University, Tianjin 300350, China

[c] State Key Laboratory of Photovoltaic Materials and Cells, Nankai University, Tianjin 300350, China

terminals, in addition to providing lateral current transport and light coupling. According to theoretical calculations, the limiting efficiency of SHJ solar cells reaches 29.4%.[9] Analyses on series resistivity (R_s) explicit that the upper bound for the sum of contact resistivities for p-type ($\rho_{c,p}$) and n-type ($\rho_{c,n}$) contacts is 0.073 Ω cm^2.[10] With the continuous improvement of contact resistivity, it comes to the conclusion that the theoretical limiting efficiency estimated by Brendel's formulation is 28.5% for SHJ solar cells which is shown in Table 1.[11] The limiting efficiency of PERC inhibits further development, but SHJ and Tunnel Oxide Passivated Contact (TOPCon) solar cells are the next direction of industrial renewal and research. In the case that the limit efficiency difference between TOPCon and SHJ solar cells is minor, low temperature production and simple production line process have become the main advantages for SHJ.[13]

Due to the advancements in silicon ingot growth processes, defect engineering, and contamination control during solar cell manufacturing, the bulk electronic quality of c-Si wafers has been enhanced to a degree where further device improvements now depend on innovative interface passivation and carrier-selective contact structures. A high-quality passivation layer is a key requirement to optimize the performance of SHJ solar cells.[14] The improvement of SHJ solar cells efficiency now mainly relies on innovative interface passivation and carrier selective contact structures, which become the focus of current research. Currently, high-quality a-Si:H deposited by radio-frequency plasma enhanced chemical vapor deposition (RF-PECVD) is widely used for passivation of c-Si surfaces, which can reduce the recombination loss of the silicon surface and obtain higher open-circuit voltage (V_{OC}).[15] This review focuses on the conditions for depositing a-Si and corresponding improvements to the carrier selection layer, such as nano-crystalline silicon (nc-Si), or nc-Si alloy with oxygen (O) and carbon (C). Novel transparent electrodes for SHJ have been explored to further reduce improve optical and electrical properties (high transmittance and low resistance) as well as production costs (less or no use of In). Finally, the tandem solar cell with SHJ solar cells is introduced, which would exhibit more than 35% of high-efficiency solar cells. Further research is focus on the various compositions of SHJ solar cells, thus ensuring that the efficiency of SHJ solar cells continues to improve.

2. Theories and measurements of SHJ solar cells

High-efficiency silicon-based solar cells are mainly improved through heterojunction structure with a-Si:H thin films as the passivation layer. Fig. 1a shows the schematic diagram of a traditional bifacial SHJ solar cell structure and Fig. 1b is the corresponding schematic band structure diagram. Fig. 1c gives the schematic diagram of an SHJ-IBC solar cell structure, and Fig. 1d presents the typical TOPCon solar cell structure with ultrathin SiO_x as a passivation layer. TOPCon and SHJ solar cells are two important directions for industrialization. At present, among silicon solar cells technologies, aluminum back surface field (Al-BSF) solar cells and passivated emitter and rear cells (PERC) dominate the production of large-scale industrial PV devices.[16] In Al-BSF and PERC solar cells, photogenerated minority carriers are collected by emitters formed by a dopant diffusion process. The main difference between the two structures is on the rear side, where the full area aluminized back contact is replaced by a dielectric passivation layer (such as an

Table 1 According to the ultimate efficiency obtained by the updated J_0 and ρ_c, showing combined selectivity ($S_{10,e\&h,max}$, top left), contact area fractions that maximize the efficiency ($f_{e,max}$, top right; $f_{h,max}$, bottom left), and theoretical limiting efficiency (η_{max}, bottom right) calculated with updated contact resistivities for a-Si:H(i)/a-Si:H(p) and a-Si:H(i)/a-Si:H(n) selective contacts (reproduced from ref. 11 and 12 with permission from Elsevier, copyright 2018 & 2021)[a]

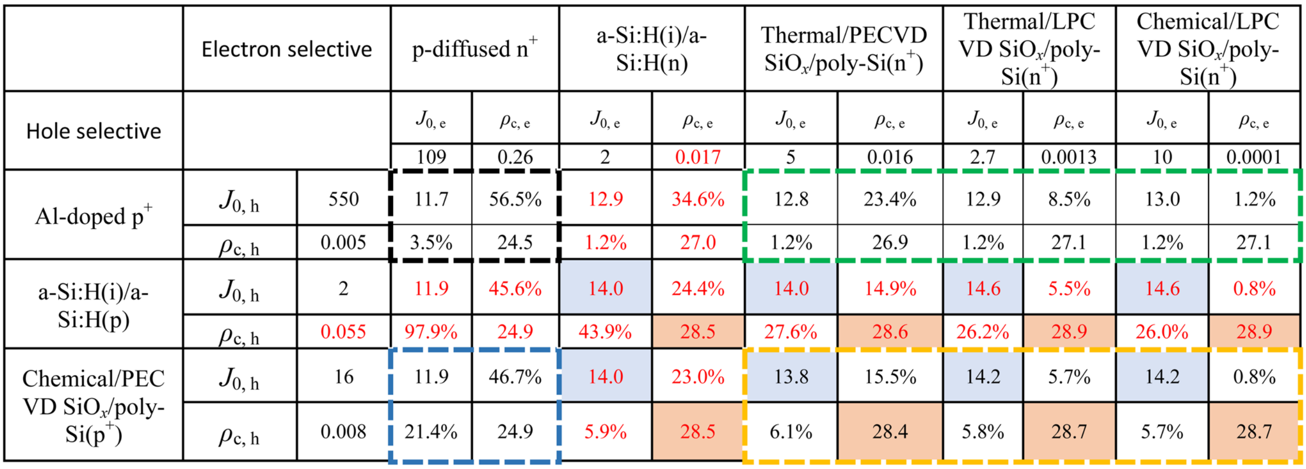

	Electron selective		p-diffused n$^+$		a-Si:H(i)/a-Si:H(n)		Thermal/PECVD SiO_x/poly-Si(n$^+$)		Thermal/LPCVD SiO_x/poly-Si(n$^+$)		Chemical/LPCVD SiO_x/poly-Si(n$^+$)	
Hole selective			$J_{0,e}$	$\rho_{c,e}$	$J_{0,e}$	$\rho_{c,e}$	$J_{0,e}$	$\rho_{c,e}$	$J_{0,e}$	$\rho_{c,e}$	$J_{0,e}$	$\rho_{c,e}$
			109	0.26	2	0.017	5	0.016	2.7	0.0013	10	0.0001
Al-doped p$^+$	$J_{0,h}$	550	11.7	56.5%	12.9	34.6%	12.8	23.4%	12.9	8.5%	13.0	1.2%
	$\rho_{c,h}$	0.005	3.5%	24.5	1.2%	27.0	1.2%	26.9	1.2%	27.1	1.2%	27.1
a-Si:H(i)/a-Si:H(p)	$J_{0,h}$	2	11.9	45.6%	14.0	24.4%	14.0	14.9%	14.6	5.5%	14.6	0.8%
	$\rho_{c,h}$	0.055	97.9%	24.9	43.9%	28.5	27.6%	28.6	26.2%	28.9	26.0%	28.9
Chemical/PECVD SiO_x/poly-Si(p$^+$)	$J_{0,h}$	16	11.9	46.7%	14.0	23.0%	13.8	15.5%	14.2	5.7%	14.2	0.8%
	$\rho_{c,h}$	0.008	21.4%	24.9	5.9%	28.5	6.1%	28.4	5.8%	28.7	5.7%	28.7

[a] Box with blue background: combined selectivity greater than 14. Box with pink background: combined selectivity greater than 28%. Red dotted line: SHJ solar cell. Black dotted line: PERC solar cell. Blue dotted line: p-type TOPcon solar cell. Green dotted line: n-type TOPcon solar cell. Orange dotted line: Bi-facial TOPcon solar cell.

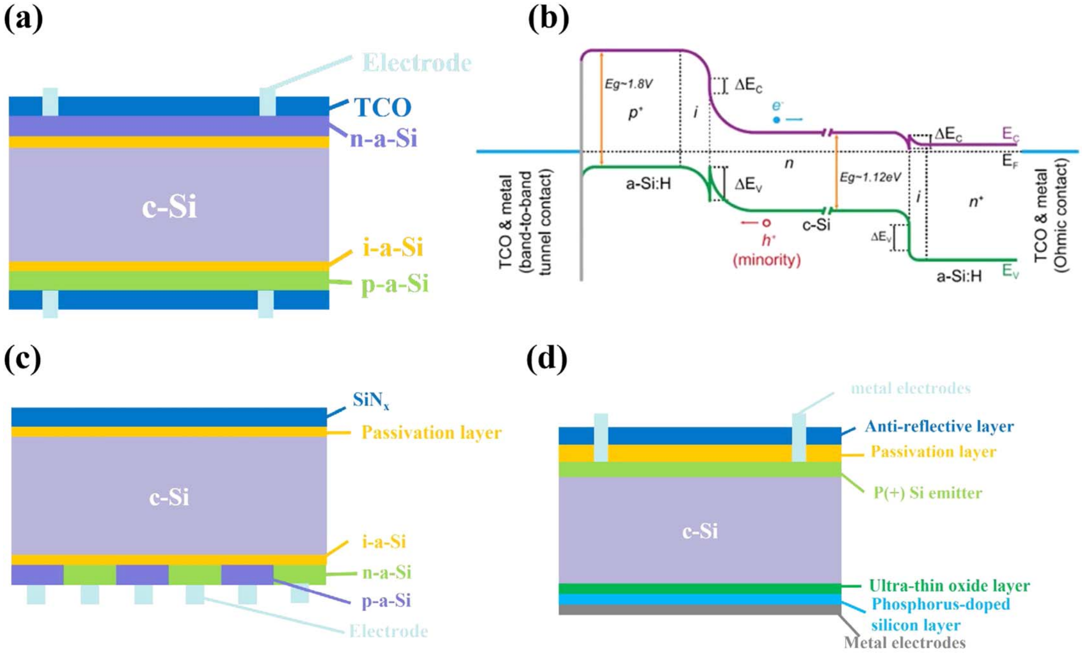

Fig. 1 (a) The structure of SHJ solar cell; (b) energy band diagram of SHJ solar cell; (c) the structure of IBC-SHJ solar cell and (d) the structure of TOPCon solar cell.

alumina layer) and a local aluminized contact. This evolution reduces the recombination current density on the rear side. However, due to the use of silicon–metal contacts on the front and back, severe recombination current densities can result in V_{OC} loss.[17,18]

Passivation contact technology can significantly reduce the contact recombination loss, and the two representative technologies are TOPcon and SHJ.[19] TOPcon solar cell follows the PERC technology, by using SiO_x/poly-Si passivation contact to replace the original metal contact (mainly the back) structure to provide an excellent surface passivation for the back of the silicon wafer, and thus improve the open circuit voltage as well as short circuit current.[20] The high performance of SHJ solar cells comes from surface passivation with thin intrinsic a-Si:H layers on the front and back, and the results show that with this structure, more than 750 mV of V_{OC} and more than 85% of FF can be obtained.[21] TOPCon is based on the PERC process (high temperature process), adding the preparation of tunnel oxide layer and polysilicon layer, and the production line is simple to upgrade. However, PERC and TOPCon exhibit scalability limitations because they rely on silver contact formation. This is especially evident in TOPCon solar cells, where the extensively used laser-enhanced contact optimization (LECO) process is applicable only to fired silver contacts.[22]

For solar cells, generally think of the ideal solar cell to calculate, that is, the series resistance is zero, and the parallel resistance is infinite. When the solar cell is in an open circuit state, $I = 0$, $R = \infty$. The expression for V_{OC} is as follows:

$$V_{OC} = \frac{nkT}{q}\left(\ln\frac{J_{SC}}{J_0} + 1\right) \approx \frac{nkT}{q}\ln\frac{J_{SC}}{J_0} \tag{1}$$

When the solar cell is exposed to light, the external circuit is short-circuited. At this time, the short-circuit current (J_{SC}) is equal to the I_{ph}, which is proportional to the incident light intensity, and the J_{SC} can be expressed as the following equation:

$$I_{SC} = I = I_{ph} \tag{2}$$

The fill factor (FF) is defined as the ratio of the maximum power output of the solar cell to the product of short-circuit current and open-circuit voltage:

$$FF = \frac{I_m V_m}{I_{SC} V_{OC}} \tag{3}$$

The percentage of the maximum power absorbed by the solar cells connection to the total radiant power incident on the cell is defined as the power conversion efficiency (PCE) of the solar cells η:

$$\eta = \frac{P_m}{A \times P_{in}} \times 100\% = \frac{FF \times V_{OC} \times J_{SC}}{P_{in}} \times 100\% \tag{4}$$

where P_{in} is the power of incident light per unit area and A is the area of the solar cell, according to the calculation for the ideal material, the band gap is about 1.5 eV.

The implied-V_{OC} (iV_{OC}) of solar cells can be obtained through minority carriers' lifetime.[23] There is no external current in the open-circuit solar cell, and the photogenerated current is balanced with the recombination current ($J_{ph} = J_{rec}$). In solar cells with thickness W, the photogenerated current density J_{ph} has the following relationship with the effective carrier lifetime τ_{eff}:

$$\mathrm{i}V_{\mathrm{OC}} = \frac{kT}{q}\ln\frac{\Delta n_0[\Delta p(0)]}{{n_\mathrm{i}}^2} \tag{5}$$

where N_A is the acceptor concentration, n_i is the intrinsic carrier concentration, Δn (0) and Δp (0) are the concentrations of carriers at the PN junction, and the iV_OC of the solar cell can be known by measuring the carrier lifetime. A higher iV_OC indicates superior device passivation. In fact, the dominant recombination mechanism in crystalline silicon cells is auger recombination, not radiation recombination. Based on the empirical parameterization of the experimentally measured radiation and auger recombination rate, the limit efficiency of c-Si solar cells can be obtained to be 29%,[24] and the theoretical limit efficiency of SHJ solar cells estimated according to Brendel's formula also reaches 28.5%.[11]

One of the major factors on the performance of SHJ are J_0 and ρ_c, in the design of solar cells to reduce the cell J_0 and ρ_c can significantly improve the performance of SHJ, lower J_0 and ρ_c are beneficial to improve the selective carrier transportation. Eqn (1) shows that V_OC is controlled by J_0, and thus lower J_0 leads to higher V_OC. J_0 is related to the intrinsic carrier concentration in the material, and changes dramatically with the change of temperature, J_0 has a great influence on V_OC, obviously.[25]

Reverse saturation current (J_0) consists of two main components, namely reverse saturation diffusion current J_{01} and reverse saturation compound current J_{02}. Recombination currents include in bulk recombination currents, surface recombination currents ($J_{0\mathrm{S}}$) and space charge region recombination currents ($J_{0\mathrm{scr}}$). For semiconductor materials, intrinsic recombination (radiation recombination and auger recombination) is a property of the material itself, which can only be eliminated by improving the quality of the material. The internal trap recombination can be reduced by improving the quality of the material. The magnitude of the recombination current in the bulk is mainly determined by the lifetime of the minority carriers, which satisfies the following relation:

$$\frac{1}{\tau_{\mathrm{bulk}}} = \frac{1}{\tau_{\mathrm{rad}}} + \frac{1}{\tau_{\mathrm{Aug}}} + \frac{1}{\tau_{\mathrm{trap}}} \tag{6}$$

where τ_rad is the recombination lifetime of radiation, τ_Aug is auger recombination lifetime and the τ_trap is the recombination lifetime of the trap.

For the surface recombination current, it can be expressed by the following formula:[24]

$$J_{\mathrm{OS}} = \frac{W}{2\tau_{\mathrm{eff}}}\frac{q{n_{\mathrm{i,eff}}}^2}{(N_{\mathrm{dop}} + \Delta n)} \tag{7}$$

where W is the layer thickness, S is the surface recombination rate, and $n_\mathrm{i,eff}$ is the effective intrinsic carrier concentration, which is related to excess carrier Δn, D is the ambipolar diffusion coefficient. $J_{0\mathrm{scr}}$ also has a certain degree of influence on the recombination current, and the relationship is shown as follows:

$$J_{0\mathrm{scr}} = \frac{qn_\mathrm{i}\omega}{\sqrt{\tau_\mathrm{n}\tau_\mathrm{p}}} \tag{8}$$

where, n_i is the intrinsic carrier concentration and ω is the space charge region depletion width. The reverse diffusion current originates from the p–n junction as well as the part of the metal–semiconductor contact. For p–n junction:

$$J_\mathrm{S} = q\left[\frac{D_\mathrm{p}P_{\mathrm{n}0}}{L_\mathrm{p}} + \frac{eD_\mathrm{n}n_{\mathrm{p}0}}{L_\mathrm{n}}\right] \tag{9}$$

where $n_{\mathrm{p}0}$ is the concentration of p-type junction minority (electron), $p_{\mathrm{n}0}$ is the concentration of n-type junction minority (hole). D_n and D_p are the electron and hole diffusion coefficients, respectively. $L_\mathrm{n} = \sqrt{\tau_\mathrm{n}D_\mathrm{n}}$ and $L_\mathrm{p} = \sqrt{\tau_\mathrm{p}D_\mathrm{p}}$ are the electron and hole diffusion lengths, respectively. For metal–semiconductor contact:

$$J_{\mathrm{ST}} = A^*T^2\ \exp\left(-\frac{e\phi_{\mathrm{Bn}}}{KT}\right) \tag{10}$$

where $A^* = \left(\frac{4\pi q m_\mathrm{n}^* k^2}{h^3}\right)$. Φ_n is the actual barrier height formed by metal–semiconductor contact. Charge carriers should be transferred and extracted as much as possible to reduce the current loss caused by recombination, which can improve the photocurrent and reduce the dark saturation current, thereby improving the V_OC of the solar cells.

Both J_0 and ρ_c have great impact on carrier selectivity. ρ_c is determined by the following relation:

$$\rho_\mathrm{c} = \left(\frac{1}{N_\mathrm{e}q\mu}\right) \tag{11}$$

The selectivity of minority carriers is determined by the formula:[25]

$$S_{10} = \log\ S = \log\left(\frac{V_{\mathrm{th}}}{J_0\rho_\mathrm{c}}\right) \tag{12}$$

where V_th is the thermal voltage. S_{10} can be used to determine the efficiency potential of the contact structure. For SHJ, if the carrier selectivity is insufficient, the external voltage V_OC at the electrode is lower than that of iV_OC. High-quality selective contacts should allow most carriers to be efficiently transported to the electrode and reduce recombination of minor carriers, resulting in improved J_SC and J_0, which ultimately improved the performance solar cell. The contact resistance ρ_c is used to quantify carrier transportation, and the recombination parameter J_SC is used to describe carrier recombination.[25] To improve the conversion efficiency of solar cells, small J_0 and ρ_c have a great promotion effect on the selective transmission of charge carriers, and can also improve the PCE of SHJ.

For practical purposes, it is worth noting that among all available techniques for measuring ρ_c, the most straightforward are the transfer length method (TLM) and circular transmission line method (CSM). Similarly, research groups reported that in SHJ solar cells, high efficiency depends not only on outstanding passivation but also on low ρ_c. Fig. 2a displays the typical TLM structure used for characterizing c-Si solar cells, in the conventional TLM model, guaranteeing the ohmic contact between the electrode and the Si substrate is necessary to extract ρ_c. The total resistance (R_T) can be expressed as the following:[26]

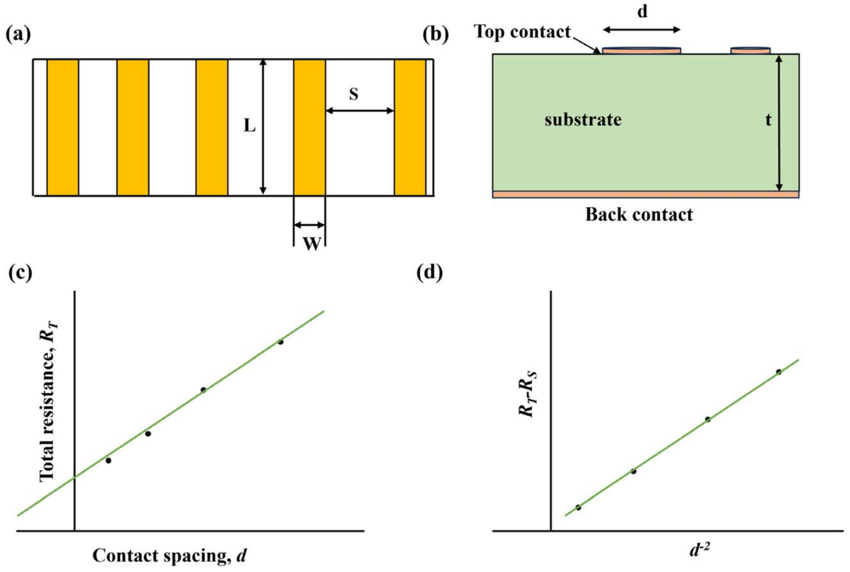

Fig. 2 (a) Typical TLM structure used for characterizing c-Si solar cells. The total resistance R_T is obtained by calculating the J–V data between the electrodes at different distances d, by application of a dc voltage V and measurement of the current (c) fitted curve of total resistance *versus* contact spacing (reproduced from ref. 26 with permission from Elsevier, copyright 2017). (b) Configuration of the conventional Cox–Strack measurement. The total resistance R_T is measured from a top contact of diameter d through a semiconducting substrate of thickness t to a back contact by applying a DC voltage V and taking the measurement of the current. (d) Plots of R_T–R_S *versus* d^{-2} and the corresponding linear fitting curve, and the slope of the curve is the specific contact resistance ρ_c (reproduced from ref. 27 with permission from Elsevier, copyright 2022).

$$W_T = \sqrt{\rho_c/R_{sh}} \tag{13}$$

$$R_T = \frac{R_{sh}W}{L} + 2R_C \tag{14}$$

$$R_C = \frac{R_{sh}W_T}{L}\coth\left(\frac{W}{W_T}\right) \tag{15}$$

where W_T is the transfer length, it indicates the average distance along W over which the current is transferred from the semiconductor to the metal, R_T is the total resistance, R_{sh} is the sheet resistance, ρ_c is the specific contact resistance. From eqn (14), the value of the total resistance at the y-intercept of the plot is $2R_C$, as shown in Fig. 2c. R_C can be deduced according to the potential distribution underneath the contact and is represented by eqn (15). When $W \geq 1.5W_T$, which can be the case for c-Si solar cells with excellent contact resistivity, eqn (15) can be approximated as: $R_C = \frac{\rho_c}{LW}$, hence $\rho_c = R_CWL$; in contrast, when $W \leq 0.5W_T$, in this case, R_C can be approximated as: $R_C = \frac{\rho_c}{WL}$, hence $\rho_c = R_CLW_T$.

The CSM model was first proposed by Cox and Strack in 1967, Fig. 2b and c show the general structure of CSM measurement and the plot of R_T–R_S *versus* d^{-2}, respectively. Theoretically, the total resistance (R_T) in a circuit can be expressed as:[27]

$$R_T = R_C + R_S + R_0 \tag{16}$$

$$R_S = \frac{\rho}{d\pi}\arctan\frac{4t}{d} \tag{17}$$

$$R_C = \frac{\rho_c}{\pi d^2/4} \tag{18}$$

where ρ and t are the resistivity and thickness of Si substrate, respectively, d is the diameter of disk electrode and ρ_c is the specific contact resistance. R_T consists of three components: contact resistance R_C, extended resistance R_S, and residual resistance R_0. Both the TLM and CSM measurements are suitable for measuring devices with good ohmic contacts between the electrodes and the Si substrate. Shanmugam Kailasam *et al.*[28] found that the CSM method can be used to obtain ρ_c more accurately when a device with non-ohmic contact (asymmetric structure) meets the following conditions:

The direction of the charge carriers and charge current density in the test structure should match the direction of the photocarriers in the solar cell. The main reason is that the direction of the charge carriers in the test structure doesn't match the direction of the photo-induced carriers in the solar cell, using the TLM method to test contact resistance is likely to introduce a large error in the data.

3. Historical development of SHJ solar cells

In the late 60s of the 20th century, the discovery of hydrogenated amorphous silicon (a-Si:H) led to the development of electronic properties of a-Si:H with reasonable carrier mobility.[29] The first solar cell using the SHJ structure consisted of the bottom cell of the a-Si:H/polysilicon heterojunction in a tandem solar cell, which was patented in 1985.[30] In 1991, Sanyo Corporation obtained a hybrid design patent for SHJ solar cells under the trademark HIT (Heterogeneous Intrinsic Thin Layer), which increased the efficiency of HIT cells by 18.1%. With the further upgrading of the process, the efficiency of SHJ was over 20% in 2000,[31] as shown in Fig. 3a. And then by reducing the carrier concentration of transparent conductive oxide (TCO) films to reduce free carrier absorption (FCA) and increasing Hall mobility to optimize transverse conductivity, Sanyo improved the efficiency of SHJ to 24.7% in 2014.[39] In 2014, Panasonic combined HIT technology with the IBC concept to achieve an efficiency of 25.6%.[40] In 2017, Kaneka Corporation achieved a record efficiency of 26.63% with their single-junction SHJ-IBC devices, and this technology combines the interdigital back contact (IBC) structure with SHJ solar cells to significantly reduce parasitic absorption from a-Si:H and TCO layers, resulting in improved power conversion efficiency,[32] as shown in Fig. 3b. Concurrently with the advancement of n-type silicon, there has been a parallel improvement in the comprehension of LID in p-type silicon. It was not until the mid-to-late 90s of the 20th century that degradation mechanisms involving boron pairs (introduced as dopant atoms) and oxygen pairs (introduced in large concentrations by the Cz process during crystal growth) were discovered.[41] In 2015, the efficiency of double-sided batteries has also been greatly improved, and a large-size (151.9 cm^2) solar cell with a conversion efficiency of 25.1% has been achieved, see in Fig. 3c.[33] In February 2018, ISFH prepared an IBC structure solar cell based on p-type silicon, which achieved an efficiency of 26.1%,[34] and the current champion efficiency of SHJ solar cells of p-type silicon is 26.56% created by LONGi in October 2022.[42]

Subsequently, LONGi successfully introduced the nano-crystallization process into the fabrication of the tip HSC with corresponding TCO. The front finger was fabricated by laser transfer process to reduce the shading ratio from 2.8 to 2.0%, the window layer of the front finger was optimized to reduce parasitic absorption, a MgF_2/Ag reflective layer was added on the back side, and the ITO was replaced by ICO. These improvements improved V_{OC} and J_{SC} of SHJ solar cells, and a certified PCE of 26.81% was achieved.[35] What's more, LONGi still holds the title for champion efficiency of mono-crystalline silicon heterojunction solar cells, and the solar cell with Heterojunction Back Contact (HBC) structure has a certified efficiency of 27.30%.[21] In recent year, Maxwell has made significant advances in copper plating, SHJ solar cells were fabricated using doped nc-SiO_x:H as a passivation contact layer, which exhibited excellent electron selectivity, low parasitic absorption, and high uniformity, additionally, seed-free copper plating with high aspect ratio and low metal fraction was employed.[36,43] Finally, a certified efficiency of 26.41% is obtained for M6-size bifacial silicon heterojunction devices, as shown in Fig. 3e. Regarding the development of flexible solar cells, Liu *et al.* [44] prepared

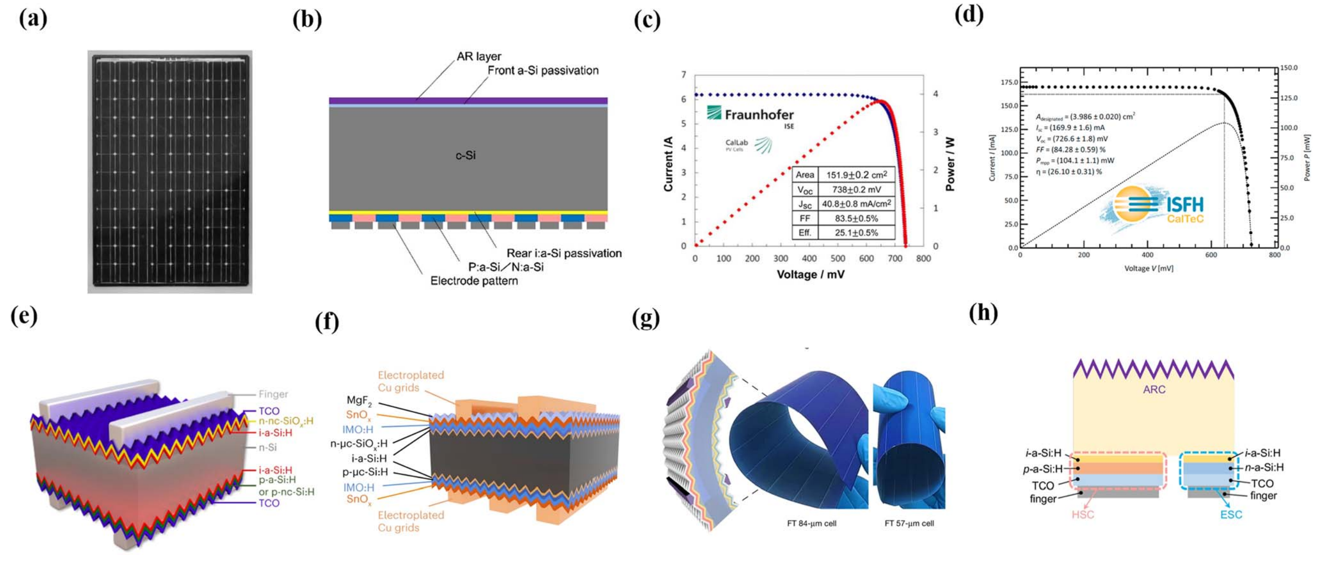

Fig. 3 (a) The world's first industrialization of a-Si/c-Si hybrid solar cell produced by Sanyo and an efficiency of 15.2% was gained (reproduced from ref. 31 with permission from Wiley, copyright 2000). (b) Cross-sectional schematic drawing of the HJ-IBC solar cell, which reached a record 26.7% in 2017 (reproduced from ref. 32 with permission from Elsevier, copyright 2017). (c) The first both-side-contacted c-Si solar cell to break through 25.1% efficiency in 2015 (reproduced from ref. 33 with permission from American Institute of Physics, copyright 2015). (d) Light J–V curve and power in dependence of the voltage of the POLO-IBC cell measured at the ISO 17025-accredited Calibration and Test Center, ISFH-CalTeC. The power conversion efficiency of the POLO-IBC cell is 26.10% (reproduced from ref. 34 with permission from Elsevier, copyright 2018). (e) Device structure of LONGi SHJ solar cell with p-type doped nanocrystalline silicon and a low sheet resistance transparent conductive oxide, which won the high PCE of 26.81% (reproduced from ref. 35 with permission from Springer Nature, copyright 2023). (f) Device structure of Maxwell prepared SHJ solar cells with plating copper electrode and double-sided indium-based transparent (dopant-free SnO_x: IMO : H = 1 : 1) electrodes, and a certified efficiency of 25.94% was achieved (reproduced from ref. 36 with permission from Springer Nature, copyright 2023). (g) Ultra-thin (57 μm) flexible SHJ solar cell prepared by LONGi, which exhibited the high power-to-weight ratio (1.9 W g^{-1}) and open-circuit voltage (761 mV) (reproduced from ref. 37 with permission from Springer Nature, copyright 2024). (h) Device structure of heterojunction back contact (HBC) solar cell with an efficiency of up to 27.09% (reproduced from ref. 38 with permission from Springer Nature, copyright 2024).

a flexible solar cell with high efficiency (>24%), a large area (>240 cm^2) with edge-blunting passivation technology, in August 2022. This technology enabled to improve the flexibility of silicon wafers by blunting the pyramidal structure in the marginal regions. In 2022, LONGi developed a large-area (274.4 cm^2) flexible SHJ solar cell with a minimum thickness of 57 μm, which has a very high power-to-weight ratio of 1.9 W g^{-1} and a high V_{OC} of 761 mV.[44] The development of flexible solar cell technology provides a practical basis for creating lightweight, low-cost, high-efficiency SHJ solar cell devices.

Historically, the main design concepts that have been proven to be critical to improve c-Si technologies, the concepts are as follows: (i) a rear surface field below the rear contact; (ii) effective surface texture for light capture; (iii) surface passivation of c-Si surfaces and (iv) contact structure (conventional structure and BC structure). Table 2 describes the corresponding devices in this article, including solar cells with small-and large-are bifacial contact amorphous silicon or polycrystalline silicon passivation layer from laboratories and enterprises.

4. Passivation contact materials and device applications in SHJ solar cells

For a solar cell to function, there must be a selective transport of charge carriers. The theoretical method to achieve carrier selectivity is to directly add conductive layers to c-Si silicon wafers with asymmetric work functions (ϕ) at the conduction and valence band edges. In this theoretical approach, Schottky–Mott theory is followed, the PCE of solar cells would increase stably with the charge-carriers transportation is fulfilled. In practice, the existence of surface phenomena such as dangling bonds, metal induced gap states (MIGS) and inter-face dipoles, makes it difficult for theoretical methods to be explained using Schottky–Mott theory, resulting in the Fermi level pinning (FLP) which forms a Schottky barrier on the interface.[14] To solve this problem passivation contact processes have been developed and SHJ was developed based on this technology. Under the condition of no passivation contact, the metal electrode in contact with Si directly, which makes the carrier recombination extremely, resulting in a high J_0, a high contact resistance and a low V_{OC} even leading to the FLP, thus making it difficult to achieve a great breakthrough in the efficiency of solar cells. Passivation contacts are defined as a set of layers that provide both selective conduction of charge carriers and effective passivation of the silicon surface.

Passivation quality directly determines the performance of SHJ. The quasi-steady-state photoconductance method (QSSPC) has been widely applied to evaluate the passivation performance of monocrystalline silicon.[49,50] Carrier lifetime τ_{eff}:

$$\frac{1}{\tau_{eff}} = \frac{1}{\tau_{bulk}} + \frac{2S}{W} \tag{19}$$

where W is the thickness of the wafer and S is the surface recombination velocity at the front or back side of the wafer, which is expected to vary with the carrier injection level. In addition, there is another method to evaluate the passivation performance, called microstructure factor R. Hydrogen plays an important role in alleviating the structural stress of silicon network and passivating the suspended bonds in the preparation of high-quality silicon thin film materials. By analyzing the bonding configuration of Si and H atoms in the infrared absorption spectrum of silicon thin films, useful information about the microstructure of the films can be obtained.[51] The microstructure factor R is defined as follows:

$$R = \frac{I_{HSM}}{I_{HSM} + I_{LSM}} \tag{20}$$

where I_{HSM} (I_{LSM}) is high (low) stretching mode, it is generally believed that the low-order expansion mode (LSM) of 2000 cm^{-1} in the infrared spectrum of amorphous silicon thin films corresponds to $Si{:}H_1$, reflecting the dense part of the film. The high-order expansion mode (HSM) of 2060–2160 cm^{-1} is related to the bonding hydrogen on the inner surface of the cavity in the thin film, including $Si–H_2$ (2090–2120 cm^{-1}) and $Si–H_3$ (2120–2150 cm^{-1}).[49,52]

Table 2 Performance summary of silicon heterojunction solar cells

No.	Wafer type	V_{OC} (mV)	J_{SC} (mA cm^{-2})	FF (%)	E_{ff} (%)	Year	Production agency
1	n-type	750	39.5	83.2	24.7	2014	Sanyo[39]
2	n-type	740	41.8	82.7	25.6	2014	Panasonic[40]
3	n-type	738	40.8	83.5	25.1	2015	Kaneka corporation[33]
4	n-type	729	40.7	76.4	22.6	2017	EPFL[45]
5	n-type	738	42.7	84.9	26.7	2017	Kaneka corporation[32]
6	n-type	736	41.5	81.9	25.0	2020	CSEM[46]
7	n-type	730	40.3	82.3	24.2	2020	CSEM[46]
8	p-type	723	40.7	80.8	23.8	2020	CSEM[46]
9	n-type	747	39.6	84.9	25.1	2020	Hanergy[47]
10	n-type	725	40.9	80.9	24.0	2021	Jülich[48]
11	n-type	751.4	41.45	86.1	26.81	2023	LONGi[35]
12	p-type	751.3	41.29	85.59	26.56	2024	LONGi[42]
13	n-type	750.2	40.79	86.28	26.41	2023	Maxwell[43]
14	n-type	761.3	40.22	85.13	26.06	2024	LONGi[37]
15	n-type	742.5	42.61	85.60	27.09	2024	LONGi[38]
16	n-type	743.4	42.62	86.19	27.30	2024	LONGi[21]

It benefits from the excellent properties of passivation contact, the efficiency of silicon solar cells exceeded 25%. Since then, all devices that exceed this mark, whether small or large area, with contacts on either side or back of the silicon wafer, have used at least one passivation contact material. The widespread success of passivation contacts have led to increasing research into ways of forming carrier selective junctions, resulting in a variety of approaches. The schematic representation of the role of passivation contact is shown in Fig. 4. In this review, the passivation contact layer is divided into a passivation layer and a carrier selection layer, and the research and exploration of each layer based on traditional SHJ solar cells are introduced, and promising opportunities towards higher conversion efficiency are emphasized. "Passivating contact", which may appropriately be called a "passivating junction",[54] encompasses several of the functions necessary for the efficient operation of a solar cell device: passivate surfaces and interfaces, provide a high conductivity for just one type of charge carrier, and establish a bridge between the work functions of silicon and silver (Ag) or aluminum (Al), the metals commonly used to form the electrodes. The passivation contact layer can generally be grown by chemical vapor deposition (CVD), including plasma enhanced chemical vapor deposition (PECVD) and hotwire chemical vapor deposition (HWCVD). Compared with PECVD, the film growth rate of HWCVD is relatively high and the order is better, and HWCVD can efficiently decompose H_2 to produce a very high density ($>10^{14}$ cm^{-3}) of H atoms, which helps to improve the passivation quality. However, HWCVD does not control the substrate temperature accurately enough during the deposition process, which will affect the deposition rate and crystallization rate of the film.[55]

4.1 Passivation layer materials

Excellent surface passivation is the key technology of high-efficiency c-Si cells,[56,57] it is necessary for the preparation of high-performance devices. The passivation mechanism of materials is usually divided into field passivation[58] and chemical passivation.[59] Field effect passivation reduces surface recombination by generating an electrostatic field at the interface through charge accumulation that drives photogenerated carriers away from the surface, such as Si_3N_4 and Al_2O_3; chemical passivation refers to through chemical bonds in materials with silicon surface suspension bonding, thus reducing the silicon surface suspension density and reducing deficiency trapping, reducing the recombination of photogenerated carriers, such as H in a-Si:H. The role of the passivation layer film in heterojunction solar cells is extremely important. At present, the passivation layers of crystalline silicon, mostly are a-Si:H and SiO_x materials.

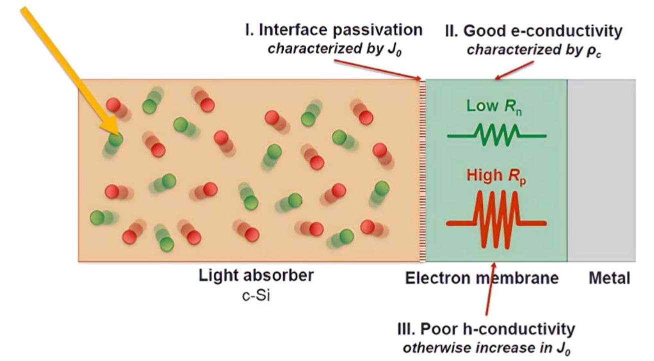

Fig. 4 Schematic representation of the role of passivation contact as an intermediate layer between light absorber and metal contact, the passivated contact layer forms different resistivity to electrons and holes to enable carrier selection (reproduced from ref. 53 with permission from Elsevier, copyright 2022).

4.1.1 a-Si:H material.

4.1.1 a-Si:H material. As a passivation material for silicon heterojunction solar cells, a-Si:H boasts the advantages of low process temperature, cost-effectiveness, pronounced passivation effect and excellent stability,[60] and the band gap and surface passivation of the a-Si:H passivation layer can be effectively regulated by adjusting the Si–H bonded state, LONGi achieved a high open circuit voltage of 761 mV in a flexible heterojunction solar cell (57 μm) prepared in October 2022, which is the current champion V_{OC}.[37] A key to the outstanding surface passivation is the prevention of epitaxial growth at the a-Si:H/c-Si interface.[61,62] There are few defect states at the interface between crystal silicon and a-Si:H passivation layer, however the epitaxial growth results in the interfacial region of the mixed phase, where the density of the interfacial defect states increases. Epitaxial growth leads to deterioration of the performance of heterojunction solar cells, especially affecting V_{OC}. Various companies and institutions have conducted in-depth research on a-Si:H. We can learn that different deposition conditions (such as substrate temperature, deposition frequency, *etc.*) will affect the passivation layer of amorphous silicon. The structure, hydrogen content, and thickness of the a-Si can be obtained by combining system deposition parameters, such as suitable temperature, optimal dilution ratio, chamber pressure, high silane depletion fraction, optimal electrode gap, *etc.*[63] Besides, according to the hydrogen balance theory, low-temperature annealing can further improve the passivation quality.

Substrate temperature is critical to improve solar cell performance. Fig. 5 shows the effect of substrate temperature on deposited amorphous silicon layers, which can be obtained that the a-Si band gap decreases with the increase of temperature. When the substrate temperature is about 210 °C, the lifetime is the highest, and the FF of the device is also the highest.[63]

In the PECVD system, different effects of intrinsic passivation layers are also deposited through different frequencies. Compared to the frequency of 40.68 MHZ, Hanergy Group use 13.56 MHZ through the RF-PECVD system, and the deposited film can achieve an efficiency advantage of 0.21%, and on a total area of 244.5 cm^2, obtain ISFH certified 25.11% efficiency.[47] Fig. 6 shows cross-sectional TEM images of deposition at different frequencies, respectively. VHF-PECVD-prepared a-Si produces more severe epitaxial growth, resulting in more light absorption. Low deposition rates produce non-dense thin films that prevent epitaxial growth of c-Si and improve passivation.

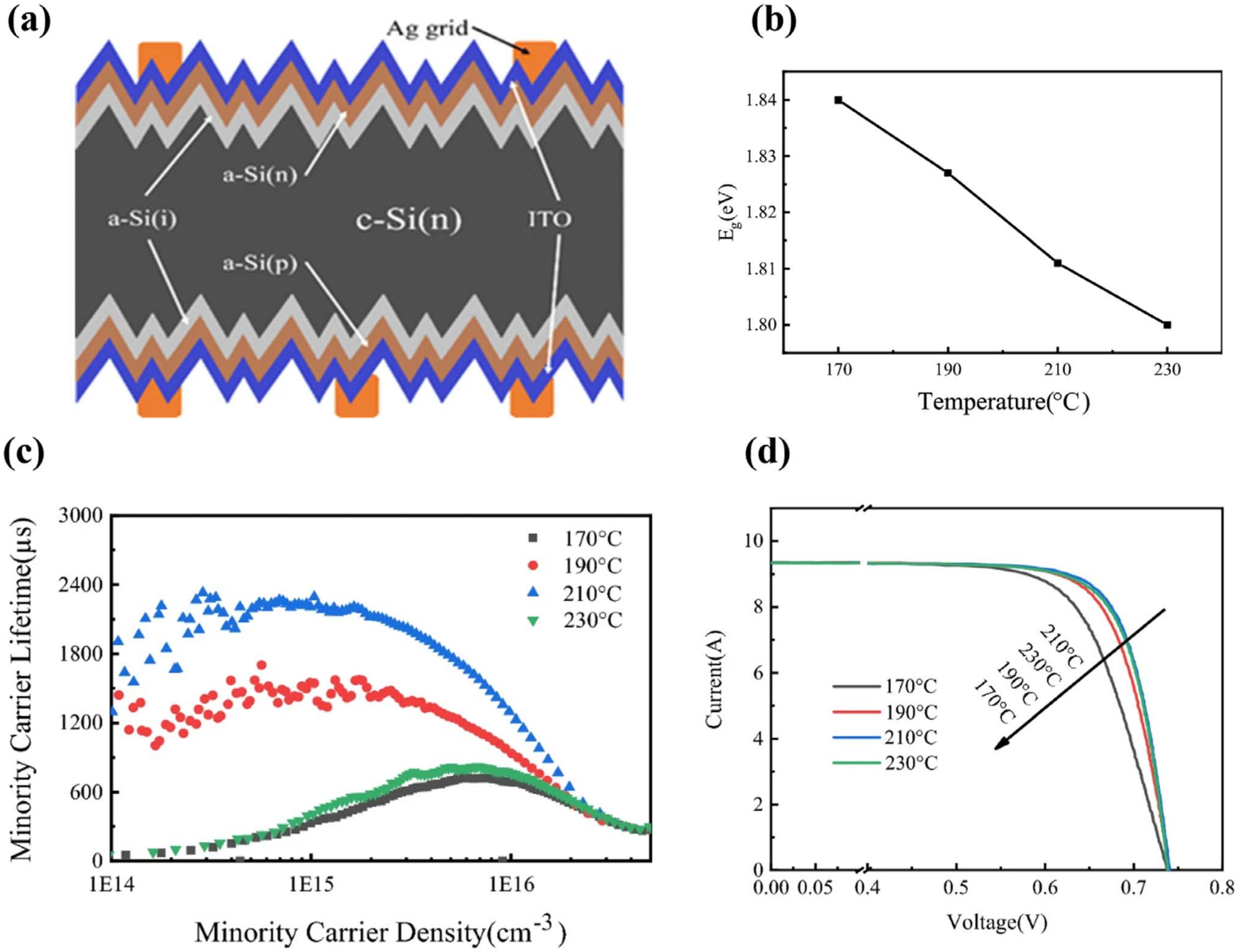

Fig. 5 (a) Double-sided SHJ structure (b) substrate temperature and a-Si:H function relationship, as the temperature increased, the a-Si band gap decreased from 1.84 to 1.80 (c) effect of temperature on a-Si:H minority carrier lifetime, optimal passivation results and high minority carrier lifetime are achieved at around 210 °C (d) influence of substrate temperature on *J*–*V* curve, prove the optimal passivation effect at about 210 °C (reproduced from ref. 63 with permission from Springer, copyright 2019).

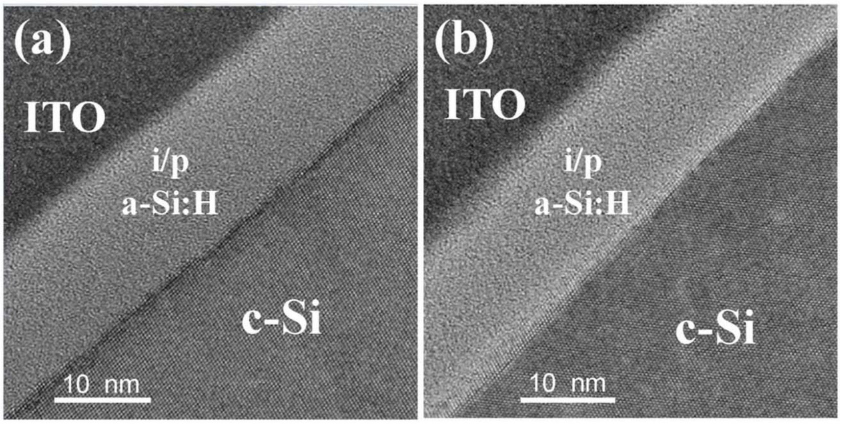

Fig. 6 Cross-sectional TEM images taken at the a-Si:H/c-Si interfaces with (a) RF-PECVD and (b) VHF-PECVD deposited i-a-Si:H layers. (a) TEM images deposited using RF (13.56 MHz) (b) TEM images deposited using VHF (40.68 MHz), thin films deposited at different frequencies have different deposition rates, and high deposition rates in VHF-PECVD can prevent epitaxial growth (reproduced from ref. 47 with permission from Elsevier, copyright 2020).

Therefore, the deposition frequency must be controlled to obtain better performance when the amorphous silicon is deposited under different conditions.

Under conditions of high pressure and high power, very thin, loose a-Si:H films with high structural factors deposited in pure silane plasma always form a mutant interface, and after the deposition of the p-a-Si:H layer, passivation will produce some degradation. National Institute of Advanced Industrial Science and Technology (AIST) utilizes an extremely thin low-density intermediate layer and a dense overlay, which ultimately leads to the preparation of high performance SHJ with a passivated a-Si/c-Si interface.[64] A double-layer passivation structure is formed through the buffer layer deposited by pure silane plasma, which effectively reduces the risk of epitaxial growth of thin films and plasma damage caused by hydrogen-diluted silane plasma.[65] On an area of 238.95 cm^2, a PCE = 22.43% was achieved. Solar Energy Technology Laboratory (STL) in Thailand has shown higher efficiency by replacing the a-SiO:H(i)/a-Si:H(i) tandem passivation layer with an a-SiO:H(i) tandem passivation layer, and the efficiency obtained was 19.4%. These experimental results show that the alloying and stacking of intrinsic layers can provide an efficient development path for SHJ solar cells by enhancing passivation and tuning photoelectric characteristics. To overcome epitaxial growth and recombination sites, many institutions have carried out changing the single-layer passivation layer to a multi-layer structure to improve the passivation quality.

It was found that for single intrinsic layer, surface passivation property is best just before the transition from amorphous to micro-crystalline,[66] presumably because the a-Si:H network is most relaxed in that case and comprises the lowest dangling bond density.[67] Therefore, careful control of the a-Si:H deposition parameters is necessary. Compared with monolayer structures, multilayer structures can reduce the requirements of monolayer film deposition through a series of treatments, *i.e.*, the combination of efficient hydrogenation and the avoidance of epitaxial growth.[65] A void-rich a-Si:H interfacial layer (i1) deposited in pure SiH$_4$ plasma in combination with a dense a-Si:H layer (i2) deposited in highly H$_2$ diluted plasma has been shown to increase the passivation quality of SHJ cells (compared to single intrinsic layers deposited in the transition zone between amorphous and micro-crystalline Si).[68] Multilayer structures are also considered to achieve good passivation. Fraunhofer Institute for Solar Energy Systems studied the excellent improvement of two-layer intrinsic amorphous silicon for n-type contact and p-type contact by changing the deposition parameters for the i1 layer and i2 layer respectively, as shown in Fig. 7, confirmed that the addition of dense i2 layer does not affect the contact resistance (ρ_c), and the use of porous i1 layer and hydrogen plasma treatment (i1 + HPT) significantly improved iV_{OC}. The i1 + HPT + i2 stacks (where i1 and i2 are both 3 nm thick) show the best passivation, but ρ_c is also the highest. i1 Layer is necessary for good passivation of holes and electronic contacts, but it is also primarily responsible for resistance loss.[69]

Though i-a-Si:H has excellent passivation effect, there are also some unsolved problems. Such as a-Si:H layer is greatly affected by temperature and began to deteriorate above 300 °C, and the passivation layer will produce hydrogen overflow at high temperature, so that the suspension bond cannot be passivated. The temperature in the production line must be precisely controlled to prevent hydrogen spillage at temperatures ranging from 200 to 300 °C. Unlike most other silicon solar cell structures, SHJ involves doped heat diffusion to form junctions. The implication is that any subsequent process step following the formation of a-Si:H passivation contacts must

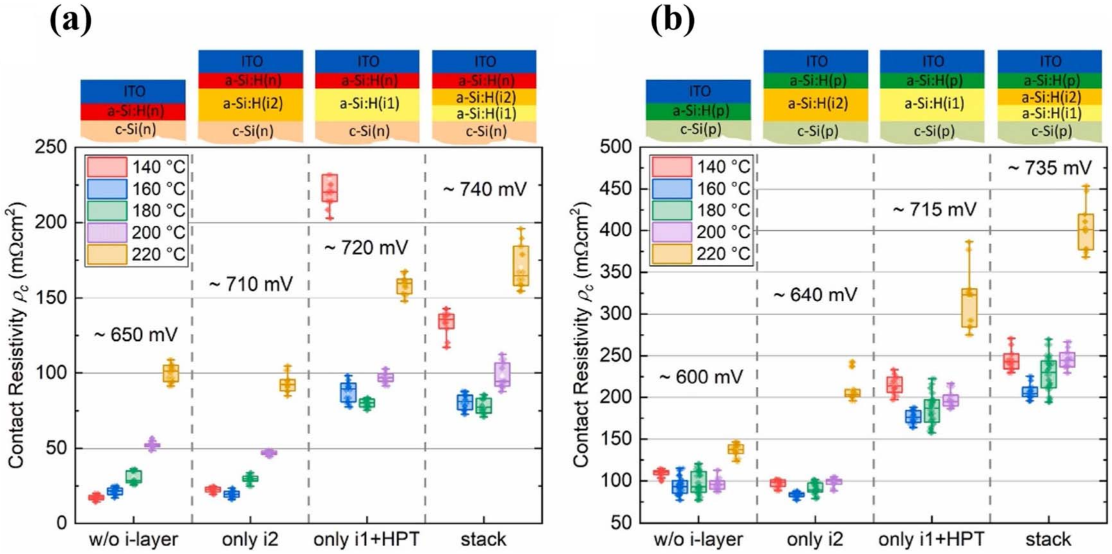

Fig. 7 Effect of multilayer structure on (a) n-type and (b) p-type contacts comprising different undoped a-Si:H layer (stacks) as indicated, different colors represent different cumulative post-deposition thermal treatments of 10 min each. At different temperatures, the V_{OC} of the double-layer intrinsic layer structure is increased by more than 20 mV compared with the single-layer intrinsic layer or the non-intrinsic layer structure on the n-type substrate and p-type substrate (reproduced from ref. 69 with permission from Elsevier, copyright 2022).

operate at temperatures below 300 °C. Consequently, fire protection through metallization becomes necessary, which entails the use of specialized and more expensive low-temperature metallic silver paste. Due to the low transverse conductivity of the a-Si:H layer, a transparent conductive electrode (TCO) is required at the top of the a-Si:H stack for transverse carrier transport, work function alignment, and anti-reflection. TCO and a-Si:H stacks produce some parasitic light absorption over a short wavelength range. This results in a 1–2 mA cm^{-2} reduction in J_{SC} compared to traditional doped diffusion junctions, which reduces device efficiency. In addition, the presence of non-negligible vertical contact resistivity through the a-Si:H stack also has an impact on device efficiency.[70]

4.1.2 a-SiO$_x$ material. Silicon oxide alloy, which is like the a-Si:H, chemical passivation is performed by reducing the interfacial density of the wafer surface. About carrier transport in SiO$_x$, there are two considerations here: (i) the carrier passes through the tunnel of the thin SiO$_x$; (ii) the rupture of the dielectric film creates the so-called pinhole.[71–73] To make the tunneling becomes the primary driving transport mechanism, carrier collection requires ultra-thin tunneled SiO$_x$ layers with a thickness of less than 1.5 nm.[74–76] For the case of thicker (>2 nm) SiO$_x$ layers, the transfer is pinhole driven, and during subsequent high-temperature annealing, the thicker SiO$_x$ layer eventually breaks/thins, allowing charge to flow,[77] this case, the trade-off between passivation and collection is related to the total pinhole area.[78] In the larger SiO$_x$ thickness range, two mechanisms (*i.e.* tunnel and pinhole) can exist at the same time.[79]

In the laboratory, PECVD is commonly used for the deposition of amorphous silicon films. In the preparation of SiO$_x$ in PRCVD, we typically tune the bandgap and conductivity of the material by introducing CO$_2$ into the reaction gas.[80] As shown in the Fig. 8a and b, in the absence of CO$_2$ ingress, an epitaxial layer is found between the a-Si:H/c-Si interface, and the

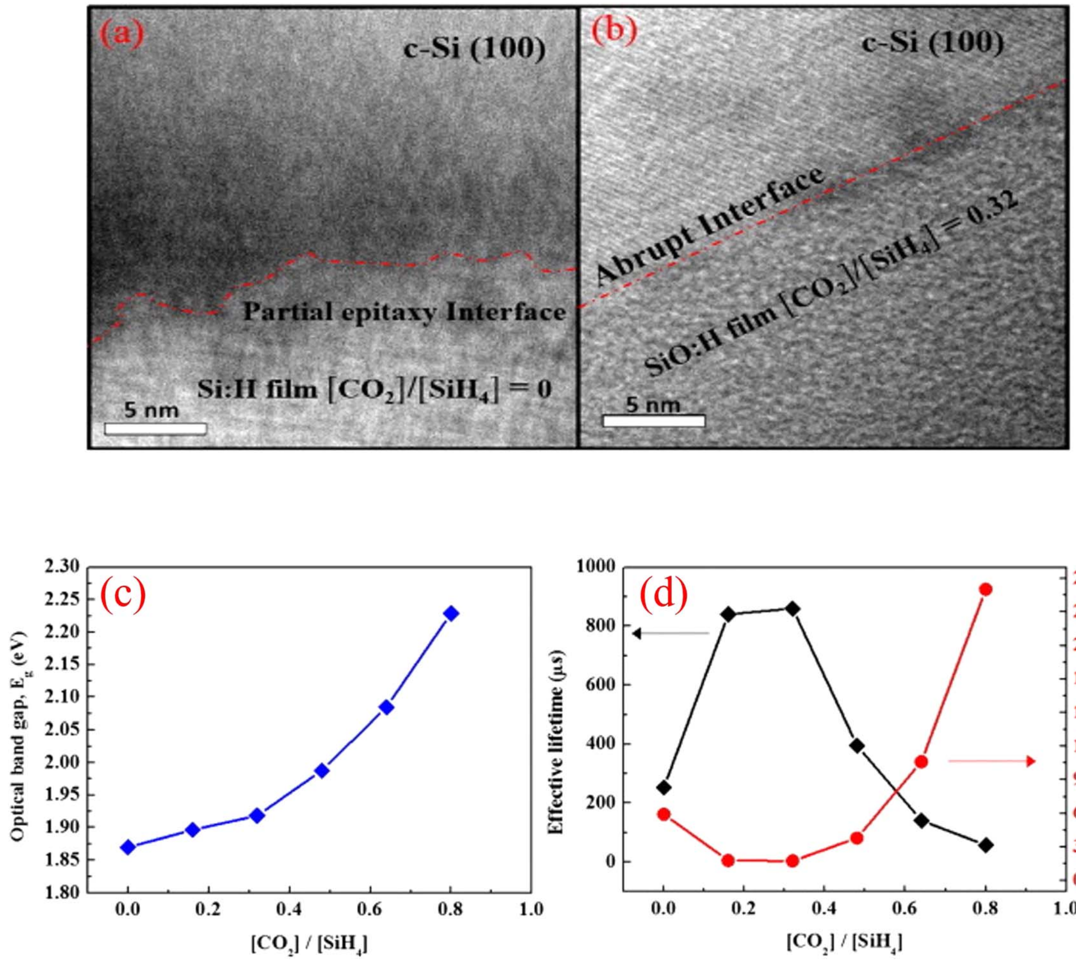

Fig. 8 (a) HRTEM image without CO$_2$, a partial epitaxial layer is found between the a-Si:H/c-Si interface, even though the passivation layer provided abundant hydrogen content (b) with CO$_2$/[CO$_2$]/[SiH$_4$] = 0.32, the partially epitaxial phase was suppressed and an abrupt interface was formed with excellent surface passivation by terminating the dangling bonds (c) curve of band gap with CO$_2$ concentration (d) the results of τ_{eff} and the upper limit of S_{eff} for various ratios of [CO$_2$]/[SiH$_4$], the τ_{eff} increased and reaches the maximum value of 860 μs (S_{eff} = 17.4 cm^{-1} s^{-1}) for increasing the ratio of [CO$_2$]/[SiH$_4$] from 0 to 0.32. After the maximum values, τ_{eff} rapidly decreased with an increasing CO$_2$ gas flow rate due to the lack of abundant hydrogen content in the a-SiO:H films (reproduced from ref. 81 with permission from Elsevier, copyright 2015).

interface also exhibits a certain roughness, which impairs the passivation quality. The AIST tunes the material properties by controlling the CO_2 ratio, and the observed change of E_g in the range of 1.87 to 2.23 eV,[82] which is shown in the Fig. 8c. Absorption in a-SiO:H films decreases due to the gradual increase of Si–O bonds in the membrane. As shown in the Fig. 8d, after the doping concentration is greater than 0.32, τ_{eff} decreases rapidly with the increase of CO_2 gas flow due to the lack of abundant hydrogen content in the a-SiO:H film. However, when excess oxygen atoms are bonded into the a-SiO:H film, the passivation quality deteriorates, which leads to the formation of silicon dangling bonds in the interface between the c-Si wafers, resulting in ineffective passivation through the film.

The PECVD-grown a-Si:H and a-SiO_x:H thin films are usually used as passivation layers in the SHJ solar cells. The extremely thin intrinsic i:a-SiO_x:H doped with oxygen is beneficial for the inhibition of epitaxial growth, but it is associated with a reduction in the electrical properties of the passivation contact. Based on an earlier HJT efficiency record of 25.11% (an ultra-thin 0.5 to 1.0 nm buffer layer rich in H content was utilized to improve passivation), LONGi introduced O-terminated Si surfaces grown by a self-limiting wet chemical oxidation process (using a HF/H_2O_2 solution) to inhibit Si epitaxial growth. Subsequently, 2–3 atomic layers of oxidized amorphous silicon subnanometer layer (<0.5 nm; i:a-SiO_x:H(1) $x \approx 10$ at%) are formed. The ultra-thin i:a-SiO_x:H(1) passivation layer prevents the periodic outward extension of the c-Si crystal arrangement, while minimizing the effect of oxygen doping on the electrical properties of the passivation contacts. In the second step, two increasingly dense a-Si:H(i) layers are deposited on i:a-SiO_x:H(1), as shown in Fig. 9a. The treatment of these layers minimizes the epitaxial growth region, which leads to more defective interfaces and provides the hydrogenation of the interface. Correspondingly, it reduces defect activity and enable efficient carrier transport. LONGi demonstrates a sandwiched passivation layer (i0/i1/i2) with an H-rich porous first layer (i0) deposited on oxygen-modified c-Si surface, see in Fig. 9c.[21]

4.2 Carriers selective layer materials

In conventional SHJ cells, although the doped a-Si:H window layer is only a few nanometers thick (5–10 nm), it still parasitically absorbs a large amount of incident light, which results in a 1.6 mA cm^{-2} reduction in the J_{SC} of the solar cell.[84,85] In addition, the a-Si:H stack ($n \sim 4.0$) increases the reflection of the TCO (632 nm, $n \sim 2.0$)/Si ($n \sim 3.8$) interface.[29] Carrier selection using doped a-Si has achieved 25% efficiency, and to achieve more efficient carrier selectivity, numerous institutions have conducted many exploration experiments on carrier selection layers. To reduce parasitic absorption and reflection, hydrogenated nanocrystalline silicon oxide (nc-SiO_x:H) has proven to be a very promising alternative to commonly used doped a-Si:H.[86–91] At the same time, the alloying of different elements to produce wider bandgap materials is also a promising development.[85,92,93] It is similar to the intrinsic layer, the doped layer can also be stacked to achieve better material properties.

Depending on the polarity of the carriers to be collected, the passivation contact is classified into electron-selective and hole-selective contacts, where the carrier transport layer (CTL) is also referred to as the electron transport layer (ETL) and hole transport layer (HTL), respectively. When contacting ETL or HTL with c-Si, the energy band alignment at the c-Si/CTL interface is key to understanding carrier transport mechanisms.

4.2.1 Nanocrystalline silicon or nanocrystalline silicon oxide. The selective transport of charge carriers has a great

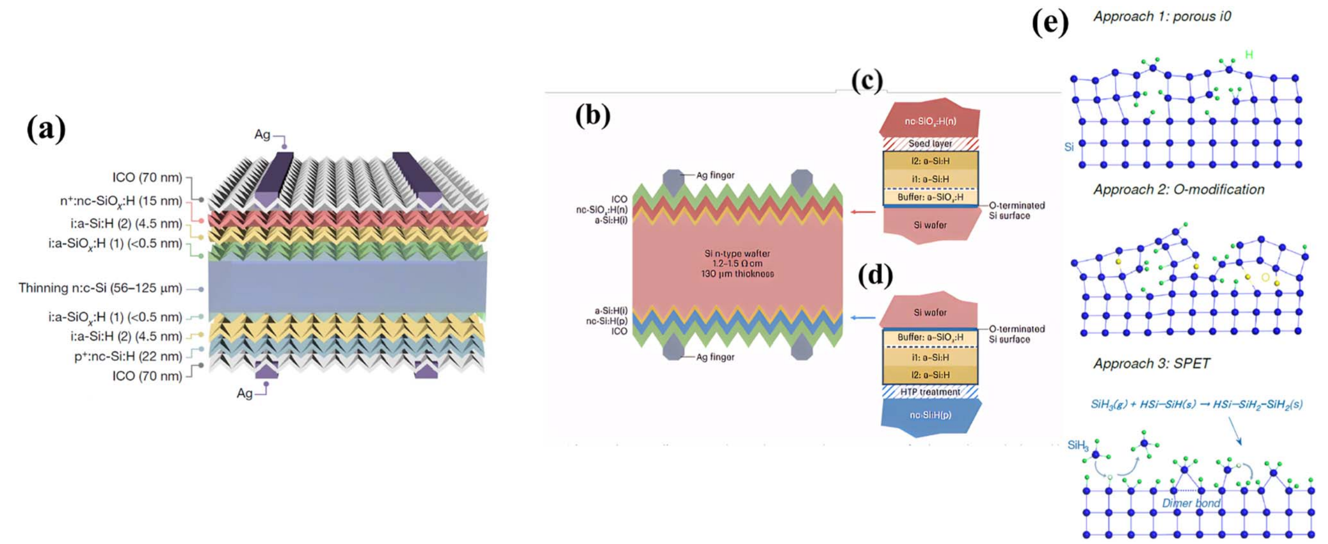

Fig. 9 (a) Structure schematics of the flexible SHJ solar cells with a two-stage composite gradient passivation process (reproduced from ref. 37 with permission from Springer Nature, copyright 2024). (b) Device structure of the solar cell with an efficiency of 26.81%. (c and d) Schematic representation of the front and rear surface fields (reproduced from ref. 83 with permission from Springer Nature, copyright 2023). (e) Three approaches for epitaxy growth suppression, which is a sandwiched passivation layer (i0/i1/i2), with an H-rich porous first layer (i0), deposited on oxygen-modified c-Si surface (reproduced from ref. 21 with permission from Springer Nature, copyright 2024).

impact on the performance of SHJ. SHJ technology often uses a doped hydrogenated amorphous silicon (a-Si:H) layer as the carrier selective contact layer, called electron-selective contact layer (ESC) and hole-selective contact layer (HSC).[94] The electrical performance of the solar cells depends strongly on the net doping of both the ESC and HSC layers. However, there are many problems existed, such as: (i) parasitic absorption of the frontal a-Si:H layer in the short wavelength region (<500 nm), resulting in a decrease in J_{SC}; (ii) the conductivity of the doped a-Si:H layer is very low (σ < 10^{-4} S cm^{-1}); (iii) relatively high activation energy (E_a > 250 meV),[95,96] low σ leads to reduced conductivity and high E_a leads to high work function. Using doped nanocrystalline silicon (nc-Si:H) films as the carrier selection layer of SHJ cells can significantly improve the performance of solar cells. In the nc-Si:H thin film. Silicon nanometer microcrystals are embedded in the amorphous silicon matrix, and H is usually preferentially located in the grain boundary or amorphous phase. With the increase of crystallinity, the transparency and conductivity of the silicon film will increase, which directly enhances the electrical conductivity of solar cells.[97] LONGi fabricated a solar cell with an efficiency of 26.81% in 2022 using p-nc-Si:H, which has an improved conductivity of four orders of magnitude and E_a below 110 eV.[35] The cross-sectional TEM images of the HSCs based on p-a-Si:H and p-nc-Si:H are shown in Fig. 10a and d. The p-nc-Si:H layer has a higher degree of crystallinity relative to i-a-Si:H and p-a-Si:H, which is achieved through the lateral merging of nanocrystalline domains embedded within the amorphous phase. Fig. 10b and c exhibit the band structure of a solar cell made of two different materials. Compared with p-a-Si:H, p-nc-Si:H layer presents good band bending in the surface region of c-Si, which provides a lower and sharper energy barrier for SHJ and facilitates the collection of holes through tunnels on the HSC.

Work function is one of the main factors affecting performance, and the work function of the doped a-Si:H layer can be changed by increasing its doping concentration or otherwise replaced by the doped hydrogenated polysilicon layer.[99] Many research institutions have conducted a lot of researches on nanocrystalline silicon, and obtained nanocrystalline silicon with different properties by regulating one or more parameters of PECVD.[100] By controlling the hydrogen dilution ratio and the ratio of B_2H_6 to SiH_4, the optical band gap, crystallinity and conductivity of the film can be adjusted, and it is observed that

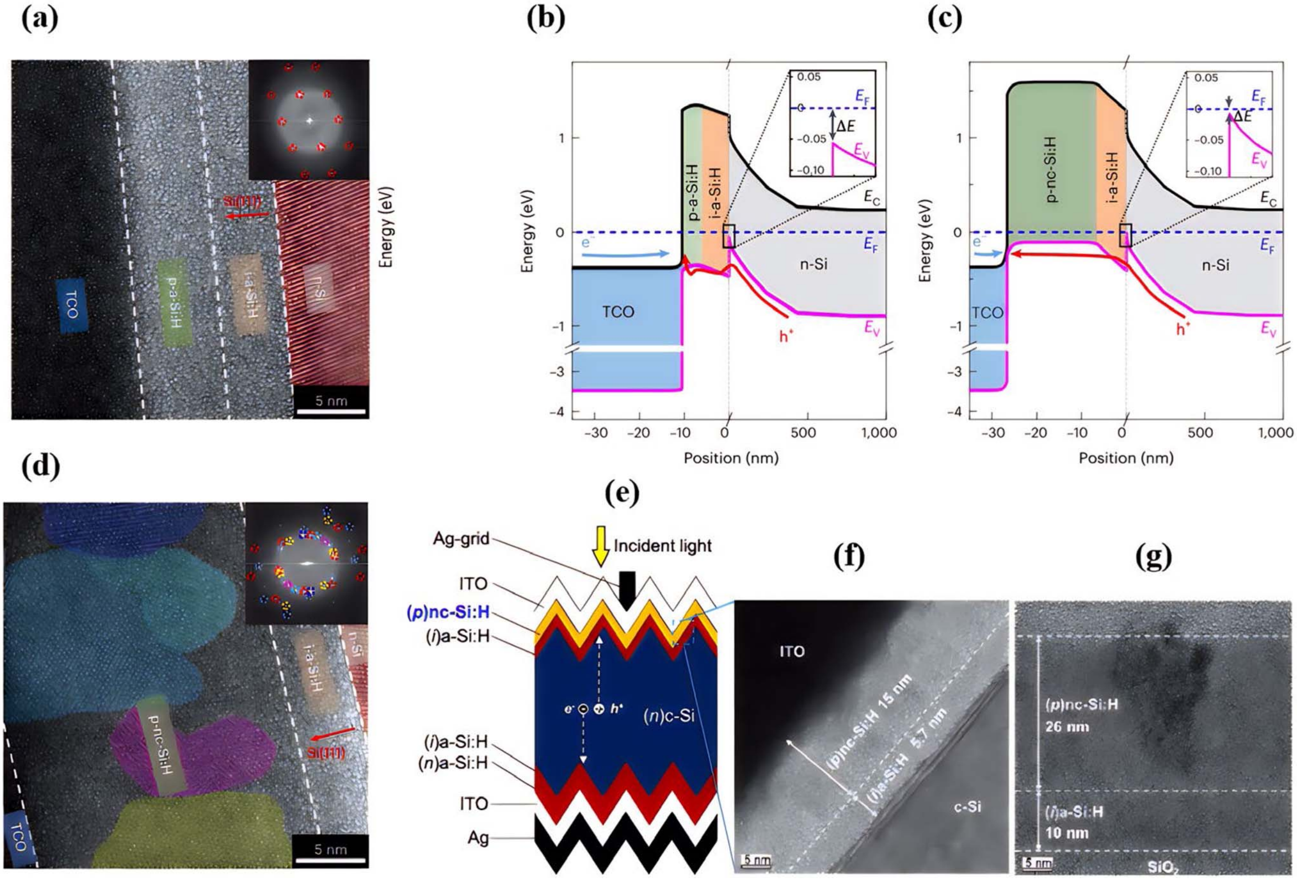

Fig. 10 (a and d) TEM images of TCO–p-a-Si:H–i-a-Si:H–n-S (a) and TCO–p-nc-Si:H–i-a-Si:H–n-Si. (b) structures. (b and c) Equilibriumband diagrams of HSCs based on p-a-Si:H (b) and p-nc-Si:H (c) related to the cross-sectional structures in (a) and (d) (reproduced from ref. 35 with permission from Springer Nature, copyright 2023). (e) Schematic diagram of solar cell structure (f) TEM image of textured and (g) flat surface representation under the same deposition conditions, it is seen that the thicknesses of these layers are thinner for textured Si than for planar substrate due to the larger surface area of the textured Si (reproduced from ref. 98 with permission from Wiley, copyright 2020).

nc-Si shows a strong dependence on the conductivity and crystallinity fraction of the film thickness. Due to enhanced field effect passivation (AFP), the effective lifetime of the sample also increases after doping on nc-Si:H. Silicon is an indirect bandgap semiconductor with a low band gap, but silicon nanocrystals change with nc-Si:H size due to the quantum confinement effect,[101] so amorphous silicon layers with different bandgaps can be generated to achieve better photoelectric performance.[46,47] The nc-Si:H is considered as a more advantageous alternative to the a-Si:H emitter and BSF layers due to nc-Si:H's higher electrical conductivity giving rise to lower series resistance. The conductivity of the doped microcrystalline silicon layer depends largely on the degree of crystallization and the concentration of effective doping, and as the doped gas flow increases, the crystallization will be suppressed, so we must compromise the doping efficiency and the degree of crystallization. Matsumura *et al.*[102] presented that the properties of as-grown silicon films and wafers could be tuned using catalytic doping (Cat-doping) process even after depositions. This Cat-doping process is a post-doping process where dopant gases can be decomposed by catalytic cracking reaction at the hot surface of the wires and, subsequently, the decomposed species contribute to the doping of the silicon surface at a shallow depth. Consequently, the conductivity of Si films can be further improved using this technique.[103]

As shown in the Fig. 10e–g,[98] the AIST designed nc-Si:H(p) for different processes, and Fig. 10b and c shows the cross-sectional TEM image of the stacked nc-Si:H(p)/a-Si:H(i) layers deposited on the textured surface and the planar surface respectively by RF-PECVD under the same deposition conditions. Due to the difference in parasitic absorption loss, the J_{SC} decrease of nc-Si:H(p) is much lower than that of (p)a-Si:H with the increase of the hole contact layer. Although nanocrystals have good characteristics, they need to be applied in well-designed solar cell structures to highlight the advantages of nc-Si:H(p). The deposition rate of nc-Si:H(p) (R_d < 0.02 nm s^{-1}) is lower than that of a-Si:H(p) ($\approx$0.14 nm s^{-1}), and it also plays a role in increasing atomic hydrogen, promoting passivation. Another beneficial effect of using the nc-Si:H(p) contact is to reduce the contact resistivity at the interface, resulting in FF improvement.[104] Nevertheless, the TCO layer covering the front and rear of the SHJ solar cell needs to be optimized to balance optical transparency, conductivity, and material cost.[54] When IWO replaced ITO, efficiency was further improved.

To increase the optical bandgap and reduce blue light loss, SHJ solar cells, the optical band gap can be widened by the introduction of oxygen.[104,105] When the nc-SiO$_x$:H(n) deposition time increases, atomic hydrogen accelerates the nucleation and growth of silicon micro-grains[106] and voids may form in the amorphous silicon network near the n-c-Si surface due to the weak bonds are corroded by the active atomic hydrogen. When the deposition time of nc-SiO$_x$:H(n) increases, the conductance monotonically increases, which is due to the increase in the crystallinity of the sample. Between the microcrystalline silicon grains in the layer, the amorphous component is reduced, and the carrier transport between the microcrystalline grains is improved.[107] Doped nc-SiO$_x$:H has excellent optical and electrical properties and is one of the most promising materials for SHJ solar cells. Currently, LONGi and Suzhou Maxwell use nc-SiO$_x$:H as the front surface field for SHJ solar cells, and their short circuit currents both exceed 40.50 mA cm^{-2} and reach up to 41.45 mA cm^{-1}.[35,37,43]

The nc-SiO$_x$:H(n) increases light transmission but decreases crystallinity. Sichuan University improved the crystallinity of the nc-SiO$_x$:H(n) layer by controlling the high-phosphorus-doped seed crystal layer to form a nucleation layer.[107] It can be observed that the light transmission increases after the formation of silicon-oxygen alloy, and then through appropriate PH$_3$ treatment, the crystallization is enhanced and the electrical properties are improved. The nc-SiO$_x$:H(n), evolved from the amorphous phase, grows in columns, and has different orientation, and the introduction of oxygen breaks the Si–Si bonds, making it difficult to grow individual crystals.[108] From Fig. 11, when the thickness of the nc-SiO$_x$(n) layer reached to 30 nm, a significant increase in τ_{eff} and iV_{OC} was observed, and the J_0 value was about 1.68×10^{-14} A cm^{-2}, indicating the breaking of the silicon–hydrogen bond, the diffusion of hydrogen in the C–Si substrate, and the diffusion of phosphorus through the silica layer in the n-type substrate, the passivation quality is enhanced by the addition of the tunnel oxide layer. At an annealing temperature of about 950 °C, the passivation of the field effect due to carrier selectivity decreases and the chemical passivation of ultrafine SiO$_2$ is improved.

Solar cell efficiency can also be improved by controlling different concentrations of doped nc-Si:H(p) stacking. Zhou *et al.*[109] studied the effects of single-layer and multi-layer p-type emitters, including boron-doped hydrogenated nanocrystalline silicon (nc-Si:H) and/or boron-doped hydrogenated nanocrystalline silicon oxide (nc-SiO$_x$:H) films, on the device performance of SHJ solar cells. The novel sandwich-like p-type layer consisting of p-nc-Si:H/p-nc-SiO$_x$:H/p$^+$-nc-Si:H triple layers is proved to be the optimal emitter/window layer, which can be contributed to its high crystallinity, high conductivity and wide bandgap, the final device results are shown in Fig. 12b. This demonstrates the advantages of the multilayer structure, and provides us with directions and ideas for the optimization of the carrier selection layer.

The use of multilayer structures instead of single layers can enhance the SHJ passivation quality and thus improve V_{OC}, and multiple layers are usually beneficial to obtain thin layers with sufficient performance.[90] At present, continuous research is also being carried out on multilayer structures, and the band gap will also widen after the introduction of amorphous silicon into C.[110,111] As can be seen in Fig. 13, the wide bandgap of n-nc-SiC:H ensures high optical clarity, and the double-layer design achieves good passivation and high conductivity, improved the performance to J_{SC} = 40.87 mA cm^{-2}, FF = 80.9%, and η = 23.99 ± 0.29%. Due to the coexistence of high hydrogen concentration at the n-c-Si/SiO$_2$ interface and passivation of strong field effects, the passivation mass of SiO$_2$/n-nc-SiC:H contact reaches iV_{OC} of up to 740 mV.[48]

Therefore, the passivation contact avoids direct contact between metal and silicon wafer, reduces interface recombination, and ensures the transport of major carriers. The thin-

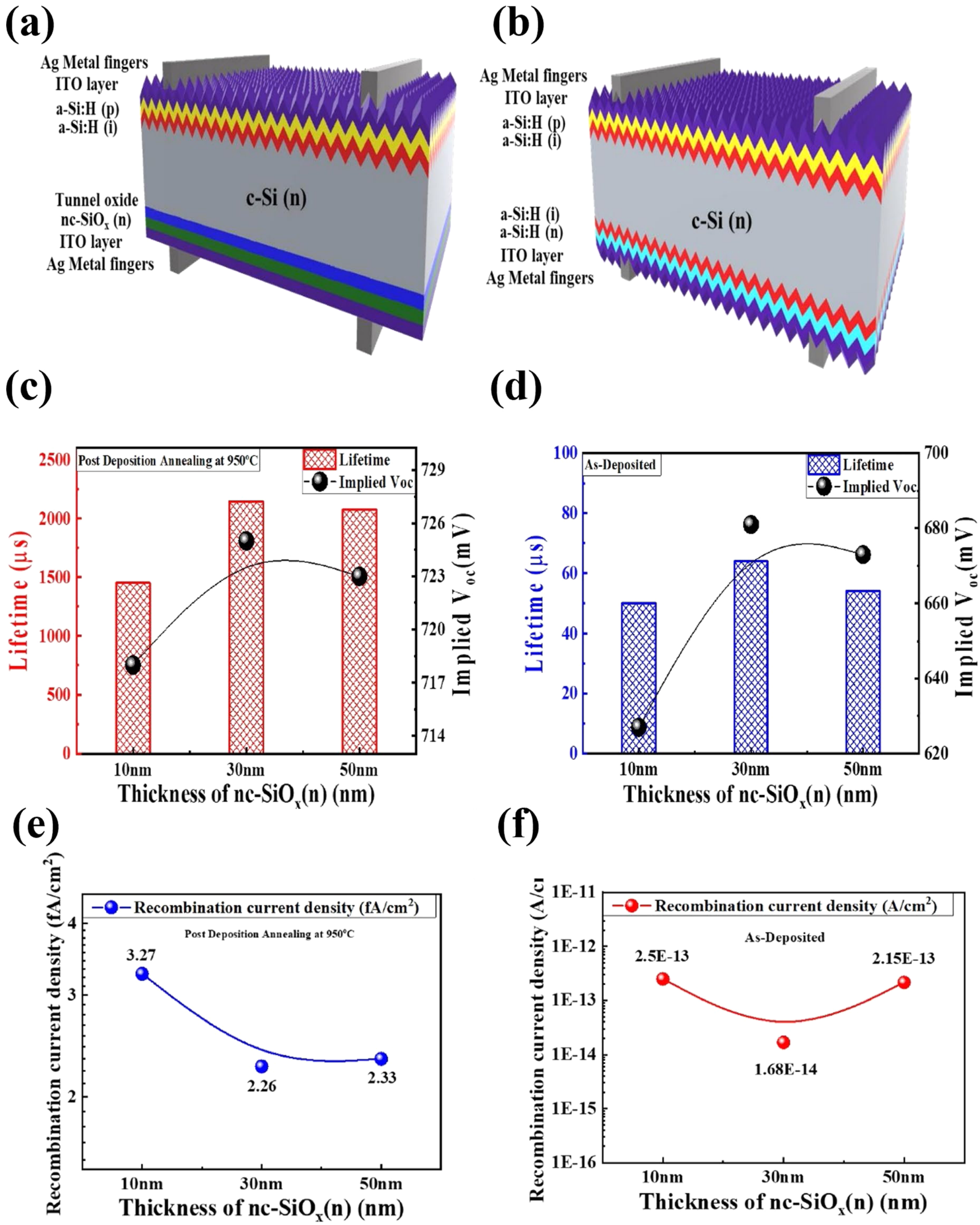

Fig. 11 (a) nc-SiO$_x$ doped layer structure and (b) contrast structure (c) iV_{OC} and minority carrier lifetimes of samples with three different nc-SiO$_x$(n) layer thicknesses after post-deposition annealing (PDA) measured at an injection level of 1 × 10^{15} cm^{-3} (d) Minority carrier lifetimes and iV_{OC} for three different nc-SiO$_x$(n) layer thicknesses in as-deposited state measured at an injection level of 1 × 10^{15}cm^{-3} (e) the recombination current densities for three different nc-SiO$_x$(n) layer thicknesses in as-deposited state (f) rear recombination current densities of nc-SiO$_x$(n)/SiO$_2$/(n)c-Si/SiO$_2$/nc-SiO$_x$(n) symmetric samples with three different nc-SiO$_x$ (n) layer thicknesses (reproduced from ref. 108 with permission from Elsevier, copyright 2022).

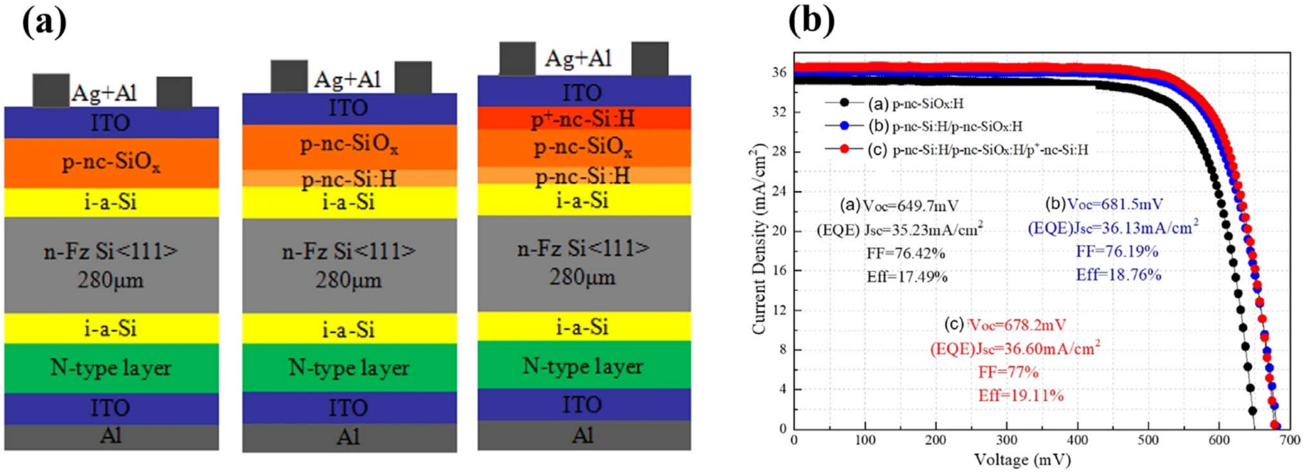

Fig. 12 (a) Diagram of a stacked structure device, from left to right are the sandwich-shaped emitter of p-nc-SiO$_x$:H monolayer, p-nc-Si:H/p-nc-SiO$_x$:H bilayer, p-nc-Si:H/p-nc-SiO$_x$:H/p$^+$-nc-Si:H triple layers. (b) Three different results result in the *J*–*V* curve, the double-layer mechanism or sandwich structure shows excellent passivation effect compared to the single-layer structure, achieving higher efficiency (reproduced from ref. 109 with permission from Springer, copyright 2021).

film materials for both the front and rear surface fields must exhibit high dark conductivity, sufficient carrier-selective properties, and sufficiently small contact resistance properties. In addition, higher optical transmittance is required for thin film materials in the front surface field and improved reflection in the rear surface field as a way to increase the efficiency of SHJ solar cells.

4.2.2 Metal compound and organic materials. In addition to doped crystalline or amorphous silicon, there exist numerous materials that can perform the function of selecting electrons or holes when deposited on a silicon wafer. The initial motivation for exploring such materials was to overcome the optical limitations imposed by doped a-Si:H. In fact, Battaglia *et al.*[111] demonstrated the improved J_{SC} by replacing the a-Si(p):H layer at the front of the SHJ solar cell with MoO$_x$, whose wide optical bandgap and high work functions (about 6 eV) make it attractive. These materials include alkali/alkaline earth metal compounds (AMCs), transition metal oxides (TMOs), and transition metal nitrides (TMNs) that are specialized for rare earth compounds (RECs), organic materials, and low work function

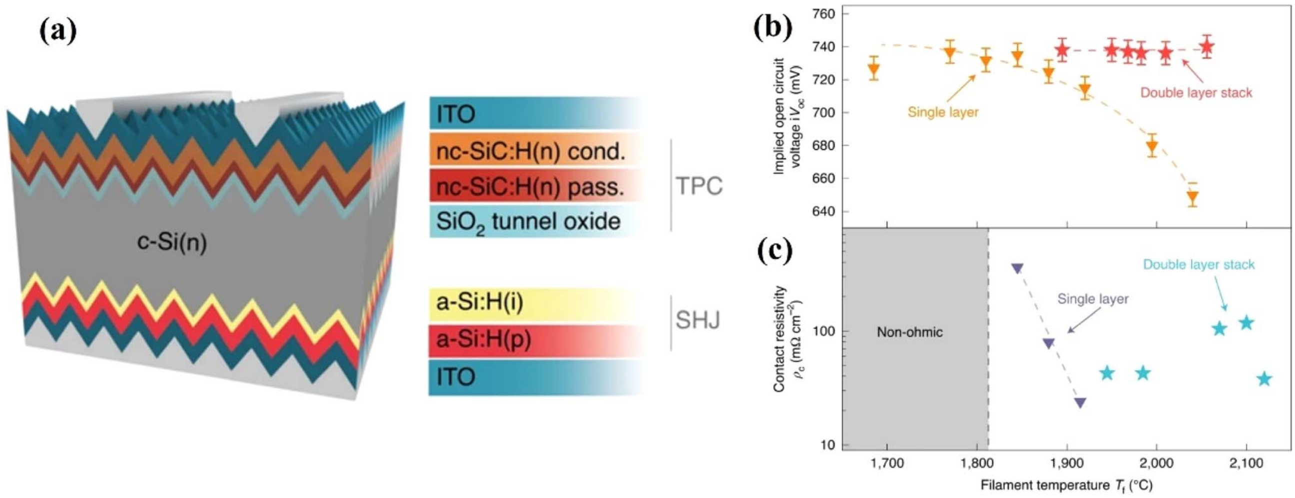

Fig. 13 (a) Schematic diagram of a double-layer structure solar cell, using an n-type wafer with a TPCon front side using nc-SiC:H(n)/SiO$_2$ stack. The back side consists of intrinsic and p-type hydrogenated amorphous silicon (a-Si:H(i/p)) and an ITO layer (b) effect of single-layer structure and bilayer structure on iV_{OC} and (c) ρ_c at different temperatures (reproduced from ref. 48 with permission from Springer Nature, copyright 2021). Stars show the results for double nc-SiC:H(n) layer (thickness of 9 + 25–30 nm) stack, where T_f of the passivation layer is fixed at 1775 °C and T_f for the conductive layer is varied according to the *x* axis. The vertical error bars represent the standard error for each measurement in the photoconductance measurement. The grey box marks the area where the contact resistivity could not be evaluated due to non-ohmic behaviour of the measured data in the case of single nc-SiC:H(n) layers. One sample was used for each data point in the iV_{OC} and ρ_c measurement. Dashed lines are guides to the eye.

(WF) metals. In practice, most of these materials lack the ability to passivate surface defects and require additional steps to deposit the passivation interlayer. Typically choose low-work function (WF) materials as electron-selective layers and high-work function (WF) materials as hole-selective layers. Taking the dopant-free wideband gap TCO as an example, Fig. 14 shows the carrier transport mechanism when four different types of TCOs are used as carrier selection layers.

Among the wide-bandgap transition metal oxides (TMOs), for ETL, the energy band arrangement of c-Si/ETL is shown in Fig. 14a. ETL materials are essentially n-type wide-bandgap semiconductors, and they should exhibit a sufficiently small conduction band offset (ΔE_C) with respect to c-Si so that electrons in c-Si can be easily transferred to the ETL, while a large valence band offset (ΔE_V) is required to block holes, the ETL materials including SnO_x,[115,116] ZnO_x,[117] TiO_x,[118,119] GaO_x,[120] MgO_x,[121] NbO_x,[122] and so on. In 2016, the high-efficiency "dopant-free asymmetric heterojunction" solar cell was reported and achieved a conversion efficiency of 19.7%.[123] A second layer of TiO_x passivation was added to the LiF_x/Al electron-selective contact while maintaining bifacial metallization, resulting in an increased efficiency of 20.7%,[113] as shown in Fig. 14e. In addition, the IBC (finger back contact) device structure and MgF_x electron-selective contact achieved efficiency of 22.1%.[124]

For HTLs, there are two main theories, one of which is similar to c-Si/ETL and the other is tunneling effect. The first theory suggests using p-type wide-bandwidth semiconductors as HTL, such as NiO,[125] Cu_2O.[126] The ΔE_V at the c-Si/HTL interface is small enough to allow for hole transportation from c-Si to HTL, while electrons are blocked due to the large ΔE_C. This approach is theoretically feasible. However, the interface between c-Si and the HTL often has a high density of interfacial defects, resulting in a high contact resistance. Additionally, the concentration of holes in the material is low, leading to poor hole conductivity and insufficient hole

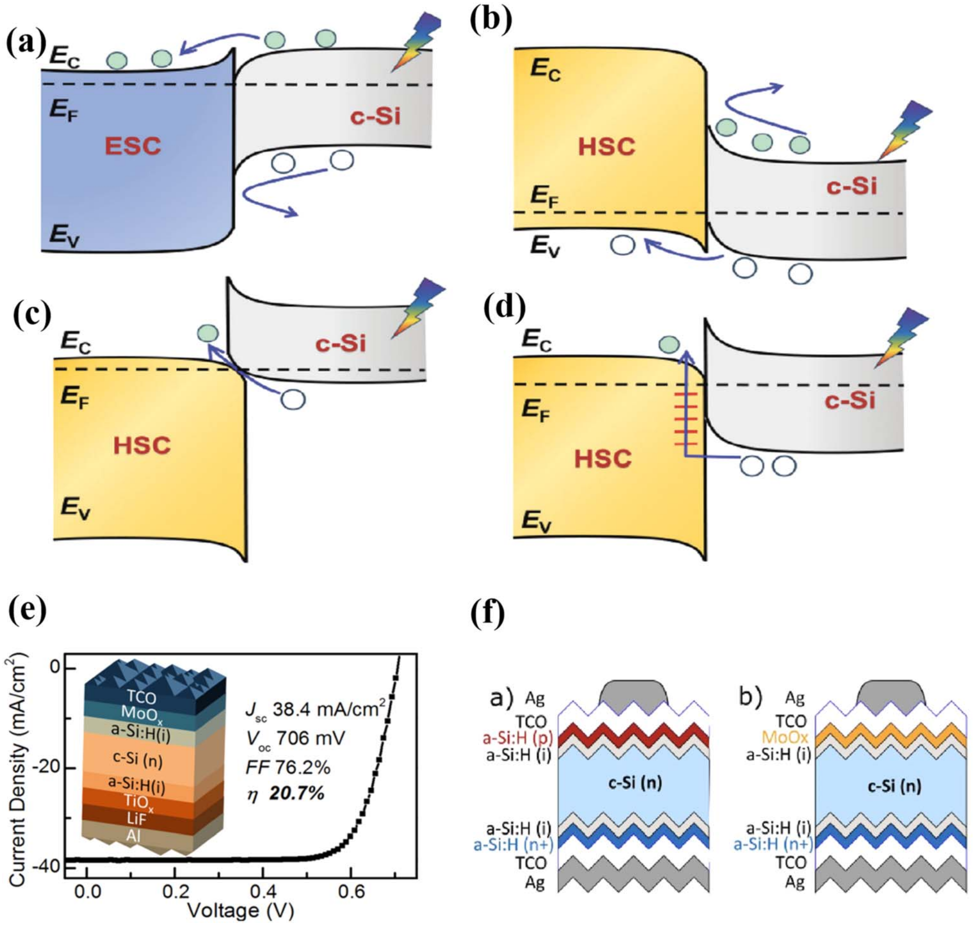

Fig. 14 (a) Band arrangement between n-type ETL material and c-Si, where low ΔE_C facilitates electron transport and large ΔE_V blocks holes. (b) Band arrangement between p-type HTL material and c-Si, where low ΔE_V facilitates hole transport and large ΔE_C blocks holes. The band alignment between n-type high-WF TMOs and c-Si, when the E_C of TMOs is higher than the E_V of c-Si, holes will transport through the (c) B2B tunneling mechanism, and anyway, when the E_C of TMOs is a little lower than the E_V of c-Si then the (d) TAT is dominant (trap-assisted tunneling effect) (reproduced from ref. 112 with permission from Wiley, copyright 2024). (e) Schematic diagram of DASH (dopant-free asymmetric hetero-contacts) solar cell structure with the TiO_x/LiF in the front-side and MoO_x in the rear-side (reproduced from ref. 113 with permission from American Chemical Society, copyright 2018). (f-(a)) Standard SHJ and (b) MoO_x-based cell schema (reproduced from ref. 114 with permission from Elsevier, copyright 2020).

selectivity of the contact. Another theory applies to n-type high work function (WF) transition metal oxides (TMOs),[127] which can work well as efficient HTLs due to their high WF, such as MnO_x (Fig. 14f),[118] WO_x[128,129] and V_2O_x,[130] which mainly relies on band-to-band (B2B) tunneling effect or trap-assisted tunneling effect (TAT). When the high WF TMOs are in contact with c-Si, the energy band alignment will cause a sharp upward energy band bending on the c-Si surface. The conduction band of these high-WF TMOs is relatively close to the valence band of c-Si, so the photogenerated holes gathered in the valence band of the c-Si absorber can cross the contact interface through the tunneling effect and complex with the electrons in the conduction. The bands of the high-WF TMOs are shown in Fig. 14c and d.

In addition to metal compounds, there are many reports on the carrier transport of other organic materials. Commonly used organic electron transport layers such as poly(ethylene oxide) (PEO),[131] branched polyethyleneimine (PEI)[132] and C60 pyrrolidine Tris-acid (CPTA)[133] have been used in many applications.[134,135] Reichel *et al.*[134] promoted the performance of n-type c-Si solar cells with front boron diffusion up to 17.5% when using L-histidine and/or fluorine surfactants as a whole-area back-surface electric field, as shown in Fig. 15a. In addition, He *et al.*[133] improved the performance of n-type c-Si solar cells by independent optimization of hole/electron selective contacts relying only on a solution-based process, with the efficiency of poly(3,4-ethylenedioxythiophene): poly(styrenesulfonate)/n-silicon (PEDOT:PSS/n-Si) HSCs boosting from 12.6% to over 16.7%, as seen in Fig. 15b and c. These materials can effectively improve the contact resistance characteristic of the interface and enhance the carrier selection properties through various mechanisms, but the inherent defects in the surface passivation of these materials lead to the still low efficiency of solar cells. At the same time, most of their preparation methods are solution methods, which are not as simple and fast as the traditional CVD and PVD preparation, resulting in their large-scale applications still have obvious disadvantages.

Commonly used organic hole transport layers such as poly(3,4-ethylenedioxythiophene) polystyrene sulfonate (PEDOT:PSS)[136] have been extensively studied. PEDOT:PSS, should be able to form a conductive passivation material because the PSS species has an excellent passivation effect, being comparable to that of high-temperature annealed SiO_2, and PEDOT has a good conductivity, like that of ITO.[137–139] By combining PEDOT and Nafion solution to form a composite film, Hebei University experimentally found a coexistence region with good electrical conductivity and passivation and called it PEDOT:Nafion, Nafion film can provide excellent passivation effect, comparable to the best a-Si:H(i) in the photovoltaic field.[140] A passivation-conductivity phase plot was made, and selectable conductivity and passivation were achieved by controlling the PEDOT/Nafion ratio. This led to the development of an organic passivation contact cell concept where passivation and hole selectivity occur at the back interface of PEDOT:Nafion/Si organic-inorganic hybrids, eliminating the need for high-temperature processes and complex laser turn-on steps. Commonly used metal compounds and organic materials are summarized in Table 3.

5. Other components of SHJ

5.1 Transparent conductive materials (TCMs)

TCM plays a vital role in SHJ solar cells, it is not only the conductive electrode of the solar cell, but also the anti-reflection film of the cell, which can reduce the reflection loss of light and improve the conversion efficiency. The role of TCMs should have the following points: (i) excellent light transmission performance, so that as many photons as possible into the emitter and base region; (ii) control the refractive index to play the role of anti-reflection; (iii) in terms of electricity, achieve the highest possible conductivity.[143,144] TCMs are mostly transparent conductive oxides (TCO), and transparent electrodes in optoelectronic devices are often based on indium tin oxide (ITO), which is the most successful TCM used in both academia and industry.[145,146] However, owing to the increasing demand and price for the rare material indium (In), alternative transparent electrodes are urgently needed for the development of optoelectronic technology.[147–149] To prepare high-quality large area transparent electrodes, it is necessary to use low-cost

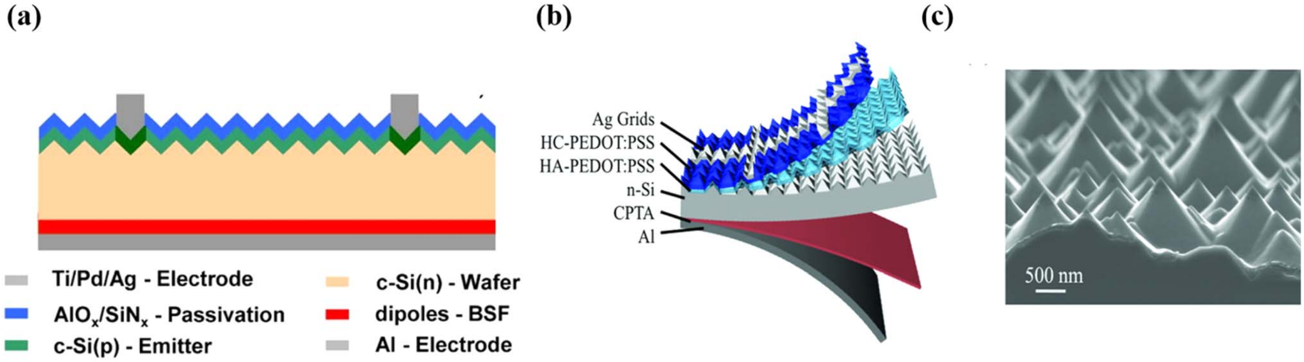

Fig. 15 (a) Schematic illustration of the organic silicon heterojunction n-type solar cells with an electron-selective contact on the back, realized by the dipole material and Al as a metal electrode (reproduced from ref. 134 with permission from American Institute of Physics, copyright 2018). (b) Configuration of a PEDOT:PSS/n-Si heterojunction device and (c) SEM image of an HA-PEDOT:PSS film on n-Si pyramids (reproduced from ref. 133 with permission from Wiley, copyright 2018).

Table 3 Compilation of c-Si solar cells employing metal compound and organic materials

Material	Carrier polarity	V_{OC} (mV)	J_{SC} (mA cm^{-2})	FF (%)	E_{ff} (%)	Ref.
SnOx	ETL	718	36.2	77.3	20.10	116
ZnOx	ETL	672	38.23	72.0	18.46	117
TiOx	ETL	696	38.61	75.3	20.24	119
LiF	ETL	716	38.36	80.5	21.12	141
MgOx	ETL	628	39.50	80.6	20.00	121
MgFx	ETL	718	41.5	74.2	22.10	124
NiOx	HTL	580	36.90	71.1	15.20	125
CuOx	HTL	622	38.38	82.6	19.71	126
WOx	HTL	715	31.50	81.1	17.90	129
V_2O_x	HTL	635	39.74	83.3	21.01	130
MoOx	HTL	718	41.50	74.2	22.10	124
PEDOT:PSS	HTL	657	38.90	80.60	20.60	136
CNT:Nafion	HTL	654	39.90	82.00	21.40	142
b-PEI	ETL	641	37.60	80.70	19.50	132
CPTA	ETL	632	34.70	76.30	16.73	133
PEO	ETL	563	28.65	76.22	12.29	131

electrodes produced by low-temperature processes and stable hydrogen (H_2) plasma. So, similar to FTO (fluorine-doped tin oxide), although it has a large optical bandgap and stable conductivity in the air environment, it is difficult to use as a transparent conductive material due to the destruction of hydrogen (H_2) plasma during the manufacturing process of solar cells and the deposition at high temperatures above 300 ° C.[150,151]

Low resistivity, high light transmittance and low temperature growth are the basic requirements for TCO films for SHJ cells.[152] The relationship between TCO film resistivity and free carrier concentration and mobility is:

$$\rho = \frac{1}{N_e q \mu} \tag{21}$$

where ρ is resistivity; q is the electronic amount of electricity; N is the free carrier concentration; μ is carrier mobility. The optical properties of TCO films are determined by the band structure and electrical properties. The optical bandgap width of TCO film should be greater than 3.1 eV, so that all wavelengths of visible light can pass through and behave as transparent. With the increase of doping, the carrier concentration increases, the optical band gap of TCO is broadened, and the optical absorption edge shifts in the short-wave direction. In the longwave region, the optical performance of TCO is affected by free carriers because free carriers interact strongly with incident light, a fundamental interaction that can be described by the classical free carrier absorption theory. An important optical property of TCO films is generally required to have an average transmittance greater than 80% in the visible range. TCO film with excellent light transmission performance can reach more than 90% in the visible light region, values of ρ_c are as low as $<10^{-5}$ Ω cm^2.[153] When depositing TCO films, the substrate temperature usually needs to be optimized.[154] The higher the deposition temperature, the better the ITO crystallinity, but when the resistivity decreases, the light transmittance decreases, so the figure of merit is introduced to balance electricity and optics.

$$\phi_{TC} = \frac{{T_{avg}}^{10}}{R_{TCO}} \tag{22}$$

${T_{avg}}^{10}$ is the average transmittance of the film in the specific region, and R_{TCO} is the sheet resistance of the film. Higher values indicate better film performance. While increasing the doping concentration or TCO layer thickness can reduce ρ_c and increase conductivity, but this reduces optical transparency, so, it is necessary to achieve balance between optical and electrical characteristics.[155]

High-performance TCO is introduced by optimizing physical properties such as structural geometry and mass density.[156,157] Numerical analysis shows that TCO with WF > 5 eV is more suitable for SHJ devices, *i.e.* allowing the use of thinner and lightly doped a-Si:H films.[158] Meanwhile, free carrier absorption (FCA) and hall mobility in TCO have great influence on light transmission. In addition, the high Hall mobility in TCO films means the large wavelength transparency limit, which is characterized by the plasma wavelength λ_p, here we need to understand the plasma wavelength (λ_{pe}), the plasma wavelength (λ_{pe}) of the TCO is given by:[159]

$$\lambda_{pe} = \frac{1}{\omega_{pe}} = \sqrt{\frac{\varepsilon m^*}{nq^2}} \tag{23}$$

where ω_{pe} is the plasma frequency, ε is the permittivity, m^* is the electron effective mass, and q is the carrier charge, ε_0 is the vacuum permittivity, m_0 is the free electron rest mass. The attenuation constant of TCO films as a function of wavelength (λ) increased at around λ_{pe} because of plasma oscillation, a phenomenon known as "cut-off".[150] Meng *et al.*[159] found in their study that with the decrease of free carrier concentration, the transmittance of NIR region increased from 70% to 95%, which is conducive to improving the performance of solar cells.

Fig. 16a shows the requirements for front and rear TCO and possible candidate for TCO application on SHJ solar cells. ITO and doped ZnO can be applied to SHJ solar cells because of high transparency and good conductivity. Research on ZnO is a hot

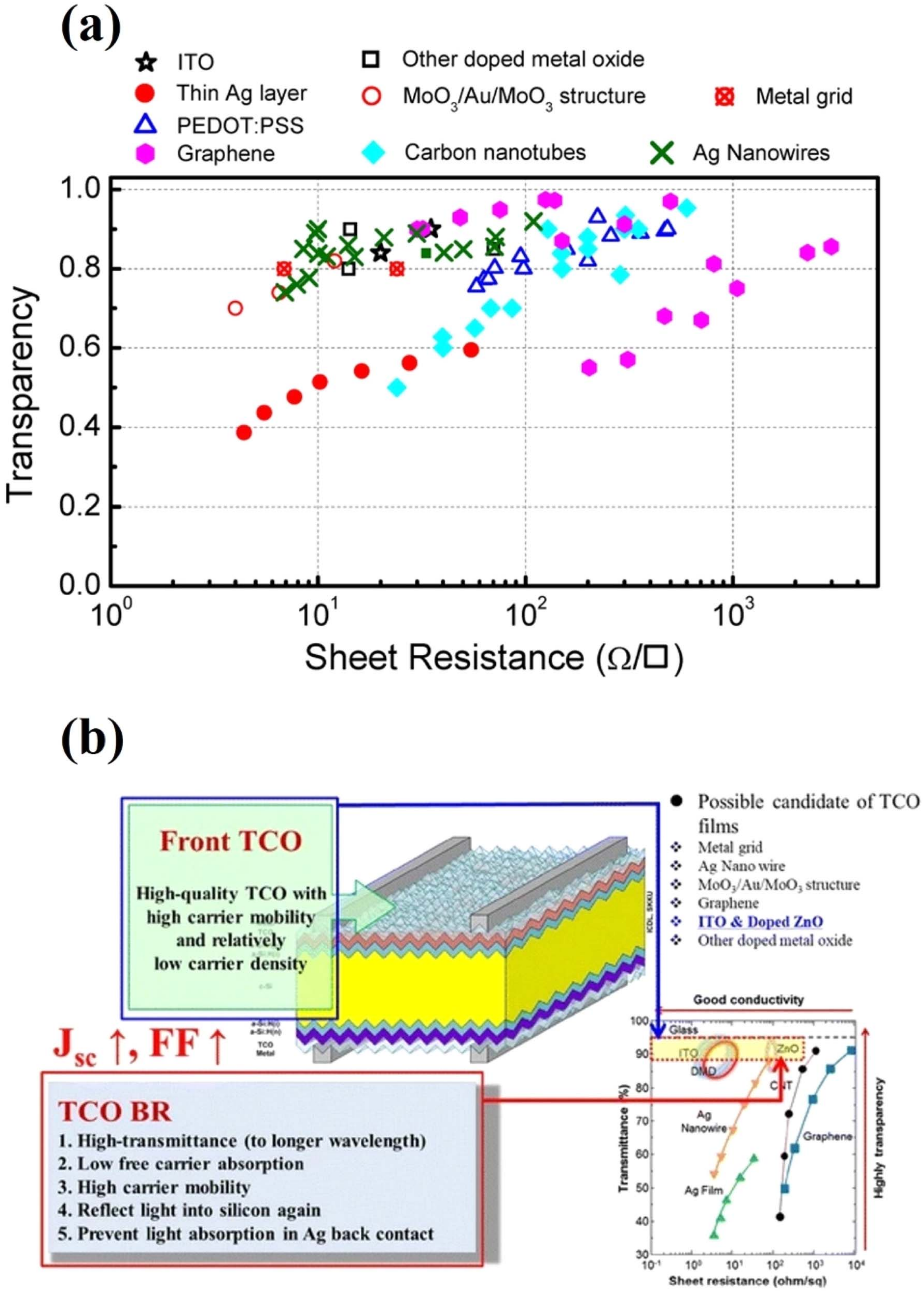

Fig. 16 (a) Requirements of TCO layer on SHJ solar cell and possible candidate of front and rear TCO layers (reproduced from ref. 160 with permission from Society of Photo-Optical Instrumentation Engineers, copyright 2014). (b) Reported different types of transparent conductive materials that have been used as transparent electrodes in SHJ solar cells, and the transparency values in the visible spectrum as a function of sheet resistance for transparent conductive materials (reproduced from ref. 161 with permission from American Institute of Physics copyright 2017).

topic, and we will introduce it accordingly below. Fig. 16b shows the results for the sheet resistance and optical transmittance of various types of transparent conductive films that were reported by other research groups.[160] The group divided TCMs into four types: doped metal oxides, inorganic metal films, non-oxide, and organic polymer electrolyte films. The sheet resistivity and transmittance of various materials are shown in the Fig. 16. Among the doped metal oxides, ITO film exhibits a maximum transmittance of 95% and a sheet resistance of 50 Ω sq^{-1}, and a sound durability;[162] furthermore, the transmittance of the thin metal layer is as low as 60%, and the electrode can guarantee a sheet resistance of approximately 80 Ω sq^{-1}.[163,164] The high transmittance values of a multi-layer structure (dielectric/metal/dielectric) and metal grids are more than 80%, whereas low sheet-resistance value of less than 80 Ω sq^{-1} is evident.[161,165] Despite its effective properties, the multi-layer structure is not very durable and is hampered by electrode-related patterning issues. Depending on the process conditions, carbon nanotubes are required to satisfy the transmittance and the sheet resistance.[166–168] The Ag nanowire exhibits a high transmittance of approximately 90% and a low sheet resistance depending on the conditions, and it can also be used as an electrode.[1,92,169–171]

High thermal elasticity and low temperature coefficient are important features of frontal contact solutions for photovoltaics. To understand the importance of thermal effects, we refer to a simple built-in junction potential model in semiconductor engineering that is suitable for idealized mutant p–n junctions. The J_{SC} of SHJ solar cells depends on the range of the built-in voltage V_{bi} between the a-Si:H(i) layer and c-Si as a charge separation and extraction mechanism, but this may be hindered by the high chip resistance of the TCO. The maximum voltage that a solar cell can provide ($V_{bi} = V_{OC}$) is affected by the rate of generation of excess electrons (Δn) or holes (Δp) in the active region where optical transparency before contact is critical,[172] we need to maintain maximum optical transmittance to achieve maximum light absorption:

$$V_{OC} = \frac{E_{FN} - E_{FP}}{e} = \frac{k_\beta T}{e} \ln\left(\frac{(n_0 + \Delta n)(p_0 + \Delta p)}{n_0 p_0}\right) \tag{24}$$

where n_0 or p_0 is the equilibrium electron or hole concentration, respectively, while the excess carrier density means that V_{OC} is comparable to the separation of quasi-Fermi levels E_{FN} and E_{FP} in the n and p regions, respectively. As the np–n_0p_0 ratio increases through the carrier injection effect, V_{OC} is larger at a given temperature.

Commonly used wide bandgap TCO materials are Sn doped In_2O_3 (ITO),[146,154] Al doped ZnO (AZO),[117,173–177] Ga doped ZnO (GZO),[178] which provide n-type conductivity. Currently, AZO and GZO are promising alternatives to ITO for thin-film transparent electrode applications, where the best candidates for AZO are inexpensive, non-toxic AZOs with low resistivity of about 10^{-4} Ω cm. The effect of actual absorber conductivity on lateral transport of high and low doping absorbers can be used to evaluate the potential of AZO as a TCO and redesigned to reduce one-dimensional losses.[174,176] However, like the problem with the commonly used TCMs, the optical transmittance of doped ZnO is generally low, especially in the NIR spectral range.[175] Besides, these metal dopants are highly diffusive: the diffusion of the dopants into the semiconducting active layer of optoelectronic devices severely deteriorates the device performance.

There are many X-doped In_2O_3 (such as W, Sn, Ce) materials used in SHJ improve performance a lot. Fluorine- and tungsten-doped In_2O_3 (IFO, and IWO) are found to be favorable for p-contact and n-contact, respectively. While for ITO, it can work well in both p-contact and n-contact, but thinner ITO shows lower contact resistance in p-contact, although its sheet resistance becomes higher. Delft University of Technology and Nankai University have designed and manufactured preferred bifacial SHJ solar cells.[179] By applying an IWO 25 nm thick on the front of the device and an ITO 25 nm thick on the back, >22% front-end efficiency was obtained. This represents a 67% reduction in TCO compared to a reference bifacial solar cell with a TCO thickness of 75 nm on both sides. In addition, utilizing the modified SHJ solar cell precursor and further TCO adjustment, our champion bifacial SHJ solar cell had a positive efficiency of 22.84%. The bifacial factor is 0.95. Indium oxide doped with transition metal: IMO, M is the abbreviation for titanium oxide (TiO_2), cerium oxide (CeO_2) and tantalum oxide (Ta_2O_5), Such IMO:H films have high carrier mobility over 70 cm^2 V^{-1} s^{-1}, high transmittance, and low free carrier absorption, which leads to a high short circuit current density exceeding 40 mA cm^{-2}. In addition, the low sheet resistance and contact resistivity of the IMO:H films contribute to the high fill factor of the solar cell. And a certified efficiency up to 25.26% (total area, 274.5 cm^2) was achieve.[180] With the development of TCO, the efficiency of silicon heterojunction solar cells continues to improve, such as IZO[181] ($E_{ff} = 24.02\%$), ICO[35] ($E_{ff} = 26.81\%$). Developing cost-effective TCO can largely solve the problem of high cost of heterojunction solar cells. Some research institutions use multi-layer TCO consisted of cost-effective TCO and dopped In_2O_3 to manufacture solar cells, which reduce the use of large amounts of In, such as AZO/IMO ($E_{ff} = 25.26\%$).[180]

Some research institutions employ sol–gel techniques to cultivate ZnO films, resulting in the successful substitution of ITO in highly efficient optoelectronic devices. As a result, the ZnO film achieves a record high conductivity of close to 500 S cm^{-1} and ultra-low optical absorption losses (<1% at wavelengths over 400 nm).[176] Tang *et al.*[182] used ITO/AZO/ITO at front and AZO at rear side in M2+ solar cells, which finally achieved a champion efficiency of 23.8% with >85% indium reduction. This research result reduces a large amount of In used in SHJ, provides a strategy for the development of SHJ in the future. In addition to the preparation of different oxide materials, the idea of oxide stacking is also important. Compared to single-layer ITO, multi-layer structure reduces the use of In, provides sufficient raw materials, and is more environmentally friendly.

SnO_x can not only be used as an electron transport layer (ETL), but also SnO-based thin films play an important role in SHJ devices as a TCO for SHJ cells. Suzhou Maxwell Technologies successfully prepared cheap and mass-producible[35] (SnOx) electrode materials by sputtering at room temperature, which is applied to the SHJ, achieving a maximum efficiency of 24.91%. Finally, SHJ solar cells with plating copper electrode and double-side IMO:H/SnO_x transparent electrodes were prepared, and a certified efficiency of 25.94% (total area of 274.4 cm^2) was achieved, and the amount of In was reduced by 50%.[36] Reactive plasma deposition is utilized by AIST to prepare a-SnO_2 thin films that are appropriate for solar cells. These films exhibit good electrical conductivity and high moisture and heat stability, while maintaining high transparency in the visible and near-infrared regions.[183] When the a-SnO_2 layer was applied to the SHJ solar cell, it was observed that the TCO layer had almost no negative impact on the performance of the SHJ, as compared to the solar cell with the indium tin oxide layer. Commonly used TCOs are summarized in Table 4.

At present, the silicon heterojunction (SHJ) cells employ indium-based transparent conductive oxide (TCO) layers to support lateral carrier transport (refer to part 6.1 for details). Nevertheless, In is a typical rare metal. For sustainable production, its consumption in solar cell manufacturing must be minimized. Researchers have developed TCO-free SHJ solar cells. For instance, Li *et al.*[189] achieved an SHJ solar cell with an efficiency of over 22% without TCO front contacts (Fig. 17a). The absence of the TCO front contact enhanced the external quantum efficiency. He *et al.*[190] realized an efficient heterojunction solar cell without conductive oxide through rational utilization of non-dopant contacts. Compared with the work of Li *et al.*, He *et al.* used non-doped TiO_x/RbF_x and MoO_x as the front and rear contact points on the n-side and p-side, respectively. MoO_x/Ag back-contact was used for hole-selective contact and RbF_x/Al front contact for electron-selective contact, and ultimately an efficiency of 22.9% was obtained, as shown in Fig. 17b. Hitoshi Sai *et al.*[191] conducted a detailed study on the influence of the TCO layer on electrical transport and stability. The research findings indicated that, regardless of the wafer polarity, the single-face rear-junction structure is beneficial for effectively collecting minority carriers without the aid of the TCO layer. The contact resistivity in the local metallized region must be minimized to achieve effective carrier transport. Correspondingly, a TCO-free SHJ cell with an efficiency of 22.1% was demonstrated in Fig. 17c.

Due to the absence of the TCO layer, compared with conventional SHJ, TCO-free solar cells still exhibit a considerable domain in terms of efficiency and stability. High-efficiency TCO-free SHJ solar cells are feasible and TCO-free SHJ technology can reduce the device cost. However, direct contact between Ag/a-Si:H may potentially lead to the penetration of Ag into the a-Si:H layer, thereby causing a device performance reduction. Overall, TCO-free SHJ technology remains in the exploration stage.

5.2 Metallization technology

The most pressing challenge currently hindering the expansion of SHJ solar cell industry is the relatively high cost of production. The low-temperature silver paste used in the SHJ process accounts for about 30% of the total processing cost due to its high consumption.[172] Therefore, many institutions are also very interested in the improvement of metal electrode materials and technologies. To improve the conductivity of electrodes and reduce the metallization cost, multi-busbar, fine-line printing, and low-temperature-cured silver-coated copper pastes have been developed.[192] In addition, several potential metallization technologies for SHJ solar cells, such as the smart wire contacting technology,[193] pattern transfer printing,[194] inkjet/FlexTrail printing,[195] and copper electroplating.[36,43,196,197]

A larger amount of low temperature silver paste for better ohmic contact is required, which will significantly affect the cost of SHJ solar cells.[198] Thus, lower silver paste consumption or substitution of expensive silver paste is of high demand for SHJ solar cell. Copper plating aroused great interest and is regarded as an ideal alternative electrode solution and industrially proven technology.[43,196,197] Benefited from the copper's high conductivity and thin finger width, the shading loss and finger resistance can be reduced remarkably, which can enhance the electrical properties. For example, SiN_X film acts as anti-reflection coating and plating mask, Ni–Si alloy as copper diffusion barrier.[196]

The resistivity of copper-plated electrode is close to bulk copper material, which is 2–3 times lower than printed silver

Table 4 Summary of the TCM applied in silicon heterojunction solar cells

No.	Material	Type	V_{OC} (mA)	J_{SC} (mA cm^{-2})	FF (%)	E_{ff} (%)	Ref.
1	ICO	n-type	751.4	41.30	86.07	26.81	35
2	IMO:H	n-type	746.2	40.10	84.64	25.26	180
4	AZO	n-type	747.5	39.13	86.23	24.94	180
5	BZO	n-type	628	41.76	67.80	17.79	184
6	IZO	n-type	743.7	38.35	84.22	24.02	181
7	IWO	n-type	731.0	40.16	78.07	22.92	185
8	AZO/IMO:H	n-type	747.4	40.10	85.48	25.26	180
9	ITO	n-type	747.0	39.60	84.90	25.20	186
10	IO:H	n-type	612	34.26	76.70	16.06	187
11	ZnO/AZO	n-type	645.3	37.11	71.60	17.13	117
12	Al_2O_3/IZO	n-type	740.0	40.53	72.33	21.57	177
13	GZO	n-type	741.5	38.79	82.56	23.65	178
14	a-SnO_x	n-type	714.0	39.30	78.90	22.18	183
15	SnO_x	n-type	747.7	39.60	84.14	24.91	36
16	SnO_x/IMO:H	n-type	747.5	40.49	85.71	25.94	36
17	SnO:Ta	n-type	748.8	39.98	83.83	25.10	188

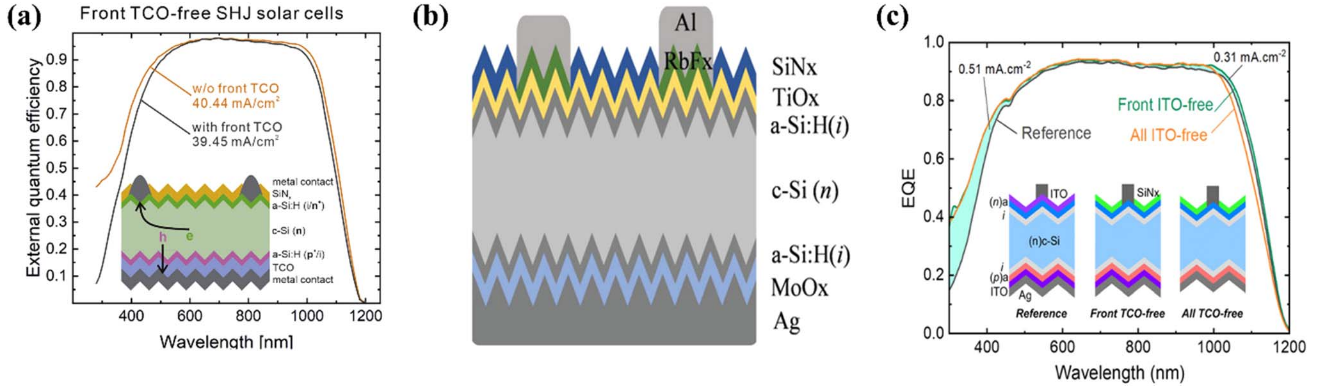

Fig. 17 (a) Sketch of SHJ solar cell structure with a rear emitter and both sides TCO-free contacts (reproduced from ref. 189 with permission from Cell Press, copyright 2021). (b) Enabling TCO-Free efficient heterojunction solar cells by flexibly using dopant-free contact (reproduced from ref. 190 with permission from Wiley, copyright 2022). (c) EQE spectra of all TCO-free, front-TCO-free, and conventional SHJ cells (reproduced from ref. 191 with permission from Wiley, copyright 2023).

electrode and could achieve decreased contact resistance and finer line. The surface morphologies comparison of printed finger and copper plated finger are shown in Fig. 18. The printed silver finger is unsmooth and wide. The topography image shows that the screen-printed Ag finger is triangular. Low temperature silver paste fulfilled with hundreds of nanometers' voids has also been observed in the cross-sectional SEM image. Taking advantage of the photolithography based, the copper finger width can be less than 30 µm. The plated copper finger is compact and uniform. Its cross section is rectangular and the surface roughness is less than 2 µm. However, the existing TCO layer makes the copper metallization totally differ from the process in diffused-emitter solar cells. The plating methods applied in diffused-emitter solar cell, such as laser ablating SiN_x film,[200] light induced plating (LIP). The current research progress in electroplating of SHJ solar cells with different methods are summarized in Table 5.

The challenges faced by the copper metallization process of SHJ solar cells are mainly the selective plating of TCO film and the adhesion of the metal oxide layer. The long-term reliability of electroplated solar cells is another decisive factor in determining whether copper metallization can be mass-

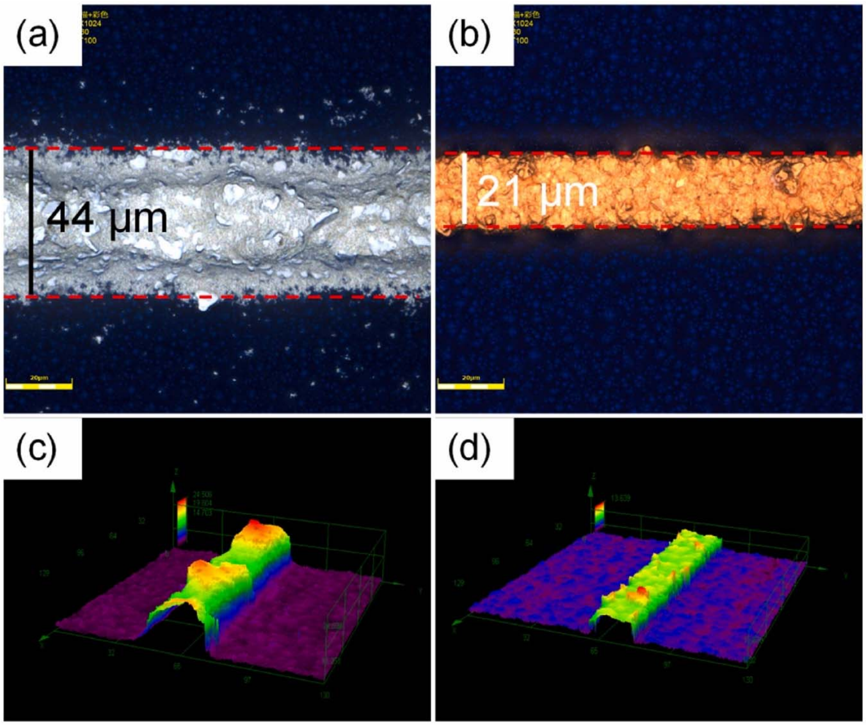

Fig. 18 SHJ solar cells: (a and c) with screen printed finger, (b and d) with electroplated finger (reproduced from ref. 199 with permission from Elsevier, copyright 2023). The electroplated one is thinner than the screen printed one, which reduced the amount of silver paste by 50%.

Table 5 Research progress in electroplating technology for SHJ solar cells

Deposition method	Finger width (μm)	E_{ff} (%)	Ref.
Low-temperature-cured	—	25.11	47
Inkjet printing		23.3	195
FlexTrail printing		23.7	195
Electrode on seed	30–40	25.10	33
Ni/Cu light induced plating	15	22.4	201
Pulse reverses current plating	30–40	20.2	202
Reverse pulse plating on Ni seed	30	22.2	203
Cu–Ni alloy palting	—	22.5	196
Electrode on PVD Ag seed	—	19.4	197
PVD copper plating	9	26.41	43
Laser transfer printing	18	26.81	35

produced.[153,155,157] For copper metallization of conventional solar cells with diffusion emitters, nickel is electro/chemically deposited. Nickel–silicon alloys are formed during subsequent annealing as a copper diffusion barrier layer In the TCO film category, ITO films with a thickness of 10–60 nm were tested as copper barriers with a maximum failure temperature of 750 ° C.[156,158,204,205] The difference in adhesion between the direct plating electrode and the TCO is one of the main challenges in simplifying the plating process, but improved adhesion of 3–5 N mm^{-1} can be achieved through the intermediate seed layer,[72,76] Copper metallization must face competition from new module technologies. The combination of fine wire screen printing and multi-busbar interconnection (or Meyer Burger's Smart Wiring Technology (SWCT)) can significantly reduce the consumption of silver paste, resulting in a consumption of silver paste as low as 100 mg.[206–208] Electroplating technology must demonstrate its cost-effectiveness advantages, otherwise breakthroughs in mass production will not be achieved. In addition to single-element metals as seed layers, co-deposited metal alloys are also deposited as electroplated seed layers. On the same ITO film, the contact resistivity of Cu–Ni alloy (0.6 mΩ cm^2) is lower than that of the evaporated copper seed crystal layer (1.18 mΩ cm^2), resulting in SHJ solar cells with a fill factor of 77.4% and conversion efficiency (22.5%).[196]

Although much effort has been currently performed in transferring the SHJ solar cell technology to high-volume manufacturing, metallization is still one of the toughest factors slowing down its industrialization progress.[198,209] Metallization not only affects the electrical performance and cost of SHJ solar cells but also affects the long-term reliability of SHJ module products.[210] More than that, due to the large particles of low-temperature silver paste, the traditional printing method of fine rasterization is very difficult, and with the continuous development of the industry makes the use of silver paste come to a new stage. Pattern transfer printing (PTP)[194] or laser transfer printing technology (LTP),[203] a contactless printing technology by Utilight, has a fine finger less than 20 μm, which can deposit the finger width smaller than that, as shown in Fig. 19.

The main advantages of LTP are as follows:(i) LTP has a smaller finger, which can reduce the cost of silver paste more than 30%, Adrian *et al.* Compared with the screen printing and LTP, the amount of silver required reduced by 54%;[211] (ii) LTP technology has excellent consistency and can keep the error within 20 μm, even can be used in the low-temperature-cured silver paste; (iii) the LTP is a contactless technology, which can avoid the problems of hidden cracks, broken pieces, contamination, scratches, *etc.* that exist in extrusion printing. Solar cells get thinner in recent years, LTP technology can effectively reduce the amount of silver paste used, and its

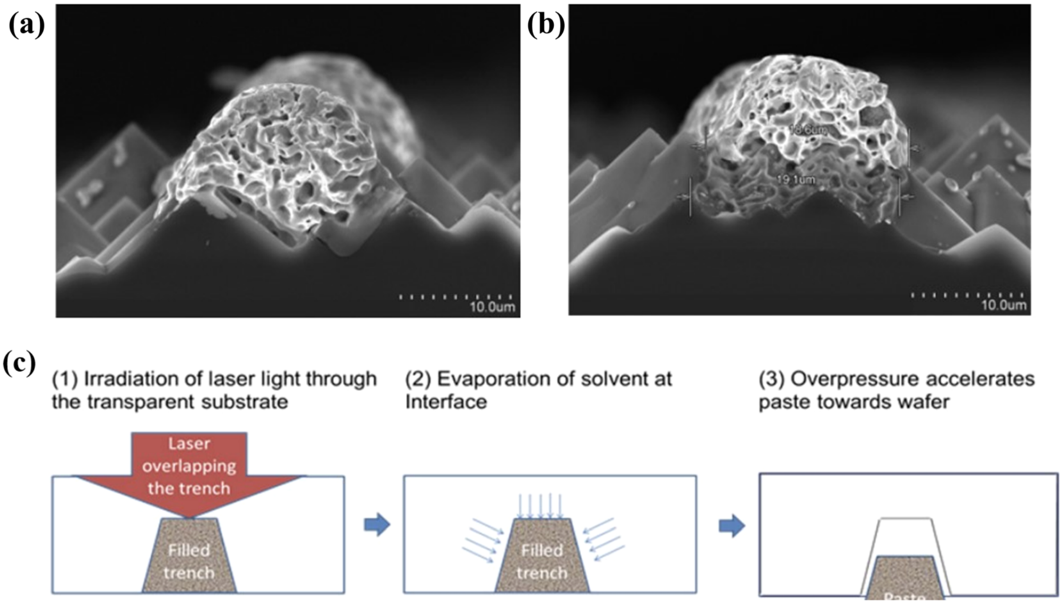

Fig. 19 (a and b) SEM images of a finger smaller than 20 μm deposited by PTP. (c) Schematic diagram of the working principle of PTP (reproduced from ref. 194 with permission from Elsevier, copyright 2015).

damage to the cell is less because the contactless printing method. In October 2023, LONGi used the laser transfer technology to make the front finger on industry-grade silicon wafers, it has improved J_{SC} dramatically, which resulted in the record efficiency 26.81%,[35] and in October 2024, silicon heterojunction back contact solar cells by laser patterning reached a champion efficiency of 27.30%.[21]

In summary, screen printing is still the mainstream solution, and further technological upgrades are needed for screen printing to achieve ultra-high utilization of Ag. The application of copper plating to silicon photovoltaics, especially in the field of silicon heterojunction, has important practical significance. However, the complex heterojunction solar cell plating process is the biggest obstacle to its industrialization. Selective deposition of seed layers and peel-free resists are key factors in simplifying the electroplating process. More innovative research is needed to break through the shortcomings of existing technologies. The development of non-destructive laser technology combined with inorganic graphics processes shows the potential for low-cost mass production of copper metallization. In the efficiency of LONGi's SHJ solar cells, traditional electrode growth methods are difficult to achieve higher efficiency, and laser transfer printing methods need to be given our attention. Although many constraints and challenges still need to be addressed, new metallization technologies should also be highlighted to disburden the current limitations of screen-printing metallization and pave the way for further efficiency increases and cost reductions in SHJ solar cells and modules.

6. Modified structure for SHJ solar cells

6.1 Rear emitter structure

As a design of standard (metal/TCO/a-Si:H(p)/a-Si:H(i)/c-Si(n)/a-Si:H(i)/a-Si:H(n)/TCO/metal) structure at soaked front is strongly dictated by the parasitic absorption in the SHJ layers, a-Si:H layer and TCO, optimization of the front layer stack is tricky as it comes at the cost of open-voltage (V_{OC}) and fill factor. Furthermore, the performance of the solar cell depends on the carrier collection of doped amorphous silicon (a-Si) layer, passivation quality of intrinsic a-Si layer, and TCO properties. Fundamental issues such as increment of the junction recombination with high doping a-Si:H layers and Schottky barrier of p-type a-Si:H with the n-type TCO's are an upper limit of V_{OC} and a trade-off between V_{OC} and FF and J_{SC} and FF, respectively. Fig. 20 shows a schematic of standard emitter and rear emitter SHJ solar cells.

High FF could be obtained with rear-emitter structures. Certainly, on n-type wafers, photo-generated electrons can benefit from the high lateral conductivity to be extracted towards the contacts.[214,215] Rear-emitter SHJ solar cells are attractive because of the lateral conductivity of electrons through the wafer yielding a higher fill factor than conventional front emitter structures.[212] However, minority carriers being collected at the rear of the cell, they are more sensitive to recombination at the front interface as there is no p–n junction induced electric field to separate charges. If the rear-emitter layer become too thin, there are no field effect passivation anymore and the interface is highly recombination. Silicon heterojunction solar cells having a rear-emitter structure feature thin silicon amorphous layers (a-Si:H) enveloping the c-Si substrate. Owing to the high-quality passivation of a-Si:H layers, SHJ solar cells can achieve easily high V_{OC}, but achieving simultaneously a high fill factor on large area cells remains challenging.[213,216] Now, Table 6 has a brief outline cell performance by comparing front emitter *versus* rear emitter regarding the transport mechanism and current flow. In conventional front emitter (FE) cells, the minority carriers of the holes are subjected to lateral transport toward the front metal grid electrode. In this configuration, the front side TCO and the absorber are horizontally p/n junction, resulting in a series connection of the absorber and the TCO.[212] At the p/n junction, holes are separated from the absorber and the actual barrier formed by the p/n junction prevents the back diffusion of the absorber.

Rear emitter (RE) devices are subjected to lateral transmission from absorber (electronic) carriers to metal grid electrodes. In this case, the front TCO and absorber are coupled horizontally through a high/low junction, connecting the TCO and absorber in parallel. This fact can be achieved within the absorber grid electrodes, with more favorable current flow patterns for carrier collection. When the device is designed with RE instead of FE, the current density inside the absorber is higher and the transverse portion of the current within the absorber is more pronounced. Therefore, in the RE design, a significant portion of the lateral current is transferred from the front-end TCO to the absorber. This results in less stringent restrictions on lateral transmission within the front-end TCO, which is why for RE designs, the influence of the thin layer resistance of the TCO electrode and the spacing of the gate electrode on the FF can be largely decoupled.[212,217]

To overcome parasitic absorption in standard a-Si:H/c-Si heterojunction solar cells, Wünsch[218] obtained an inverted a-Si:H/c-Si cell by designing a heterojunction on the back of a solar cell. The p–n junction of this cell is located on the back, and no light passes through the a-Si:H(p) emitter, so its thickness does not have to be as thin as possible, but only optimized from the perspective of minimum interface recombination speed and maximum open-circuit voltage. In addition, more conductive layers can optionally be deposited on the a-Si:H(p) emission layer to improve band bending at the a-Si:H(p)/n-c-Si interface, without necessarily being a transparent TCO film. Solar cells of this structure appear with relatively low initial efficiency, only 11.05%, but it gave people great inspiration to make SHJ cells with emitters on the back.

In Fig. 20b, it is possible to reduce power losses due to 2D transmission by placing high/low junctions at the front end and p/n junctions at the back end by placing high/low junctions on the front end and p/n junctions at the back end. The lateral conductivity of the absorbing material can open additional transmission paths. The electrical volume characteristics of optics and TCO are less pronounced, which means that requirements for spacing, TCO mobility, or free carrier density

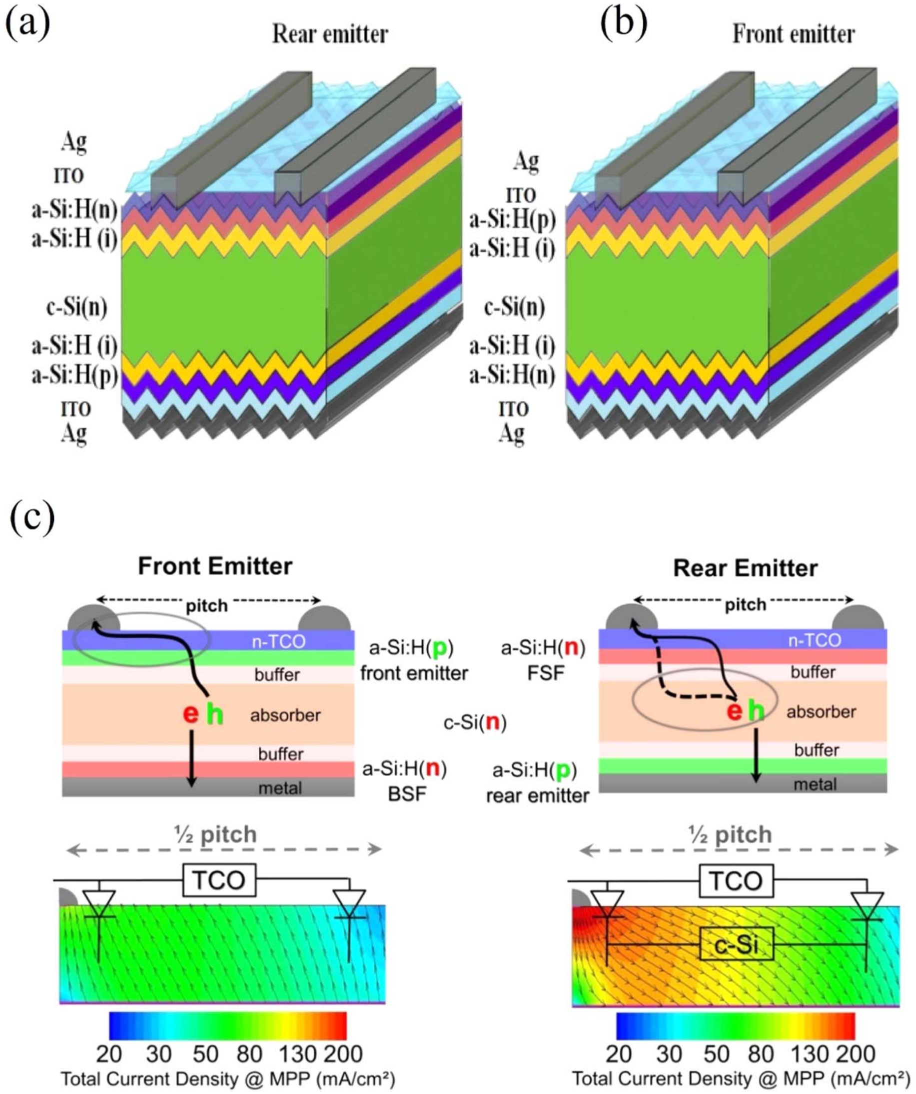

Fig. 20 Schematic diagram of the structure of the solar cell after the emission junction (a) schematic of a rear emitter structure and (b) front emitter structure (c) (Top), sketch of simulated and experimentally investigated cell structures. (Bottom) simulated current density within the absorber for MPP conditions indicating that a large part of the lateral transport is shifted from the TCO (not visible) into the absorber. The series and parallel connection between the absorber and the TCO for the FE and RE design is indicated as well (reproduced from ref. 212 and 213 with permission from Elsevier and The Korean Institute of Electrical and Electronic Material Engineers, copyright 2014 & 2020).

are lower. The reduced free carrier density allows for higher J_{SC} without affecting FF (and *vice versa*), resulting in higher efficiency. This can be interpreted as the transfer of the transverse transmission section from the TCO to the absorber. In terms of 2D effects, this distinguishes the rear emitter (RE) design from the traditional front emitter (FE) design and provides more freedom in device design. Equipped with a more complex p-type doping in the unilluminated rear, it is possible to focus on optimizing its electrical performance, while the n-type doping at the front makes the trade-off between optical and electrical performance less stringent. The results show that at the high/low junction, additional transport through the absorber facilitates lateral carrier transport and the transverse conductivity of TCO decreases. This means that under MPP conditions, the voltage drop in the TCO electrode is low, this reduces ohmic losses and non-generation losses. Although the a-Si:H/c-Si

Table 6 Comparison of front-emitter *versus* rear-emitter according to the transport mechanism and current flow

	FE	RE
Transport mechanism	2D transport loss (high/low junction, p/n)	1D transport loss
Current flow	Lateral and vertical conductivity	Lateral conductivity

heterojunction cell with the emitter on the back can theoretically reduce parasitic absorption and is conducive to the improvement of cell efficiency, there is still a certain gap between its efficiency and that of standard SHJ cells, so it needs to be continuously studied and optimization.

6.2 Interdigitated back contact structure

Apart from shadowing losses due to current collecting grids at the front side, short wavelength response losses are inevitable in front heterojunction solar cells due to parasitic absorption caused by a-Si:H films/TCO. Both issues cause reduction in J_{SC}. These two issues can be avoided by employing contacts as interdigitated pattern. In 2014, Sharp first proposed an HBC solar cell with a conversion efficiency of 25.1%.[40] Almost simultaneously, Panasonic achieved a higher conversion efficiency of 25.6%, with a design area of 143.7 cm^2, breaking the efficiency record of crystalline silicon-based solar cells at the time.[219]

In mid-September 2016, Kaneka Corporation announced a conversion efficiency of 26.3% for HBC solar cells with a designated area of 180.4 cm.[32] Soon, HBC solar cells based on n-type c-Si wafers have a size of 243 cm^2, a thickness of 200 μm, and a resistivity of about 7 Ω cm, which achieve a high conversion efficiency of 26.6%.[220] The IBC design is particularly attractive because it does not require a functional contact stack on the front of the device, which frees up design space for highly transparent materials. In general, however, IBC designs introduce greater manufacturing complexity into other simple SHJ unit processes, an issue that is currently being actively investigated.[45] In addition, the current crowding effect close to the back contacts reduces radiated recombination.[221] IBC solar cells achieve high short-circuit currents by eliminating metal grid shading on the front surface. In IBC designs, both electron and hole collection occur at the back side of the device. This allows a high degree of freedom in the optical and electronic design of the front of the solar cell, with a J_{SC} of up to 42.7 mA cm^{-2}.[172] IBC solar cells generally have higher absorption and short-circuit current densities. Other advantages are as follows: (i) since there is no front metal finger, there is no need to consider the contact resistance on the front side, which provides more space and potential for optimizing the passivation performance of the front surface; (ii) since the shading loss of the front metal finger is not considered, a wider finger can be used to reduce the series resistance of the rear metal contact; (iii) the design of all rear contacts makes the interconnection of units in the module simpler and more aesthetically pleasing.

Some research groups have used Silvaco Atlas tools for the design of emitters and BSFs for simulations and experiments. As shown in Fig. 21, with and without intrinsic a-Si:H passivation layers for doped emitters and BSFs. It was found that in order to avoid recombination at the rear, the BSF size should be less than half of the emitter size of the distance between the same polarity, *i.e.* emitter to emitter or BSF to BSF, called pitch size is also an important factor in high efficiency.[222]

The key problem for IBC solar cells is how to prepare *n*-regions and *p*-regions with good quality and sympathetic distribution on the posterior surface. In recent years, ion implantation technology has been applied to IBC solar cells because the technology can precisely control the doping concentration to obtain uniform *p*-region and *n*-region with controllable junction depth. However, the introduction and activation of dopants requires a high annealing temperature, which is a difficult problem in the photovoltaic industry.[219,223] Compared with conventional crystalline silicon cells, surface recombination of the front surface has a greater impact on the performance of IBC solar cells because the front surface is far away from the p–n junction located on the back side. In order to inhibit front surface recombination, a better surface passivation scheme is required for the front surface. At the same time, high-quality substrate materials with long diffusion lengths are often required to ensure that the minority of carriers produced by photons do not recombine before reaching the posterior junction. At the rear side, the grid lines are separated by 10 μm

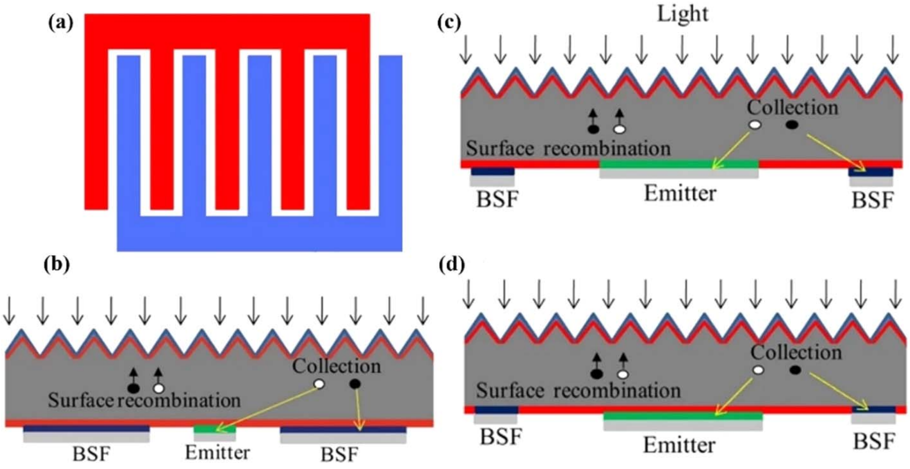

Fig. 21 (a) An interdigitated electrode pattern (current collecting girls) at the rear side of the c-Si wafer (b) probability of minority carrier recombination is enhanced when emitter size is a smaller than BSF size (figure not to scale) (c) emitter in direct contact with c-Si (d) BSF in direct contact with c-Si (peproduced from ref. 222 with permission from Springer, copyright 2017).

and the area within the electrodes are filled by contact metal in the rear side layout.

7. SHJ-based tandem solar cells

To break through the Shockley–Queisser limit of single-junction solar cells and obtain more efficient photovoltaic devices, tandem solar cells (TSC) have attracted widespread attention.[224] In multi-junction or tandem solar cells, the top cell has a wider band gap that can absorb high-energy photons. Tandem solar cells based on silicon heterojunction bottom cells, such as perovskite PVK/Si and III–V/Si tandem solar cells, are growing fast. As early as 1985, Yablonovitch *et al.* pointed out that an ideal solar cell should have a double heterojunction structure; that is, an absorber material with a smaller bandgap is placed between two materials with a broad bandgap with different doping types. The structure is easy to obtain with large quasi-Fermi level splitting in the absorbing layer material. High voltage and efficiency can be obtained if the heterojunction interface can be well-passivated. SHJ solar cells have the advantages of a simple and symmetrical structure and a low process temperature.[225] In addition, SHJ solar cells have a unique energy band structure and full-area passivation. In TSCs, SHJ cells have some natural advantages as bottom cells, the SHJ structure contains TCO material as a natural tunnel junction, which also makes the SHJ more suitable as a bottom cell. However, it is a challenge to grow high-quality perovskite films on a fluted heterojunction bottom cell.[226]

As for the PVK/Si tandem cells, there are two mainstream designs of PVK/Si tandem solar cells: two terminal (2T) and four terminal (4T) structures.[227] 2T device may offer some efficiency advantages over the parasitic absorption losses of the two ultra-transparent electrodes of a 4T structure. However, the fabrication of 2T devices poses more technical challenges in terms of materials and device structure. Perovskite solar cells as top sub-cells are particularly suitable for forming 2T TSCs with c-Si bottom sub-cell to absorb a larger solar spectral range because their band gap is adjustable.[228] For example, the high-temperature annealing process required for selective contact of certain inorganic carriers can be detrimental to the passivation and contact quality of the bottom subcell.

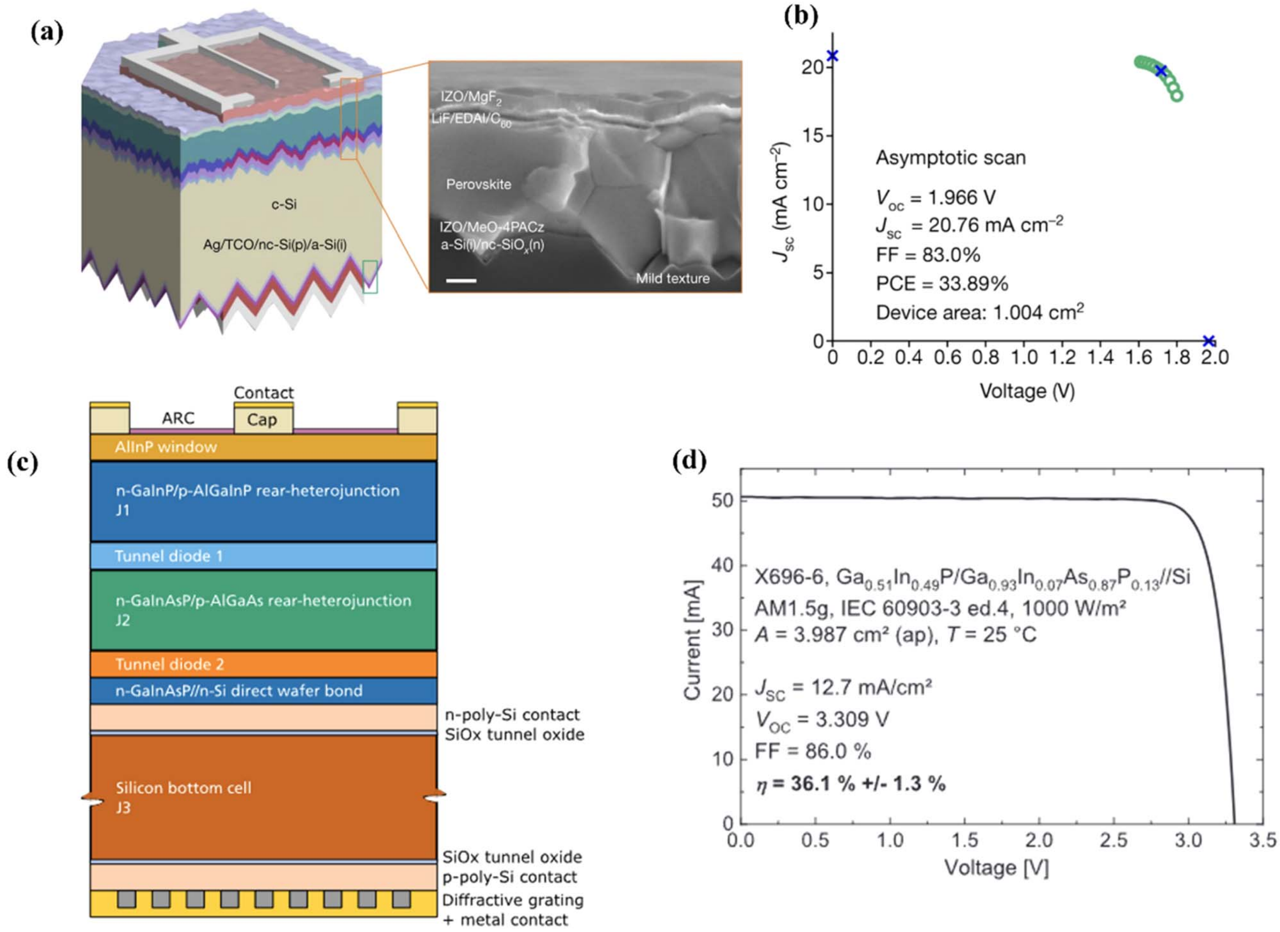

Fig. 22 (a) Schematic of the monolithic perovskite/silicon tandem solar cell built from a double-side-textured SHJ cell and (b) J–V curve and the maximum power output point of one PVK/SHJ tandem cell, measured by NREL using the asymptotic maximum power scan method (reproduced from ref. 234 with permission from Springer Nature, copyright 2024). (c) Schematic structure of the III–V//SHJ triple-junction solar cell with 36.1% efficiency and (d) J–V curve of III–V//SHJ solar cell (reproduced from ref. 233 with permission from Wiley, copyright 2024).

Compared with perovskite materials, III–V compound semiconductor materials, with their excellent proven reliability and adjustable band gap, exhibit high efficiency and promising potential for industrial application.[229] Epitaxial growth method is an advanced technology to obtain high quality multilayer films, but it has strict requirements on substrate and thin film growth. These characteristics make III–V solar cells expensive and limit the application of III–V//SHJ tandem solar cells.[230] The current maximum efficiency of PVK/SHJ tandem solar cells is 34.6%,[231,232] and the maximum efficiency of III–V//Si is 36.1%.[233] Typical PVK/SHJ and III-V//Si tandem solar cell devices are shown in Fig. 22.[233,234] Generally, tandem solar cells based on silicon heterojunction bottom cells, such as PVK/Si and III–V/Si tandem solar cells, are under development. Relative review of Si based tandem solar cells can be referenced in recent articles.[235–238]

8. Industrialization of SHJ solar cells

SHJ solar cells consist of only five steps in industrial production compared to other types of solar cells. Fewer steps, low temperature, and less energy consumption are the advantages of SHJ solar cells.[14] As shown in Fig. 23, the manufacturing process of typical SHJ solar cells begins with wafer cleaning and alkaline texturing, followed by PECVD to form a single-sided intrinsic and doped a-Si:H stack and then opposite polarity on the other side. Next, the front and back of the cell are covered by PVD by applying a TCO layer, and then metal electrodes are formed by PVD, screen printing or electroplating, fabrication process steps of double-side contacted SHJ solar cell, as well as the schematic diagrams of IBC-SHJ and bifacial SHJ solar cells have shown in Fig. 23.

Since 1997, when Sanyo introduced the SHJ industrial line, the SHJ industrial line has been continuously updated. Considering the high bifacial coefficient (>90%), low temperature coefficient and high energy yield, SHJ has the potential to achieve ultra-low power costs, and thinner wafers can reduce costs. Many of the technical aspects we discuss here are as follows:

(i) Passivation uniformity problem: a major difficulty is to achieve a uniform ultra-thin passivation layer based on a-Si:H in PECVD. In fact, these problems can be solved, for example by carrying out PECVD reactor design.[41,239] (ii) Wafer selection issues: current SHJ use more expensive n-type wafers that are less sensitive to gap transition metal defects present in the feedstock, reducing refining costs. While p-type silicon currently accounts for the majority of the market, most monocrystalline silicon manufacturers have developed proprietary technologies that enable them to grow high-quality n-type silicon (lifetime/resistivity typically greater than 1 ms Ω^{-1} cm^{-1}) at a similar or only slightly higher cost to p-type materials.[240,241] (iii) TCO cost problem: usually 100 nm ITO is deposited in the front and back of SHJ. ITO targets are a major cost factor, using about 3.5 g of indium per square meter (considering the 50% sputtering material usage). For TCO replacement, new materials such as ZnO and SnO_2 can be selected, especially on the n-side, where wafer conductivity plays a major role. (iv) The problem of high metallization cost: since the final annealing step is around 200 °C, a low curing temperature silver paste is used.[193,198] Due to the use of a multiwire configuration, in which the strip is replaced by a round wire, the need for seeker conductance is further reduced: typical 18 wires $\sim$ 300 μm, embedded in a polymer foil, soldered to soft silver paste during lamination. Due to the short distance between the two wires, it is possible to reduce silver consumption to 10–20 mg on each side of 6 inches. To completely curb the demand for silver, copper plating was also reported as an alternative, and the process of directly achieving double-sided

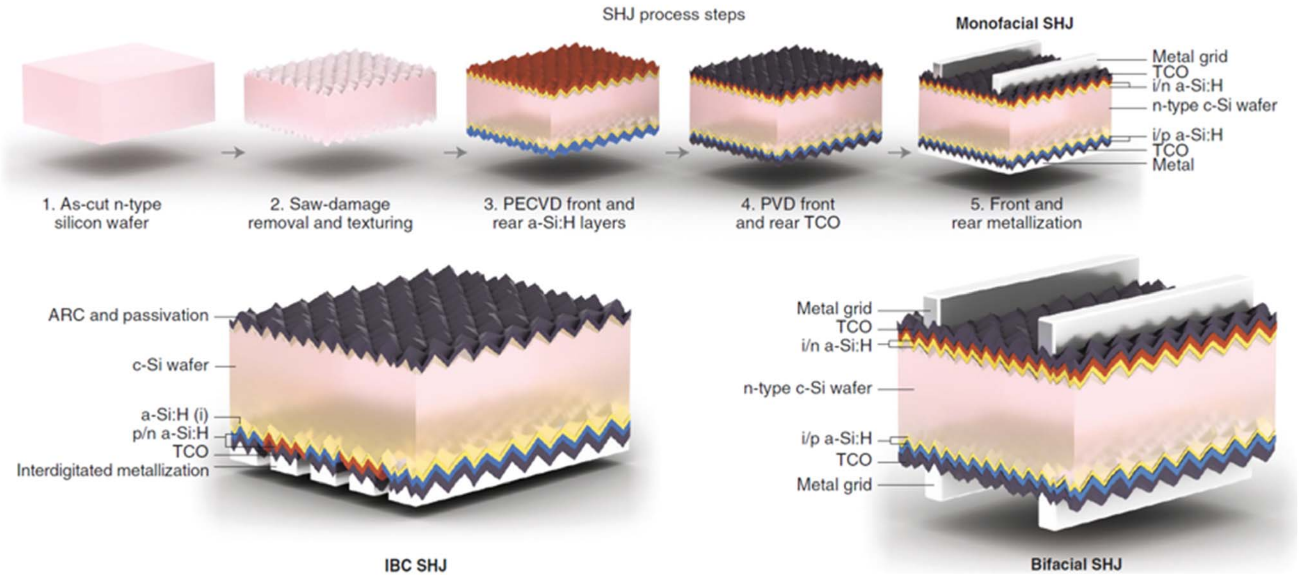

Fig. 23 Fabrication process steps of double-side contacted SHJ solar cell, as well as the schematic diagrams of IBC (interdigitated back contact) SHJ and bifacial SHJ solar cells (reproduced from ref. 14 with permission from Springer Nature, copyright 2019).

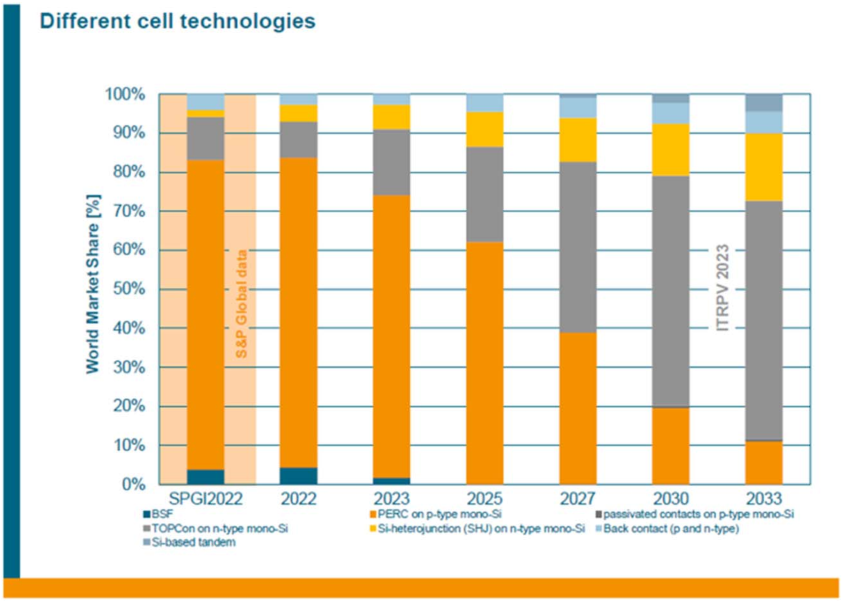

Fig. 24 Global market share for different solar cell technologies.[246]

copper metallization was also shown above.[242] The process has low-cost potential after large-scale acceptance. In addition, optimizing grid configurations using industry-compatible contact-free laser transfer printing (LTP) technology can improve solar cell efficiency, which can have a huge impact on reducing manufacturing costs.[203]

The main reasons for the decrease in SHJ solar cell cost are (i) high module efficiency (>24%), (ii) better temperature coefficient (∼0.21%/°C) indicating less performance loss over their cycles, and (iii) lower manufacturing temperatures. For every approximately 1% increase in module efficiency, the system cost balance is reduced by about 6–7%.[243] With a better temperature coefficient, SHJ cells can get higher solar energy during the day and throughout the year, which makes the technology particularly attractive for hot climate markets. Due to its higher conversion efficiency and good rear contact IR reflection characteristics, this will also significantly reduce device heating compared to the diffusion junction method. In addition, frameless designs are being explored to further improve the cost-effectiveness of SHJ cells. For standard solar glass, the phenomenon of unnecessary light loss is reflected by a refractive index mismatch at the glass/air interface, about 4%. Some measures need to be taken to improve the utilization of light. For instance, it is found that the industrial sol gel process is used to apply the porous SiO_2 layer to the glass, thus increasing the J_{SC} by about 2.7%.[244]

In industrial production, for standard industrial production lines, reducing wafer thickness is feasible to enable low-cost solar cells, and flexibility is a decisive advantage in applying silicon solar cells to life, such as power supplies for wearable devices and building-integrated photovoltaics (BIPV). Using 50 μm thick silicon wafers can save more than 70% of silicon material costs. However, the efficiency is limited due to insufficient light absorption on ultra-thin silicon substrates, especially in the long-wave region. Nanostructures are an effective method of light harvesting. For example, a 10 μm-thick inverted nanopyramid silicon achieves effective solar cell light absorption.[245]

PV industries are shifting from aluminum back surface field (Al-BSF) c-Si to passivated emitter and rear cell (PERC) and SHJ to increase efficiency further. Fig. 24 presents the projected world market share for different silicon-based PV technologies. According to the ITRPV (2023),[246] at present, PERC still holds over 70% of the c-Si market share, it is noted that the traditional Al-BSF is predicted to be outdated in 2025, while PERC, SHJ, IBC, and Si-tandem solar cells will be increased in the future, and TOPcon is expected to become the dominating solar cells after 2025.[247] Like PERC, TOPCon and HJT (SHJ) are expected to become mainstream PV technologies in the next two to three years, as these technologies offer significant advantages in terms of cost control, raw material availability, ease of process and high efficiency. The primary advantage of TOPcon solar cells, as compared to SHJ solar cells, is their compatibility with current PERC production lines. TOPCon cells are based on the PERC process, with the addition of a tunneling oxide layer and a polycrystalline silicon layer, which makes upgrading the production line easier. SHJ, on the other hand, is one of the newest crystalline silicon PV technologies, and large-scale production requires updates for new equipments. Therefore, solving the production cost problem of SHJ is crucial for making it commercially available.

9. Summary and outlook

This review provides a comprehensive overview of all aspects of SHJ solar cells, from basic theory to intrinsic passivation layer and other material selection, as well as related series of devices. SHJ solar cells are currently at the forefront of silicon solar cell research in terms of conversion efficiency. Through the introduction of passivation and stack processing in the contact layer elements, enhancements are made to carrier selectivity, passivation quality, transparency, and conductivity. It is expected to increase the efficiency limit of single-junction silicon. Due to the successful development of the passivated contact layer, the efficiency of SHJ solar cells has exceeded 27%, showing the great potential and development space of silicon heterojunction technology. Then through further improvement of TCO materials and the design of corresponding emerging thin film structures, the limit efficiency of single-junction silicon cells can be further approached.

While diffusion homojunction silicon solar cells such as Al-BSF and PERC currently dominate the PV market, SHJ solar cells will become the next generation of high-efficiency PV products. Despite of the notable achievements, the large-scale commercialization of SHJ technology remains very challenging. The SHJ solar cell industry line does not match the existing conventional production line, the main obstacle to commercialization is the big capital required to build the production line and reduce the cost of the main thin-film fabrication tools (like PECVD and PVD). Manufacturers should accelerate technological transformation (like IBC-SHJ soar cells) to realize larger scale industrialization. With the manufacture of high-efficiency devices, the use of indium and silver should be reduced (or even completely avoided). Low-cost metalized materials (like Al and Cu pastes and Al grids) should be developed to further reduce costs. Hope that there will be no material resource limitations for TW scale production for SHJ solar cells. More efficient SHJ-based tandem solar cells (like PVK/SHJ and III–V//SHJ) are the future development direction. We believe that this review will help to understand the remaining challenges and possible research directions, and promote faster development of the field.

Data availability

Data availability is not applicable to this article as no new data were created or analyzed in this study.

Conflicts of interest

There are no conflicts to declare.

Acknowledgements

This work is supported by the National Key Research and Development Program of China (No. 2022YFB4200102), and Tianjin Natural Science Foundation Project (No. 21JCYBJC00270).

References

1 W. Duan, A. Lambertz, K. Bittkau, D. Qiu, K. Qiu, U. Rau and K. Ding, *Prog. Photovoltaics Res. Appl.*, 2021, **30**, 384–392.

2 D. Moore, S. Krishnamurthy, Y. Chao, Q. Wang, D. Brabazon and P. J. McNally, *Phys. Status Solidi A*, 2011, **208**, 604–607.

3 P. H. A. Veríssimo, R. A. Campos, M. V. Guarnieri, J. P. A. Veríssimo, L. R. do Nascimento and R. Rüther, *Sol. Energy*, 2020, **211**, 433–445.

4 Y. Liu, Y. Li, Y. Wu, G. Yang, L. Mazzarella, P. Procel-Moya, A. C. Tamboli, K. Weber, M. Boccard, O. Isabella, X. Yang and B. Sun, *Mater. Sci. Eng., R*, 2020, **142**, 100579.

5 F. M. Orr, *ACS Energy Lett.*, 2016, **1**, 113–114.

6 J. Haschke, O. Dupre, M. Boccard and C. Ballif, *Sol. Energy Mater. Sol. Cells*, 2018, **187**, 140–153.

7 J. Veirman, R. Varache, M. Albaric, A. Danel, B. Guo, N. Fu and Y. C. Wang, *Sol. Energy Mater. Sol. Cells*, 2021, **228**, 11.

8 A. Haeri, *J. Mater. Sci.: Mater. Electron.*, 2017, **28**, 18183–18192.

9 A. Richter, M. Hermle and S. W. Glunz, *IEEE J. Photovoltaics*, 2013, **3**, 1184–1191.

10 J. Ziegler, A. Montesdeoca-Santana, D. Platt, S. Hohage, R. Guerrero-Lemus and D. Borchert, *Jpn. J. Appl. Phys.*, 2012, **51**, 4.

11 W. Long, S. Yin, F. Peng, M. Yang, L. Fang, X. Ru, M. Qu, H. Lin and X. Xu, *Sol. Energy Mater. Sol. Cells*, 2021, **231**, 111291.

12 J. Schmidt, R. Peibst and R. Brendel, *Sol. Energy Mater. Sol. Cells*, 2018, **187**, 39–54.

13 Y. C. Zhang, M. Kim, W. Li, P. Verlinden and B. Hallam, *Energy Environ. Sci.*, 2021, **14**, 5587–5610.

14 T. G. Allen, J. Bullock, X. Yang, A. Javey and S. De Wolf, *Nat. Energy*, 2019, **4**, 914–928.

15 Y. R. Lin, M. M. Feng, Z. X. Wang, Y. H. Zeng, M. D. Liao, L. F. Gong, B. J. Yan, Z. Z. Yuan and J. C. Ye, *Sol. Energy*, 2020, **211**, 753–758.

16 Y. Yu, S. Li, F. Xi, H. Lan, D. Wu, Z. Chen, W. Ma and R. Deng, *Sol. Energy*, 2023, **263**, 111938.

17 P. A. Basore, *Prog. Photovoltaics Res. Appl.*, 2016, **24**, 1024–1031.

18 D. B. Needleman, J. R. Poindexter, R. C. Kurchin, I. M. Peters, G. Wilson and T. Buonassisi, *IEEE 43rd Photovoltaic Specialists Conference (PVSC)*, Portland, OR, USA, 2016, pp. 3487–3491.

19 J. Melskens, B. Van de Loo, B. Macco, L. Black, S. Smit and W. Kessels, *IEEE J. Photovoltaics*, 2018, **8**, 373–388.

20 C. Hollemann, F. Haase, S. Schäfer, J. Krügener, R. Brendel and R. Peibst, *Prog. Photovoltaics Res. Appl.*, 2019, **27**, 950–958.

21 H. Wu, F. Ye, M. Yang, F. Luo, X. Tang, Q. Tang, H. Qiu, Z. Huang, G. Wang, Z. Sun, H. Lin, J. Wei, Y. Li, X. Tian, J. Zhang, L. Xie, X. Deng, T. Yuan, M. Yu, Y. Liu, P. Li, H. Chen, S. Zhou, Q. Xu, P. Li, J. Duan, J. Chen, C. Li, S. Yin, B. Liu, C. Sun, Q. Su, Y. Wang, H. Deng, T. Xie, P. Gao, Q. Kang, Y. Zhang, H. Yan, N. Yuan, F. Peng, Y. Yuan, X. Ru, B. He, L. Chen, J. Wang, J. Lu, M. Qu, C. Xue, J. Ding, L. Fang, Z. Li and X. Xu, *Nature*, 2024, **635**, 604–609.

22 T. Fellmeth, H. Höffler, S. Mack, E. Krassowski, K. Krieg, B. Kafle and J. Greulich, *Prog. Photovoltaics Res. Appl.*, 2022, **30**, 1393–1399.

23 R. A. Sinton and A. Cuevas, *Appl. Phys. Lett.*, 1996, **69**, 2510–2512.

24 A. Kimmerle, J. Greulich and A. Wolf, *Sol. Energy Mater. Sol. Cells*, 2015, **142**, 116–122.
25 R. Brendel and R. Peibst, *IEEE J. Photovoltaics*, 2016, **6**, 1413–1420.
26 S. Guo, G. Gregory, A. M. Gabor, W. V. Schoenfeld and K. O. Davis, *Sol. Energy*, 2017, **151**, 163–172.
27 B. van Wijngaarden, J. Yang and J. Schmitz, *Sol. Energy Mater. Sol. Cells*, 2022, **246**, 111909.
28 S. Kailasam, R. A. Vijayan, D. Amirthaganesan, S. Srinath, V. Viswanathan, S. Masilamani, P. Krishnamoorthy and M. Varadharajaperumal, *IEEE J. Photovoltaics*, 2021, **11**, 613–619.
29 P. G. Le Comber and W. E. Spear, *Phys. Rev. Lett.*, 1970, **25**, 509–511.
30 J. Melskens, B. W. H. van de Loo, B. Macco, L. E. Black, S. Smit and W. M. M. Kessels, *IEEE J. Photovoltaics*, 2018, **8**, 373–388.
31 M. Taguchi, K. Kawamoto, S. Tsuge, T. Baba, H. Sakata, M. Morizane, K. Uchihashi, N. Nakamura, S. Kiyama and O. Oota, *Prog. Photovoltaics Res. Appl.*, 2000, **8**, 503–513.
32 K. Yoshikawa, W. Yoshida, T. Irie, H. Kawasaki, K. Konishi, H. Ishibashi, T. Asatani, D. Adachi, M. Kanematsu, H. Uzu and K. Yamamoto, *Sol. Energy Mater. Sol. Cells*, 2017, **173**, 37–42.
33 D. Adachi, J. L. Hernández and K. Yamamoto, *Appl. Phys. Lett.*, 2015, **107**, 0003–6951.
34 F. Haase, C. Hollemann, S. Schäfer, A. Merkle, M. Rienäcker, J. Krügener, R. Brendel and R. Peibst, *Sol. Energy Mater. Sol. Cells*, 2018, **186**, 184–193.
35 H. Lin, M. Yang, X. Ru, G. Wang, S. Yin, F. Peng, C. Hong, M. Qu, J. Lu, L. Fang, C. Han, P. Procel, O. Isabella, P. Gao, Z. Li and X. Xu, *Nat. Energy*, 2023, **8**, 789–799.
36 C. Yu, Q. Zou, Q. Wang, Y. Zhao, X. Ran, G. Dong, C.-W. Peng, V. Allen, X. Cao, J. Zhou, Y. Zhao and X. Zhang, *Nat. Energy*, 2023, **8**, 1119–1125.
37 Y. Li, X. Ru, M. Yang, Y. Zheng, S. Yin, C. Hong, F. Peng, M. Qu, C. Xue, J. Lu, L. Fang, C. Su, D. Chen, J. Xu, C. Yan, Z. Li, X. Xu and Z. Shao, *Nature*, 2024, **626**, 105–110.
38 G. Wang, Q. Su, H. Tang, H. Wu, H. Lin, C. Han, T. Wang, C. Xue, J. Lu, L. Fang, Z. Li, X. Xu and P. Gao, *Nat. Commun.*, 2024, **15**, 8931.
39 M. Taguchi, A. Yano, S. Tohoda, K. Matsuyama, Y. Nakamura, T. Nishiwaki, K. Fujita and E. Maruyama, *IEEE J. Photovoltaics*, 2014, **4**, 96–99.
40 K. Masuko, M. Shigematsu, T. Hashiguchi, D. Fujishima, M. Kai, N. Yoshimura, T. Yamaguchi, Y. Ichihashi, T. Mishima, N. Matsubara, T. Yamanishi, T. Takahama, M. Taguchi, E. Maruyama and S. Okamoto, *IEEE J. Photovoltaics*, 2014, **4**, 1433–1435.
41 L. Fang, J. Liu, S. Ju, F. Zheng, W. Dong and M. Shen, *Appl. Phys. Lett.*, 2010, **97**, 0003–6951.
42 X. Ru, M. Yang, S. Yin, Y. Wang, C. Hong, F. Peng, Y. Yuan, C. Sun, C. Xue, M. Qu, J. Wang, J. Lu, L. Fang, H. Deng, T. Xie, S. Liu, Z. Li and X. Xu, *Joule*, 2024, **8**, 1092–1104.
43 C. Yu, K. Gao, C.-W. Peng, C. He, S. Wang, W. Shi, V. Allen, J. Zhang, D. Wang, G. Tian, Y. Zhang, W. Jia, Y. Song, Y. Hu, J. Colwell, C. Xing, Q. Ma, H. Wu, L. Guo, G. Dong, H. Jiang, H. Wu, X. Wang, D. Xu, K. Li, J. Peng, W. Liu, D. Chen, A. Lennon, X. Cao, S. De Wolf, J. Zhou, X. Yang and X. Zhang, *Nat. Energy*, 2023, **8**, 1375–1385.
44 W. Liu, Y. Liu, Z. Yang, C. Xu, X. Li, S. Huang, J. Shi, J. Du, A. Han, Y. Yang, G. Xu, J. Yu, J. Ling, J. Peng, L. Yu, B. Ding, Y. Gao, K. Jiang, Z. Li, Y. Yang, Z. Li, S. Lan, H. Fu, B. Fan, Y. Fu, W. He, F. Li, X. Song, Y. Zhou, Q. Shi, G. Wang, L. Guo, J. Kang, X. Yang, D. Li, Z. Wang, J. Li, S. Thoroddsen, R. Cai, F. Wei, G. Xing, Y. Xie, X. Liu, L. Zhang, F. Meng, Z. Di and Z. Liu, *Nature*, 2023, **617**, 717–723.
45 A. Tomasi, B. Paviet-Salomon, Q. Jeangros, J. Haschke, G. Christmann, L. Barraud, A. Descoeudres, J. P. Seif, S. Nicolay, M. Despeisse, S. De Wolf and C. Ballif, *Nat. Energy*, 2017, **2**, 1–8.
46 A. Descoeudres, J. Horzel, B. Paviet-Salomon, G. Christmann, J. Geissbühler, P. Wyss, N. Badel, J. W. Schüttauf, J. J. Zhao, C. Allebé, A. Faes, S. Nicolay, C. Ballif and M. Despeiss, *Prog. Photovoltaics Res. Appl.*, 2020, **28**, 569–577.
47 X. Ru, M. Qu, J. Wang, T. Ruan, M. Yang, F. Peng, W. Long, K. Zheng, H. Yan and X. Xu, *Sol. Energy Mater. Sol. Cells*, 2020, **215**, 110643.
48 M. Köhler, M. Pomaska, P. Procel, R. Santbergen, A. Zamchiy, B. Macco, A. Lambertz, W. Duan, P. Cao, B. Klingebiel, S. Li, A. Eberst, M. Luysberg, K. Qiu, O. Isabella, F. Finger, T. Kirchartz, U. Rau and K. Ding, *Nat. Energy*, 2021, **6**, 529–537.
49 L. Zhang, W. Guo, W. Liu, J. Bao, J. Liu, J. Shi, F. Meng and Z. Liu, *J. Phys. D: Appl. Phys.*, 2016, **49**, 165305.
50 I. Martín, A. Alcañiz, A. Jiménez, G. López, C. d. Cañizo and A. Datas, *IEEE J. Photovoltaics*, 2020, **10**, 1068–1075.
51 X. F. Lin, A. Fucsko, K. Noehring, E. Gabriel, A. Regner, S. York and D. Palsulich, *J. Vac. Sci. Technol. B*, 2022, **40**, 8.
52 D. Qiu, W. Duan, A. Lambertz, A. Eberst, K. Bittkau, U. Rau and K. Ding, *Sol. RRL*, 2022, **6**, 2400052.
53 J. Zhou, Q. Huang, Y. Ding, G. Hou and Y. Zhao, *Nano Energy*, 2022, **92**, 106712.
54 D. Yan, A. Cuevas, J. Stuckelberger, E. C. Wang, S. P. Phang, T. C. Kho, J. I. Michel, D. Macdonald and J. Bullock, *Prog. Photovoltaics Res. Appl.*, 2022, **31**, 310–326.
55 S. Furukawa and T. Miyasato, *Phys. Rev. B:Condens. Matter Mater. Phys.*, 1988, **38**, 5726–5729.
56 M. Garín, U. Rau, W. Brendle, I. Martín and R. Alcubilla, *J. Appl. Phys.*, 2005, **98**, 0021–8979.
57 D. Macdonald, R. A. Sinton and A. Cuevas, *J. Appl. Phys.*, 2001, **89**, 2772–2778.
58 G. Seguini, E. Cianci, C. Wiemer, D. Saynova, J. A. M. van Roosmalen and M. Perego, *Appl. Phys. Lett.*, 2013, **102**, 1077–3118.
59 S. W. Glunz and F. Feldmann, *Sol. Energy Mater. Sol. Cells*, 2018, **185**, 260–269.
60 H. Sai, H.-J. Hsu, P.-W. Chen, P.-L. Chen and T. Matsui, *Phys. Status Solidi A*, 2021, **218**, 2000743.
61 H. Fujiwara and M. Kondo, *Appl. Phys. Lett.*, 2007, **90**, 1079–7114.

62 T. H. Wang, E. Iwaniczko, M. R. Page, D. H. Levi, Y. Yan, H. M. Branz and Q. Wang, *Thin Solid Films*, 2006, **501**, 284–287.

63 T. Ruan, M. Qu, J. Wang, Y. He, X. Xu, C. Yu, Y. Zhang and H. Yan, *J. Mater. Sci.: Mater. Electron.*, 2019, **30**, 13330–13335.

64 J. Panigrahi and V. K. Komarala, *J. Non-Cryst. Solids*, 2021, **574**, 0022–3093.

65 Y. Zhang, C. Yu, M. Yang, L.-R. Zhang, Y.-C. He, J.-Y. Zhang, X.-X. Xu, Y.-Z. Zhang, X.-M. Song and H. Yan, *Chin. Phys. Lett.*, 2017, **34**, 0256–307X.

66 D. K. Schroder and D. L. Meier, *IEEE Trans. Electron Devices*, 1984, **31**, 637–647.

67 S. De Wolf and M. Kondo, *Appl. Phys. Lett.*, 2007, **90**, 0003–6951.

68 W. Liu, L. Zhang, R. Chen, F. Meng, W. Guo, J. Bao and Z. Liu, *J. Appl. Phys.*, 2016, **120**, 175301.

69 C. Luderer, D. Kurt, A. Moldovan, M. Hermle and M. Bivour, *Sol. Energy Mater. Sol. Cells*, 2022, **238**, 111412.

70 A. Cruz, E.-C. Wang, A. B. Morales-Vilches, D. Meza, S. Neubert, B. Szyszka, R. Schlatmann and B. Stannowski, *Sol. Energy Mater. Sol. Cells*, 2019, **195**, 339–345.

71 R. Peibst, U. Römer, Y. Larionova, M. Rienäcker, A. Merkle, N. Folchert, S. Reiter, M. Turcu, B. Min, J. Krügener, D. Tetzlaff, E. Bugiel, T. Wietler and R. Brendel, *Sol. Energy Mater. Sol. Cells*, 2016, **158**, 60–67.

72 T. F. Wietler, D. Tetzlaff, J. Krügener, M. Rienäcker, F. Haase, Y. Larionova, R. Brendel and R. Peibst, *Appl. Phys. Lett.*, 2017, **110**, 0003–6951.

73 N. Folchert, M. Rienäcker, A. A. Yeo, B. Min, R. Peibst and R. Brendel, *Sol. Energy Mater. Sol. Cells*, 2018, **185**, 425–430.

74 P. Procel, G. Yang, O. Isabella and M. Zeman, *IEEE J. Photovoltaics*, 2019, **9**, 374–384.

75 P. Procel, P. Löper, F. Crupi, C. Ballif and A. Ingenito, *Sol. Energy Mater. Sol. Cells*, 2019, **200**, 109937.

76 H. Steinkemper, F. Feldmann, M. Bivour and M. Hermle, *IEEE J. Photovoltaics*, 2015, **5**, 1348–1356.

77 S. Choi, K. H. Min, M. S. Jeong, J. I. Lee, M. G. Kang, H. E. Song, Y. Kang, H. S. Lee, D. Kim and K. H. Kim, *Sci. Rep.*, 2017, **7**, 12853.

78 A. Campa, F. Smole, N. Folchert, T. Wietler, B. Min, R. Brendel and M. Topic, *IEEE J. Photovoltaics*, 2019, **9**, 1575–1582.

79 A. S. Kale, W. Nemeth, H. Guthrey, E. Kennedy, A. G. Norman, M. Page, M. Al-Jassim, D. L. Young, S. Agarwal and P. Stradins, *Appl. Phys. Lett.*, 2019, **114**, 0003–6951.

80 O. Gabriel, S. Kirner, M. Klingsporn, F. Friedrich, B. Stannowski and R. Schlatmann, *Plasma Processes Polym.*, 2015, **12**, 82–91.

81 Y.-H. Chu, C.-C. Lee, T.-H. Chang, Y.-L. Hsieh, S.-M. Liu, J.-Y. Chang, T. T. Li and I. C. Chen, *J. Non-Cryst. Solids*, 2015, **412**, 5–10.

82 T. Oikawa, K. Ohdaira, K. Higashimine and H. Matsumura, *Curr. Appl. Phys.*, 2015, **15**, 1168–1172.

83 M. A. Green, *Nat. Energy*, 2023, **8**, 783–784.

84 Z. C. Holman, A. Descoeudres, L. Barraud, F. Z. Fernandez, J. P. Seif, S. De Wolf and C. Ballif, *IEEE J. Photovoltaics*, 2012, **2**, 7–15.

85 L. Mazzarella, S. Kirner, B. Stannowski, L. Korte, B. Rech and R. Schlatmann, *Appl. Phys. Lett.*, 2015, **106**, 0003–6951.

86 L. Mazzarella, A. B. Morales-Vilches, M. Hendrichs, S. Kirner, L. Korte, R. Schlatmann and B. Stannowski, *IEEE J. Photovoltaics*, 2018, **8**, 70–78.

87 A. Richter, V. Smirnov, A. Lambertz, K. Nomoto, K. Welter and K. Ding, *Sol. Energy Mater. Sol. Cells*, 2018, **174**, 196–201.

88 A. Lambertz, V. Smirnov, T. Merdzhanova, K. Ding, S. Haas, G. Jost, R. E. I. Schropp, F. Finger and U. Rau, *Sol. Energy Mater. Sol. Cells*, 2013, **119**, 134–143.

89 A. Richter, F. Lentz, M. Meier, F. Finger and K. Ding, *Phys. Status Solidi A*, 2016, **213**, 1976–1982.

90 L. Mazzarella, A. B. Morales-Vilches, L. Korte, R. Schlatmann and B. Stannowski, *Sol. Energy Mater. Sol. Cells*, 2018, **179**, 386–391.

91 K. Ding, U. Aeberhard, V. Smirnov, B. Holländer, F. Finger and U. Rau, *Jpn. J. Appl. Phys.*, 2013, **52**, 0021–4922.

92 L. Yang, T. Zhang, H. Zhou, S. C. Price, B. J. Wiley and W. You, *ACS Appl. Mater. Interfaces*, 2011, **3**, 4075–4084.

93 H. Fujiwara, T. Kaneko and M. Kondo, *Appl. Phys. Lett.*, 2007, **91**, 0003–6951.

94 M. Stuckelberger, R. Biron, N. Wyrsch, F. J. Haug and C. Ballif, *Renewable Sustainable Energy Rev.*, 2017, **76**, 1497–1523.

95 W. Liu, J. Shi, L. Zhang, A. Han, S. Huang, X. Li, J. Peng, Y. Yang, Y. Gao, J. Yu, K. Jiang, X. Yang, Z. Li, W. Zhao, J. Du, X. Song, J. Yin, J. Wang, Y. Yu, Q. Shi, Z. Ma, H. Zhang, J. Ling, L. Xu, J. Kang, F. Xu, J. Liu, H. Liu, Y. Xie, F. Meng, S. De Wolf, F. Laquai, Z. Di and Z. Liu, *Nat. Energy*, 2022, **7**, 427–437.

96 O. Madani Ghahfarokhi, K. von Maydell and C. Agert, *Appl. Phys. Lett.*, 2014, **104**, 0003–6951.

97 A. Shah, J. Meier, E. Vallat-Sauvain, N. Wyrsch, U. Kroll, C. Droz and U. Graf, *Sol. Energy Mater. Sol. Cells*, 2003, **78**, 469–491.

98 H. Umishio, H. Sai, T. Koida and T. Matsui, *Prog. Photovoltaics Res. Appl.*, 2020, **29**, 344–356.

99 M. Sharma, J. Panigrahi and V. K. Komarala, *Nanoscale Adv.*, 2021, **3**, 3373–3383.

100 Z. Qiao, X. Xie, Q. Hao, D. Wen, J. Xue and C. Liu, *Appl. Surf. Sci.*, 2015, **324**, 152–159.

101 D. P. Pham, D. Oh, V.-A. Dao, Y. Kim and J. Yi, *Appl. Mater. Today*, 2022, **29**, 2352–9407.

102 H. Matsumura, T. Hayakawa, T. Ohta, Y. Nakashima, M. Miyamoto, T. C. Thi, K. Koyama and K. Ohdaira, *J. Appl. Phys.*, 2014, **116**, 0021–8979.

103 Y. Liu, D. Y. Kim, A. Lambertz and K. Ding, *Thin Solid Films*, 2017, **635**, 63–65.

104 V. Smirnov, A. Lambertz, B. Grootoonk, R. Carius and F. Finger, *J. Non-Cryst. Solids*, 2012, **358**, 1954–1957.

105 V. Smirnov, W. Böttler, A. Lambertz, H. Wang, R. Carius and F. Finger, *Phys. Status Solidi C*, 2010, **7**, 1053–1056.

106 S. J. Konezny, M. N. Bussac and L. Zuppiroli, *Appl. Phys. Lett.*, 2008, **92**, 0003–6951.
107 C. Lei, C.-W. Peng, J. Zhong, H. Li, M. Yang, K. Zheng, X. Qu, L. wu, C. Yu, Y. Li and X. Xu, *Sol. Energy Mater. Sol. Cells*, 2020, **209**, 110439.
108 M. Q. Khokhar, S. Q. Hussain, S. Chowdhury, M. A. Zahid, D. P. Pham, S. Jeong, S. Kim, S. Kim, E.-C. Cho and J. Yi, *Energy Convers. Manage.*, 2022, **252**, 115033.
109 J. Zhou, B. Zhang, J. Chen, H. Ren, Q. Huang, X. Zhang, G. Hou and Y. Zhao, *Appl. Phys. A*, 2021, **127**, 0947–8396.
110 M. Boccard and Z. C. Holman, *J. Appl. Phys.*, 2015, **118**, 0021–8979.
111 C. Battaglia, S. M. de Nicolás, S. De Wolf, X. Yin, M. Zheng, C. Ballif and A. Javey, *Appl. Phys. Lett.*, 2014, **104**, 0003–6951.
112 W. Li, Z. Xu, Y. Yan, J. Zhou, Q. Huang, S. Xu, X. Zhang, Y. Zhao and G. Hou, *Adv. Energy Mater.*, 2024, **14**, 2304338.
113 J. Bullock, Y. Wan, Z. Xu, S. Essig, M. Hettick, H. Wang, W. Ji, M. Boccard, A. Cuevas, C. Ballif and A. Javey, *ACS Energy Lett.*, 2018, **3**, 508–513.
114 J. Dréon, Q. Jeangros, J. Cattin, J. Haschke, L. Antognini, C. Ballif and M. Boccard, *Nano Energy*, 2020, **70**, 104495.
115 M. Liu, Y. Zhou, G. Dong, W. Wang, J. Wang, C. Liu, F. Liu and D. Yu, *Sol. Energy Mater. Sol. Cells*, 2019, **200**, 109996.
116 Q. Wang, Y. Zhou, W. Guo, Y. Yang, J. Shang, H. Chen, H. Mao, T. Zhu, Y. Zhou and F. Liu, *Appl. Phys. Lett.*, 2021, **119**, 263502.
117 J. Ding, Y. Zhou, G. Dong, M. Liu, D. Yu and F. Liu, *Prog. Photovoltaics Res. Appl.*, 2018, **26**, 974–980.
118 J. Bullock, Y. Wan, M. Hettick, X. Zhaoran, S. P. Phang, D. Yan, H. Wang, W. Ji, C. Samundsett, Z. Hameiri, D. Macdonald, A. Cuevas and A. Javey, *Adv. Energy Mater.*, 2019, **9**, 1803367.
119 F. Li, Z. Sun, Y. Zhou, Q. Wang, Q. Zhang, G. Dong, F. Liu, Z. Fan, Z. Liu, Z. Cai, Y. Zhou and D. Yu, *Sol. Energy Mater. Sol. Cells*, 2019, **203**, 110196.
120 T. G. Allen and A. Cuevas, *Appl. Phys. Lett.*, 2014, **105**, 031601.
121 Y. Wan, C. Samundsett, J. Bullock, M. Hettick, T. Allen, D. Yan, J. Peng, Y. Wu, J. Cui, A. Javey and A. Cuevas, *Adv. Energy Mater.*, 2017, **7**, 1601863.
122 B. Macco, L. E. Black, J. Melskens, B. W. H. van de Loo, W.-J. H. Berghuis, M. A. Verheijen and W. M. M. Kessels, *Sol. Energy Mater. Sol. Cells*, 2018, **184**, 98–104.
123 J. Bullock, M. Hettick, J. Geissbühler, A. J. Ong, T. Allen, C. M. Sutter-Fella, T. Chen, H. Ota, E. W. Schaler, S. De Wolf, C. Ballif, A. Cuevas and A. Javey, *Nat. Energy*, 2016, **1**, 15031.
124 W. Wu, W. Lin, S. Zhong, B. Paviet-Salomon, M. Despeisse, Q. Jeangros, Z. Liang, M. Boccard, H. Shen and C. Ballif, *Phys. Status Solidi RRL*, 2020, **14**, 1900688.
125 M. Nayak, S. Mandal, A. Pandey, S. Mudgal, S. P. Singh and V. K. Komarala, *Sol. RRL*, 2019, **3**, 1900261.
126 L. Li, G. Du, X. Zhou, Y. Lin, Y. Jiang, X. Gao, L. Lu, G. Li, W. Zhang, Q. Feng, J. Wang, L. Yang and D. Li, *ACS Appl. Mater. Interfaces*, 2021, **13**, 28415–28423.
127 C. Messmer, M. Bivour, J. Schon, S. W. Glunz and M. Hermle, *IEEE J. Photovoltaics*, 2018, **8**, 456–464.
128 M. Mews, L. Korte and B. Rech, *Sol. Energy Mater. Sol. Cells*, 2016, **158**, 77–83.
129 M. Bivour, J. Temmler, F. Zähringer, S. Glunz and M. Hermle, *IEEE 43rd Photovoltaic Specialists Conference (PVSC)*, Portland, OR, USA, 2016, pp. 0215–0220.
130 G. Du, L. Li, X. Yang, X. Zhou, Z. Su, P. Cheng, Y. Lin, L. Lu, J. Wang, L. Yang, X. Gao, X. Chen and D. Li, *Adv. Mater. Interfaces*, 2021, **8**, 2100989.
131 D. Wang, J. Sheng, S. Wu, J. Zhu, S. Chen, P. Gao and J. Ye, *Appl. Phys. Lett.*, 2016, **109**, 0003–6951.
132 X. Yang, Z. Ying, Z. Yang, J.-R. Xu, W. Wang, J. Wang, Z. Wang, L. Yao, B. Yan and J. Ye, *Adv. Sci.*, 2021, **8**, 2003245.
133 J. He, Y. Wan, P. Gao, J. Tang and J. Ye, *Adv. Funct. Mater.*, 2018, **28**, 1802192.
134 C. Reichel, U. Würfel, K. M. Winkler, H. Schleiermacher, M. Kohlstädt, M. Unmüssig, C. Messmer, M. Hermle and S. W. Glunz, *J. Appl. Phys.*, 2018, **123**, 024505.
135 J. P. Bastos, E. Voroshazi, E. Fron, G. Brammertz, T. Vangerven, M. Van der Auweraer, J. Poortmans and D. Cheyns, *ACS Appl. Mater. Interfaces*, 2016, **8**, 9798–9805.
136 D. Zielke, C. Niehaves, W. Lövenich, A. Elschner, M. Hörteis and J. Schmidt, *Energy Procedia*, 2015, **77**, 331–339.
137 N. Ikeda, T. Koganezawa, D. Kajiya and K.-i. Saitow, *J. Phys. Chem. C*, 2016, **120**, 19043–19048.
138 I. Lee, G. W. Kim, M. Yang and T. S. Kim, *ACS Appl. Mater. Interfaces*, 2016, **8**, 302–310.
139 J. Chen, L. Yang, K. Ge, B. Chen, Y. Shen, J. Guo, H. Liu, Y. Xu, J. Fan and Y. Mai, *Appl. Phys. Lett.*, 2017, **111**, 0003–6951.
140 J. Chen, K. Ge, C. Zhang, J. Guo, L. Yang, D. Song, F. Li, Z. Xu, Y. Xu and Y. Mai, *ACS Appl. Mater. Interfaces*, 2018, **10**, 44890–44896.
141 Z. Liu, H. Lin, Z. Wang, L. Chen, T. Wu, Y. Pang, L. Cai, J. He, S. Peng, H. Shen and P. Gao, *Adv. Sci.*, 2022, **9**, 2202240.
142 J. Chen, L. Wan, H. Li, J. Yan, J. Ma, B. Sun, F. Li and B. S. Flavel, *Adv. Funct. Mater.*, 2020, **30**, 2004476.
143 E. Aydin, C. Altinkaya, Y. Smirnov, M. A. Yaqin, K. P. S. Zanoni, A. Paliwal, Y. Firdaus, T. G. Allen, T. D. Anthopoulos, H. J. Bolink, M. Morales-Masis and S. De Wolf, *Matter*, 2021, **4**, 3549–3584.
144 K. Ellmer, *Nat. Photonics*, 2012, **6**, 809–817.
145 A. I. Hofmann, E. Cloutet and G. Hadziioannou, *Adv. Electron. Mater.*, 2018, **4**, 2400645.
146 T. Tang, C. Yu, C. W. Peng, G. Dong, C. He, X. Ran, H. Jiang, V. Allen, X. Cao and J. Zhou, *Prog. Photovoltaics Res. Appl.*, 2022, **31**, 449–460.
147 B. Azzopardi, C. J. M. Emmott, A. Urbina, F. C. Krebs, J. Mutale and J. Nelson, *Energy Environ. Sci.*, 2011, **4**, 1754–5692.
148 L. Gao, Z. Dai, H. Wu, C. Wu and Y. Wan, *Sep. Purif. Technol.*, 2022, **288**, 119586.
149 D.-Y. Lee, S.-P. Cho, S.-I. Na and S.-S. Kim, *J. Ind. Eng. Chem.*, 2017, **45**, 1–4.

150 I. Hamberg and C. G. Granqvist, *J. Appl. Phys.*, 1986, **60**, R123–R160.

151 L. Xu, W. Liu, H. Liu, C. Ke, M. Wang, C. Zhang, E. Aydin, M. Al-Aswad, K. Kotsovos, I. Gereige, A. Al-Saggaf, A. Jamal, X. Yang, P. Wang, F. Laquai, T. G. Allen and S. De Wolf, *Joule*, 2021, **5**, 631–645.

152 M. Morales-Masis, S. De Wolf, R. Woods-Robinson, J. W. Ager and C. Ballif, *Adv. Electron. Mater.*, 2017, **3**, 1600529.

153 A. Klein, C. Korber, A. Wachau, F. Sauberlich, Y. Gassenbauer, S. P. Harvey, D. E. Proffit and T. O. Mason, *Materials*, 2010, **3**, 4892–4914.

154 V. A. Dao, H. Choi, J. Heo, H. Park, K. Yoon, Y. Lee, Y. Kim, N. Lakshminarayan and J. Yi, *Curr. Appl. Phys.*, 2010, **10**, S506–S509.

155 C. Luderer, L. Tutsch, C. Messmer, M. Hermle and M. Bivour, *IEEE J. Photovoltaics*, 2021, **11**, 329–336.

156 M. Singh, P. Prasher and J. Kim, *Nano-Struct. Nano-Objects*, 2018, **16**, 151–155.

157 R. Saive, M. Boccard, T. Saenz, S. Yalamanchili, C. R. Bukowsky, P. Jahelka, Z. J. Yu, J. Shi, Z. Holman and H. A. Atwater, *Sustainable Energy Fuels*, 2017, **1**, 593–598.

158 M. Bivour, S. Schröer and M. Hermle, *Energy Procedia*, 2013, **38**, 658–669.

159 F. Meng, J. Shi, Z. Liu, Y. Cui, Z. Lu and Z. Feng, *Sol. Energy Mater. Sol. Cells*, 2014, **122**, 70–74.

160 W. Cao, J. Li, H. Chen and J. Xue, *J. Photonics Energy*, 2014, **4**, 040990.

161 R. Hokari, K. Kurihara, N. Takada and H. Hiroshima, *Appl. Phys. Lett.*, 2017, **111**, 0003–6951.

162 N. Kim, H.-D. Um, I. Choi, K.-H. Kim and K. Seo, *ACS Appl. Mater. Interfaces*, 2016, **8**, 11412–11417.

163 S. D. Yambem, A. Haldar, K.-S. Liao, E. P. Dillon, A. R. Barron and S. A. Curran, *Sol. Energy Mater. Sol. Cells*, 2011, **95**, 2424–2430.

164 N. Formica, P. Mantilla-Perez, D. S. Ghosh, D. Janner, T. L. Chen, M. Huang, S. Garner, J. Martorell and V. Pruneri, *ACS Appl. Mater. Interfaces*, 2015, **7**, 4541–4548.

165 W. Cao, Y. Zheng, Z. Li, E. Wrzesniewski, W. T. Hammond and J. Xue, *Org. Electron.*, 2012, **13**, 2221–2228.

166 F. Wang, D. Kozawa, Y. Miyauchi, K. Hiraoka, S. Mouri, Y. Ohno and K. Matsuda, *Nat. Commun.*, 2015, **6**, 6305.

167 D.-Y. Cho, K. Eun, S.-H. Choa and H.-K. Kim, *Carbon*, 2014, **66**, 530–538.

168 T. M. Barnes, M. O. Reese, J. D. Bergeson, B. A. Larsen, J. L. Blackburn, M. C. Beard, J. Bult and J. van de Lagemaat, *Adv. Energy Mater.*, 2012, **2**, 353–360.

169 J. Krantz, M. Richter, S. Spallek, E. Spiecker and C. J. Brabec, *Adv. Funct. Mater.*, 2011, **21**, 4784–4787.

170 D. S. Leem, A. Edwards, M. Faist, J. Nelson, D. D. Bradley and J. C. de Mello, *Adv. Mater.*, 2011, **23**, 4371–4375.

171 M. Song, J.-K. Kim, S.-Y. Yang and J.-W. Kang, *Thin Solid Films*, 2014, **573**, 14–17.

172 C. Battaglia, A. Cuevas and S. De Wolf, *Energy Environ. Sci.*, 2016, **9**, 1552–1576.

173 O. Madani Ghahfarokhi, K. Chakanga, S. Geissendoerfer, O. Sergeev, K. von Maydell and C. Agert, *Prog. Photovoltaics Res. Appl.*, 2015, **23**, 1340–1352.

174 K. N. Tonny, R. Rafique, A. Sharmin, M. S. Bashar and Z. H. Mahmood, *AIP Adv.*, 2018, **8**, 2158–3226.

175 G. V. Naik, J. Liu, A. V. Kildishev, V. M. Shalaev and A. Boltasseva, *Proc. Natl. Acad. Sci. U. S. A.*, 2012, **109**, 8834–8838.

176 Z. Chen, J. Wang, H. Wu, J. Yang, Y. Wang, J. Zhang, Q. Bao, M. Wang, Z. Ma, W. Tress and Z. Tang, *Nat. Commun.*, 2022, **13**, 4387.

177 M. A. Zahid, M. Q. Khokhar, S. Park, S. Q. Hussain, Y. Kim and J. Yi, *Vacuum*, 2022, **200**, 0042–207X.

178 Z. Yan, J. Shi, S. Chen, J. Du, L. Zhang, Q. Yuan, C. Song, K. Jiang, Y. Yang, A. Han, Z. Liu and F. Meng, *Sol. Energy Mater. Sol. Cells*, 2023, **253**, 112244.

179 C. Han, R. Santbergen, M. van Duffelen, P. Procel, Y. Zhao, G. Yang, X. Zhang, M. Zeman, L. Mazzarella and O. Isabella, *Prog. Photovoltaics Res. Appl.*, 2022, **30**, 750–762.

180 G. Dong, J. Sang, C. W. Peng, F. Liu, Y. Zhou and C. Yu, *Prog. Photovoltaics Res. Appl.*, 2022, **30**, 1136–1143.

181 Q. Q. Qiu, Y. Bai, J. J. Li, C. Guo, H. Y. Chen, H. C. Zhang, J. H. Shi, W. Z. Liu, T. Chen, J. X. Liao and J. Yu, *Energy Technol.*, 2023, **11**, 8.

182 Q. Tang, W. Duan, A. Lambertz, K. Bittkau, M. A. Yaqin, Y. Zhao, K. Zhang, Q. Yang, D. Qiu, F. Gunkel, M. Weber, U. Rau and K. Ding, *Sol. Energy Mater. Sol. Cells*, 2023, **251**, 112120.

183 T. Koida, T. Matsui and H. Sai, *Sol. RRL*, 2023, **7**, 2300381.

184 X. Zeng, X. Wen, X. Sun, W. Liao and Y. Wen, *Thin Solid Films*, 2016, **605**, 257–262.

185 C. Han, Y. Zhao, L. Mazzarella, R. Santbergen, A. Montes, P. Procel, G. Yang, X. Zhang, M. Zeman and O. Isabella, *Sol. Energy Mater. Sol. Cells*, 2021, **227**, 111082.

186 T. Tang, C. Yu, C.-W. Peng, G. Dong, C. He, X. Ran, H. Jiang, V. Allen, X. Cao and J. Zhou, *Prog. Photovoltaics Res. Appl.*, 2023, **31**, 449–460.

187 T. Koida, H. Fujiwara and M. Kondo, *Sol. Energy Mater. Sol. Cells*, 2009, **93**, 851–854.

188 Q. Zou, C. Yu, Y. Zhao, Y. Liu, G. Dong, Q. Wang, X. Ran, Y. Zhang, X. Cao, J. Zhou, X. Yang, X. Zhang, Y. Zhao and X. Zhang, *Nano Energy*, 2024, **131**, 110206.

189 S. Li, M. Pomaska, A. Lambertz, W. Duan, K. Bittkau, D. Qiu, Z. Yao, M. Luysberg, P. Steuter, M. Köhler, K. Qiu, R. Hong, H. Shen, F. Finger, T. Kirchartz, U. Rau and K. Ding, *Joule*, 2021, **5**, 1535–1547.

190 J. He, G. Wang, Y. Qiu, Z. Tang, F. Ye, C. Zhang, S. Wang, L. Cai, T. Yu and P. Gao, *Adv. Funct. Mater.*, 2022, **32**, 2205901.

191 H. Sai and T. Matsui, *Sol. RRL*, 2023, **7**, 2300290.

192 T. Wenzel, A. Lorenz, E. Lohmüller, S. Auerbach, K. Masuri, Y. C. Lau, S. Tepner and F. Clement, *Sol. Energy Mater. Sol. Cells*, 2022, **244**, 111804.

193 P. Papet, L. Andreetta, D. Lachenal, G. Wahli, J. Meixenberger, B. Legradic, W. Frammelsberger, D. Bätzner, B. Strahm, Y. Yao and T. Söderström, *Energy Procedia*, 2015, **67**, 203–209.

194 J. Lossen, M. Matusovsky, A. Noy, C. Maier and M. Bähr, *Energy Procedia*, 2015, **67**, 156–162.
195 J. Schube, T. Fellmeth, M. Jahn, R. Keding and S. W. Glunz, *Phys. Status Solidi RRL*, 2019, **13**, 1900186.
196 S. H. Lee, D. W. Lee, K.-j. Lim, W.-s. Shin and J. Kim, *Electron. Mater. Lett.*, 2019, **15**, 314–322.
197 G. Limodio, Y. De Groot, G. Van Kuler, L. Mazzarella, Y. Zhao, P. Procel, G. Yang, O. Isabella and M. Zeman, *IEEE J. Photovoltaics*, 2020, **10**, 372–382.
198 Y. Zeng, C.-W. Peng, W. Hong, S. Wang, C. Yu, S. Zou and X. Su, *Trans. Tianjin Univ.*, 2022, **28**, 358–373.
199 J. Yu, Y. Bai, J. Li, Q. Qiu, T. Chen, Y. Huang, J. Yu and J. Liao, *Sol. Energy Mater. Sol. Cells*, 2023, **250**, 112057.
200 P.-C. Hsiao, N. Song, X. Wang, X. Shen, B. Phua, J. Colwell, U. Romer, B. Johnston, S. Lim, Y. Shengzhao, P. Verlinden and A. Lennon, *IEEE J. Photovoltaics*, 2018, **8**, 952–959.
201 J. Geissbuhler, S. D. Wolf, A. Faes, N. Badel, Q. Jeangros, A. Tomasi, L. Barraud, A. Descoeudres, M. Despeisse and C. Ballif, *IEEE J. Photovoltaics*, 2014, **4**, 1055–1062.
202 T. Hatt, S. Kluska, M. Yamin, J. Bartsch and M. Glatthaar, *Sol. RRL*, 2019, **3**, 2300335.
203 A. Rodofili, W. Wolke, L. Kroely, M. Bivour, G. Cimiotti, J. Bartsch, M. Glatthaar and J. Nekarda, *Sol. RRL*, 2017, **1**, 1700085.
204 A. Dabirian, A. Lachowicz, J. W. Schüttauf, B. Paviet-Salomon, M. Morales-Masis, A. Hessler-Wyser, M. Despeisse and C. Ballif, *Sol. Energy Mater. Sol. Cells*, 2017, **159**, 243–250.
205 P. Kuang, J. M. Park, W. Leung, R. C. Mahadevapuram, K. S. Nalwa, T. G. Kim, S. Chaudhary, K. M. Ho and K. Constant, *Adv. Mater.*, 2011, **23**, 2469–2473.
206 J. Bullock, D. Yan, Y. Wan, A. Cuevas, B. Demaurex, A. Hessler-Wyser and S. De Wolf, *J. Appl. Phys.*, 2014, **115**, 0021–8979.
207 W.-K. Oh, S. Q. Hussain, Y.-J. Lee, Y. Lee, S. Ahn and J. Yi, *Mater. Res. Bull.*, 2012, **47**, 3032–3035.
208 Y. S. Park, E. Kim, B. Hong and J. Lee, *Mater. Res. Bull.*, 2013, **48**, 5115–5120.
209 A. Descoeudres, C. Allebe, N. Badel, L. Barraud, J. Champliaud, G. Christmann, F. Debrot, A. Faes, J. Geissbuhler, J. Horzel, A. Lachowicz, J. Levrat, S. M. de Nicolas, S. Nicolay, B. Paviet-Salomon, L. L. Senaud, C. Ballif and M. Despeisse, *Sol. Energy*, 2018, **175**, 54–59.
210 J. Schube, T. Fellmeth, M. Jahn, R. Keding, S. W. Glunz and Konstanz, *AIP Conf. Proc.*, 2019, **2156**, 020007.
211 A. Adrian, D. Rudolph, N. Willenbacher and J. Lossen, *IEEE J. Photovoltaics*, 2020, **10**, 1290–1298.
212 M. Bivour, H. Steinkemper, J. Jeurink, S. Schröer and M. Hermle, *Energy Procedia*, 2014, **55**, 229–234.
213 M. Q. Khokhar, S. Q. Hussain, S. Kim, S. Lee, D. P. Pham, Y. Kim, E.-C. Cho and J. Yi, *Trans. Electr. Electron. Mater.*, 2020, **21**, 138–143.
214 H. Park, Y.-J. Lee, J. Park, Y. Kim, J. Yi, Y. Lee, S. Kim, C.-K. Park and K.-J. Lim, *Trans. Electr. Electron. Mater.*, 2018, **19**, 165–172.
215 D. Diouf, J. P. Kleider, T. Desrues and P. J. Ribeyron, *Mater. Sci. Eng., B*, 2009, **159–160**, 291–294.
216 L. Yang, S. Zhong, W. Zhang, X. Li, Z. Li, Y. Zhuang, X. Wang, L. Zhao, X. Cao, X. Deng, Q. Wang and W. Shen, *Prog. Photovoltaics Res. Appl.*, 2018, **26**, 385–396.
217 M. Bivour, M. Rüdiger, C. Reichel, K.-U. Ritzau, M. Hermle and S. W. Glunz, *Energy Procedia*, 2011, **8**, 185–192.
218 F. Wünsch, G. Citarella, O. Abdallah and M. Kunst, *J. Non-Cryst. Solids*, 2006, **352**, 1962–1966.
219 G. Yang, A. Ingenito, O. Isabella and M. Zeman, *Sol. Energy Mater. Sol. Cells*, 2016, **158**, 84–90.
220 K. Yoshikawa, H. Kawasaki, W. Yoshida, T. Irie, K. Konishi, K. Nakano, T. Uto, D. Adachi, M. Kanematsu, H. Uzu and K. Yamamoto, *Nat. Energy*, 2017, **2**, 2058–7546.
221 A. Tomasi, B. Paviet-Salomon, D. Lachenal, S. Martin de Nicolas, A. Descoeudres, J. Geissbuhler, S. De Wolf and C. Ballif, *IEEE J. Photovoltaics*, 2014, **4**, 1046–1054.
222 R. Jeyakumar, T. K. Maiti, M. M. Khader, N. Kandasamy, A. Verma, R. Nekovei, J. Kumar, N. Balaji and J. Yi, *J. Mater. Sci.: Mater. Electron.*, 2017, **28**, 9697–9703.
223 A. Ingenito, O. Isabella and M. Zeman, *Sol. Energy Mater. Sol. Cells*, 2016, **157**, 354–365.
224 J. P. Mailoa, C. D. Bailie, E. C. Johlin, E. T. Hoke, A. J. Akey, W. H. Nguyen, M. D. McGehee and T. Buonassisi, *Appl. Phys. Lett.*, 2015, **106**.
225 E. Yablonovitch, T. Gmitter, R. M. Swanson and Y. H. Kwark, *Appl. Phys. Lett.*, 1985, **47**, 1211–1213.
226 Z. Wang, Z. Song, Y. Yan, S. Liu and D. Yang, *Adv. Sci.*, 2019, **6**, 1801704.
227 L. Duan, D. Walter, N. Chang, J. Bullock, D. Kang, S. P. Phang, K. Weber, T. White, D. Macdonald, K. Catchpole and H. Shen, *Nat. Rev. Mater.*, 2023, **8**, 261–281.
228 R. Prasanna, T. Leijtens, S. P. Dunfield, J. A. Raiford, E. J. Wolf, S. A. Swifter, J. Werner, G. E. Eperon, C. de Paula, A. F. Palmstrom, C. C. Boyd, M. F. A. M. van Hest, S. F. Bent, G. Teeter, J. J. Berry and M. D. McGehee, *Nat. Energy*, 2019, **4**, 939–947.
229 C. Yang, W. Hu, J. Liu, C. Han, Q. Gao, A. Mei, Y. Zhou, F. Guo and H. Han, *Light:Sci. Appl.*, 2024, **13**, 227.
230 S. P. Philipps, F. Dimroth and A. W. Bett, in *McEvoy's Handbook of Photovoltaics*, ed. S. A. Kalogirou, Academic Press, 3rd edn, 2018, pp. 439–472, DOI: **10.1016/B978-0-12-809921-6.00012-4**.
231 M. A. Green, E. D. Dunlop, M. Yoshita, N. Kopidakis, K. Bothe, G. Siefer, D. Hinken, M. Rauer, J. Hohl-Ebinger and X. Hao, *Prog. Photovoltaics Res. Appl.*, 2024, **32**, 425–441.
232 NERL, Best Research-Cell Efficiency Chart, **https://www.nrel.gov/pv/cell-efficiency.html/**.
233 P. Schygulla, R. Müller, O. Höhn, M. Schachtner, D. Chojniak, A. Cordaro, S. Tabernig, B. Bläsi, A. Polman, G. Siefer, D. Lackner and F. Dimroth, *Prog. Photovoltaics Res. Appl.*, 2024, 1–9, Special Issue.
234 J. Liu, Y. He, L. Ding, H. Zhang, Q. Li, L. Jia, J. Yu, T. W. Lau, M. Li, Y. Qin, X. Gu, F. Zhang, Q. Li, Y. Yang, S. Zhao, X. Wu, J. Liu, T. Liu, Y. Gao, Y. Wang, X. Dong, H. Chen, P. Li, T. Zhou, M. Yang, X. Ru, F. Peng, S. Yin, M. Qu, D. Zhao, Z. Zhao, M. Li, P. Guo, H. Yan, C. Xiao, P. Xiao, J. Yin, X. Zhang, Z. Li, B. He and X. Xu, *Nature*, 2024, **635**, 596–603.

235 A. Saeed, L. Wang and Q. Miao, *Sol. RRL*, 2024, **8**, 2400172.

236 S. Yu, M. Rabelo and J. Yi, *Trans. Electr. Electron. Mater.*, 2022, **23**, 327–336.

237 A. Kumar, D. Kumar, N. Jain, M. Kumar, G. Ghodake, S. Kumar, R. K. Sharma, J. Holovsky, V. S. Saji and S. K. Sharma, *Sol. Energy*, 2023, **266**, 112185.

238 H. Li and W. Zhang, *Chem. Rev.*, 2020, **120**, 9835–9950.

239 A. Shah, J. Meier, A. Buechel, U. Kroll, J. Steinhauser, F. Meillaud, H. Schade and D. Dominé, *Thin Solid Films*, 2006, **502**, 292–299.

240 A. Richter, J. Benick, F. Feldmann, A. Fell, M. Hermle and S. W. Glunz, *Sol. Energy Mater. Sol. Cells*, 2017, **173**, 96–105.

241 B. Vicari Stefani, M. Wright, A. Soeriyadi, D. Chen, M. Kim, B. Wright, D. Andronikov, I. Nyapshaev, S. Abolmasov, G. Wilson and B. Hallam, *Sol. RRL*, 2022, **6**, 2200449.

242 J. Yu, J. Li, Y. Zhao, A. Lambertz, T. Chen, W. Duan, W. Liu, X. Yang, Y. Huang and K. Ding, *Sol. Energy Mater. Sol. Cells*, 2021, **224**, 110993.

243 M. Taguchi, *ECS J. Solid State Sci. Technol.*, 2021, **10**, 025002.

244 K. R. McIntosh, R. M. Swanson and J. E. Cotter, *Prog. Photovoltaics Res. Appl.*, 2006, **14**, 167–177.

245 A. Mavrokefalos, S. E. Han, S. Yerci, M. S. Branham and G. Chen, *Nano Lett.*, 2012, **12**, 2792–2796.

246 VDMA, *International Technology Roadmap for Photovoltaic (ITRPV)*, 14th edn, 2023, **https://www.vdma.org**.

247 E. H. Yousuf, M. Khokhar, S. Chowdhury, D. P. Pham, Y. Kim, M. Ju, Y. Cho, E. Cho and J. Yi, *Current Photovoltaic Research*, 2021, vol. 9, pp. 75–83.